Speciation of Aluminum During the Formation of Aluminum Chlorohydrate: A Combined Kinetic and Mass Spectrometry Study

by

MOHAMMAD FAKRUL ISLAM

Presented to the Faculty of the Graduate School of
The University of Texas at Arlington in Partial Fulfillment
of the Requirements
for the Degree of

DOCTOR OF PHILOSOPHY

THE UNIVERSITY OF TEXAS AT ARLINGTON
August 2019

Acknowledgement

I would like to express my gratitude to my advisor, professor Frederick M. MacDonnell for his effective guidance, patience, and support during my Ph.D. study. I consider myself fortunate to have the opportunity to pursue my Ph. D. under his supervision and without his continuous encouragement and guidance, it would not have been possible. I would also like to address my gratitude to Dr. Brian H. Dennis for his precious advice and guidance in the engineering field, and Dr. Rasika Dias, Dr. Robin Macaluso, and Dr. Junha Jeon for serving on my graduate committee. I would like to thank all faculty and staff members in the Department of Chemistry and Biochemistry at the University of Texas at Arlington.

I would like to thank all my colleagues from CREST lab for their friendship, assistance, and support. Dr. Chanmanee Wilaiwan, an excellent researcher and a better friend and helped me through numerous situations during my graduate study. I would like to sincerely thank my CREST lab colleague, Dr. Pawrat Bootpakdeetam for her assistance and support in the engineering work. My gratitude to Mr. Maciej Kukula at SCCAC for his assistance in LC-MS study and to support me with his kind words.

My parents Ali Ashraf and Hasne Ara Begum, who has always been there for me and supported my choice. My brother and sisters, who mean the world to me and without them I could not have made this fur in my life.

July 29, 2019

Abstract

Speciation of Aluminum During the Formation of Aluminum Chlorohydrate: A Combined Kinetic and Mass Spectrometry Study

Mohammad Fakrul Islam, Ph.D.

The University of Texas at Arlington, 2019

Supervising Professor: Frederick M. MacDonnell

Aluminum chlorohydrate (ACH) is synthesized in a heterogeneous reaction of aluminum ingots or pellets with aqueous hydrochloric acid. This exothermic reaction produces copious amounts of hydrogen gas and ultimately generates product grade aluminum chlorohydrate when the specific gravity of the solution reaches 1.33-1.35. Other product specifications include 3.5-4.0 pH, 7.9-8.4 wt.% chloride, 23-24 wt.% Al_2O_3, low turbidity (<50 NTU) and high basicity (>83%). A relative study of aluminum ingot with pellet shows that the reaction rate highly depends upon the size of the aluminum in terms of the surface area, as expected. The smaller the size of the aluminum solid, the higher the surface area to mass ratio, and the faster the rate of the ACH product formation. In a kinetic study of this reaction under commercial production conditions, we recorded the $[Al^{3+}]$ in the ACH solution versus time, using an ICP-OES to measure $[Al^{3+}]$, and observed that aluminum pellet (3.2 mm, 9.5 cm^2/g surface area) reacts 6.5 times faster than the aluminum ingot (surface area 0.3 cm^2/g, 2.27 kg bar) to produce specification grade ACH. The

reaction is always run with an 150% excess of aluminum and calculations show that 60% of the aluminum added is now dissolved.

In subsequent studies, we explored the role of trace metallic impurities, such as Fe, Co, Ni, and Cu in the kinetics of the ACH synthesis reaction. Experienced producers of ACH had long noted that if the aluminum was too pure the reaction would not 'kick-off', meaning take off and generate heat such that the reaction accelerated itself. Presumably the impurities in the aluminum play some role in the reaction kinetics. In a side-by-side study of ACH production in which aluminum with two different purities (99.99% and 99.82%) were used, we observed a substantial increase in the reaction rate (11.5 times) for those made with less pure Al. Additional studies show that a similar acceleration of the reaction can be accomplished by the deliberate addition of small quantities of these metal salts, including $FeSO_4 \cdot 7H_2O$ and $NiSO_4 \cdot 6H_2O$, suggesting that the mechanism of catalysis is via lowering the reaction barrier to hydrogen formation, i.e. these metals serve as better hydrogen evolution sites (catalysts) than Al. We observe that Ni >> Fe, Co > Cu for accelerating the ACH reaction, which matches well with their overpotential for H_2 evolution in acidic media.[1]

Table of Contents

List of Figures

List of Tables

List of Acronym

ACH	Aluminum Chlorohydrate
NMR	Nuclear Magnetic Resolution
ESI-MS	Electrospray Ionization
HPLC	High Performance Liquid Chromatography
FDA	Federal Drug Administration
PACl	Polyaluminum Chloride
SG	Specific Gravity
NTU	Nephelometric Turbidity Unit
EDX	Energy Dispersive X-ray Spectroscopy
SEM	Scanning Electron Microscopy
ESI-IT-TOF-MS	Electrospray Ionization- Ion Trap- Time of Flight- Mass Spectrometry
SEC	Size Exclusion Chromatography
CE	Capillary Electrophoresis
EDTA	Ethylenediaminetetraacetic Acid

TEM	Transmission Electron Microscopy
PID	Proportional Integral Derivative
DCM	Dichloromethane

Chapter 1

Introduction

1.1 Chemistry of aluminum chlorohydrate (ACH)

Aluminum chlorohydrate is a highly water-soluble aluminum complex with the general formula $Al_nCl_{(3n-m)}(OH)_m$ and which meets certain specifications in specific gravity, pH, basicity, turbidity, and Al content, as shown in Table 1-1.[2,3] Aluminum chlorohydrate, which is a polymerized solution of polyaluminum hydroxychloride, contains 12% aluminum by mass and is the most concentrated homogeneous aluminum solution commercially available. Removal of some of the water from ACH results in a solid in which the aluminum content varies between 46-50%.[2,4] The basicity of ACH, the degree of the aluminum polymerization and acid neutralization, is a measure of its neutralizing capacity and is reported as the ratio of OH^- per aluminum charge. If 5 of the 6 positive charges on the aluminum are offset by hydroxides, the basicity would be 83%, which is the specification value for ACH. A basicity of 83% is also the highest basicity available in a stable solution form for any polyaluminum solution.[4] Because of the high basicity, ACH is more efficient in coagulating the negatively charged contaminants in a water treatment process than other aluminum salts including alum, aluminum chloride, and related polyaluminum compounds, and leaves fewer negatively charged counterions in the resulting clarified solution.[2,3,4]

Table 1-1. Industrial specifications for aluminum chlorohydrate solution (ACH)

Alumina, % Al_2O_3	23.0-24.0
Chlorides, % Cl	7.9-8.3
Basicity, %	>83
Specific Gravity (at 60^{o}F)	1.33-1.35
Turbidity	<50 NTU
pH	3.4-4.0

In addition to the water treatment application described above, ACH in both solution and powdered form is also the active ingredient of many antiperspirants. Upon contact with the skin, ACH forms a variety of polymer species, some of which play a critical role in ACH's activity as antiperspirant .[5,6]

In terms of its structure, the hydrolysis products of ACH are highly pH dependent; below pH 4, it forms a trivalent aluminum cation surrounded with six water molecules to form an octahedral structure (figure 1-1).[7,8] At higher pH, more complex aluminum hydroxy species form, which eventually leads to the formation of $Al(OH)_3$ (s). Above pH 8.0, most of the water soluable aluminum forms a tetrahedral tetrahydroxyaluminate ion, $[Al(OH)_4]^-$.

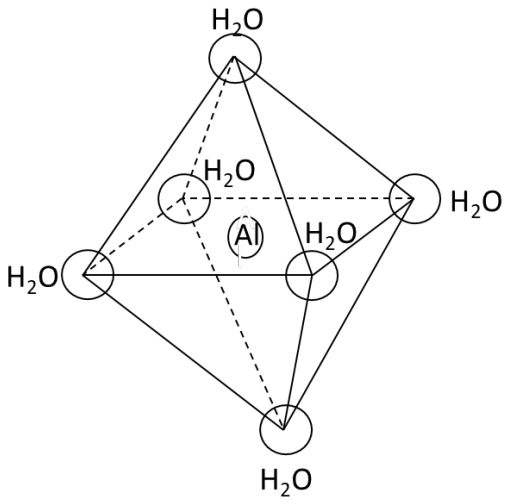

Figure 1-1: Structure of octahedral monomer species of aluminum chlorohydrate hydrolysis.[8,9]

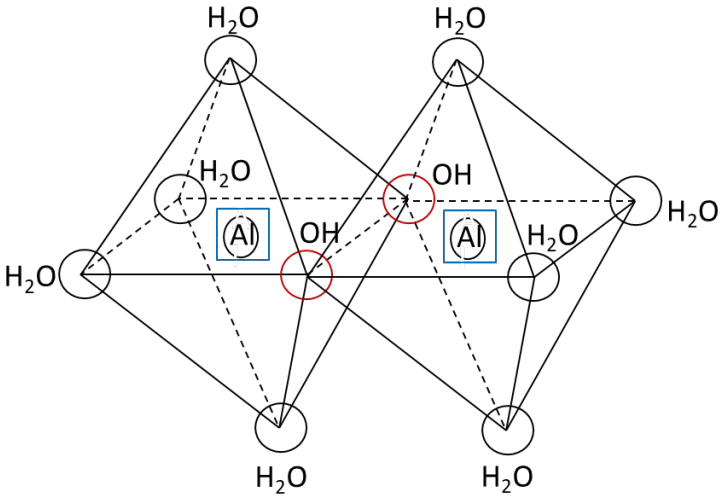

Figure 1-2: Structure of dimer-species of aluminum chlorohydrate hydrolysis.[10,11]

Experimental data shows that there are a wide variety of aluminum polymeric species present in a bulk sample of aluminum chlorohydrate, usually ranging from polynuclear species between Al_2 – Al_{200}.[7,10] The presence of these polymeric species can be found through several analytical

methods, including X-ray, ^{27}Al NMR, Raman, IR, size exclusion chromatography, capillary electrophoresis, potentiometry, ESI-MS, and HPLC.[12-15] However, few polymeric species, such as the monomer, dimer (figure 1-2), Al_{13} (figure 1.3) and Al_{30} aggregates, appear to be dominant species.[2,15] In addition, to make $Al_{13,}$ two smaller Al species may condense in a stepwise polymerization reaction as seen in Rxn 1 – 3 below.[2,7] Subsequent polymerization of the dimers and monomers gives higher nuclearity species. The dimer goes through further polymerization and forms various species such as $Al_3(OH)_4(H_2O)_9^{5+}$, $Al_6(OH)_{12}(H_2O)_{12}^{6+}$, $Al_{13}O_4(OH)_{24}(H_2O)_{12}^{7+}$, and Al_{14}-Al_{200} species.[2]

$$3Al_2(OH)_5Cl\cdot 2H_2O \longrightarrow Al(H_2O)_6^{3+} + 3Cl^- + 5Al(OH)_3 \quad \text{(Rxn 1)}$$

$$Al(H_2O)_6^{3+} \longrightarrow Al(OH)(H_2O)_5^{2+} + H^+ \quad \text{(Rxn 2)}$$

$$2Al(OH)(H_2O)_5^{2+} \longrightarrow Al_2(OH)_2(H_2O)_8^{4+} + 2H_2O \quad \text{(Rxn 3)}$$

The Al_{13} cluster is thought to be of particular importance and is believed to have the α-Keggin structure shown in Figure 1-3. In this structure, the cluster has a central tetrahedral aluminum ion surrounded by twelve Al octahedrons, reformulated as $(AlO_4Al_{12}(OH)_{24}(H_2O)_{12})^{7+}$. Experimental data to support the α-Keggin structure includes ^{27}Al NMR and GFC studies, with NMR spectra confirming the presence of octahedral and tetrahedral Al^{3+} sites. The special stability of this structure comes from the bridging of three of the oxygens on each of the octahedra with three neighboring octahedrons. As a result, a generally spherical and closed structure is formed with better stability than smaller and most larger clusters.

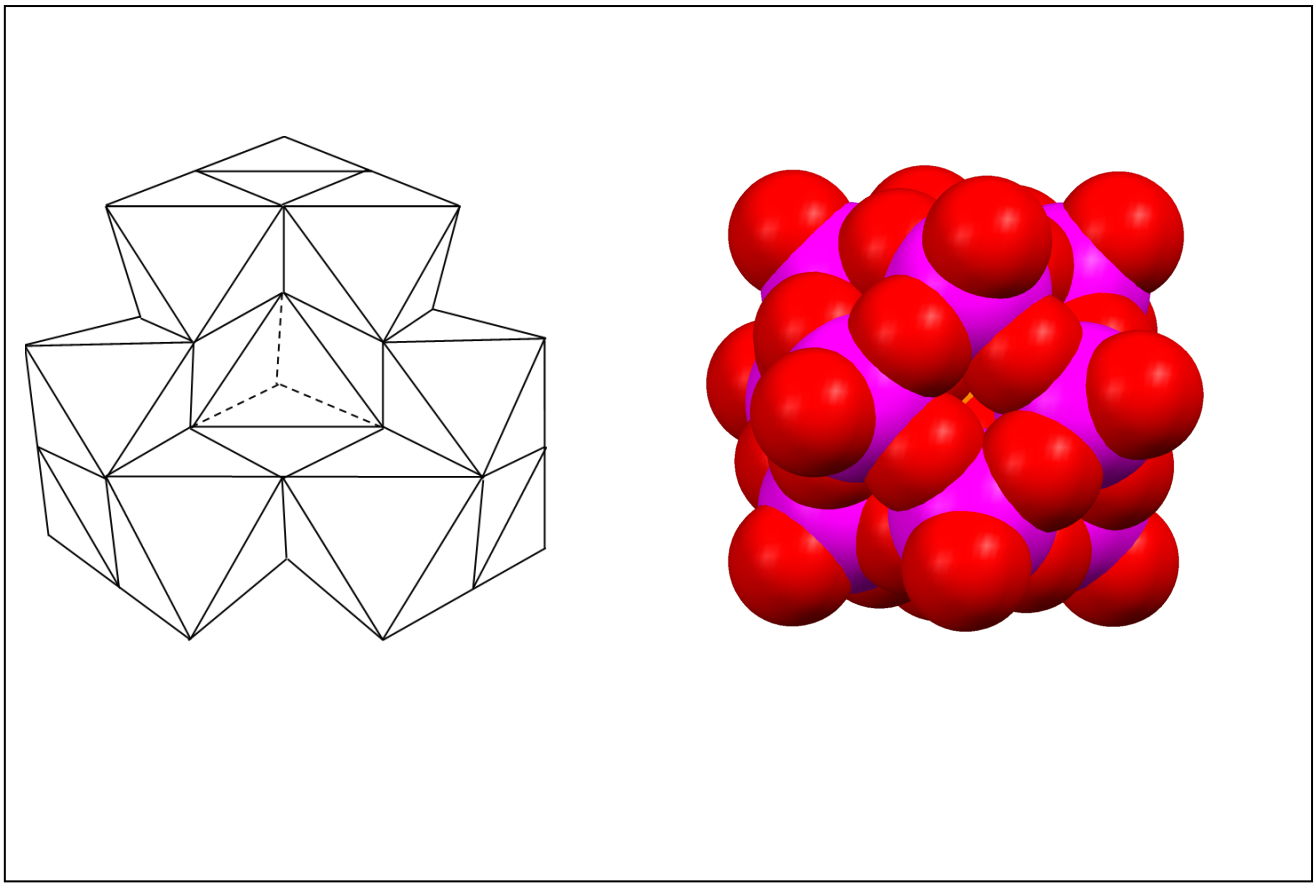

Figure 1-3: A polyhedral representation (left) and right space-filling model (right, hydrogens not shown) of the α-Keggin structure proposed for the dominant Al_{13} species in ACH.[7,16]

ACH chemistry has been investigated both experimentally and theoretically for quite some time, and it is clear that the ACH solution comprises a complex mixture of oligomeric species, some of which are dominant.[16] This complexity and lability of Al^{3+} has also made isolation of individual species near impossible. Computational chemistry has been useful in that modelling can help identify certain stable structures over others.

ACH has a wide variety of applications including drinking water treatment, sewage and industrial waste water treatment, and paper and cosmetics manufacturing.[17,18] The evolution of the uses of ACH and the functioning mechanism in antiperspiration and water treatment processes are briefly discussed in the following section (1.1-1.2).

1.2 Antiperspiration

Underarm perspiration, generated from the sweat glands, is essential for bodies in various ways including the regulation of body temperature, moistening and protecting the skin from dryness, and removing the lactic acid; however, it does come with possible offensive smell.[19,20] People have worried about offensive body odors since the ancient Egyptians, or even earlier.[21] The Egyptians invented the perfumed bath, and they were known to apply perfume to their underarms. The Greeks and Romans regularly bathed in perfume and soaked their clothes in perfumed water so they could smell good. As there was a limited understanding about the source of the body odor, most of the activities were focused on masking the body odor using perfumes, scented candles, and essential oil.[21]

In 1888, Mum deodorant became the first commercially available deodorant consisting of a zinc oxide cream and was applied to the underarm.[21] Although it took care of the odor, it was not very effective against excessive perspiration. The first antiperspirant 'EverDry' became available in 1903 and used aluminum chloride as the primary active ingredient.[21] Since this time, numerous commercial antiperspirants have been developed and almost all use different kinds of aluminum or zirconium salts as the active antiperspirants. However, the early antiperspirants were often quite acidic and prone to cause skin irritation and damage to clothing.[21]

Around 1947, ACH was first synthesized and its mild pH helped overcome these problems.[21] It has a pH range of 3.5-4.0, which is similar to the skin acid mantle and therefore does not irritate the skin. It is notably less acidic than aluminum chloride and so does not damage clothing. ACH also shows improved antiperspirant performance with no or limited adverse side-effects. In addition to ACH, sodium zirconium lactate was also found effective as an antiperspirant, although it was discontinued in the 1970's by rule of the FDA.[21] Currently the

most widely used antiperspirant ingredient is either aluminum chlorohydrate based or aluminum zirconium chlorohydrex-glycine.[21]

ACH has two important functions as an antiperspirant.[20,22] The first is to reduce the amount of secretion from the glands, and the second is to control the bacterial growth there. ACH can form a blockage (plug) deep within sweat ducts by altering the sweat duct permeability to fluids, consequently forming a superficially obstructing plug to inhibit the excretion of sweat from the sweat glands.[5,6,21,22]

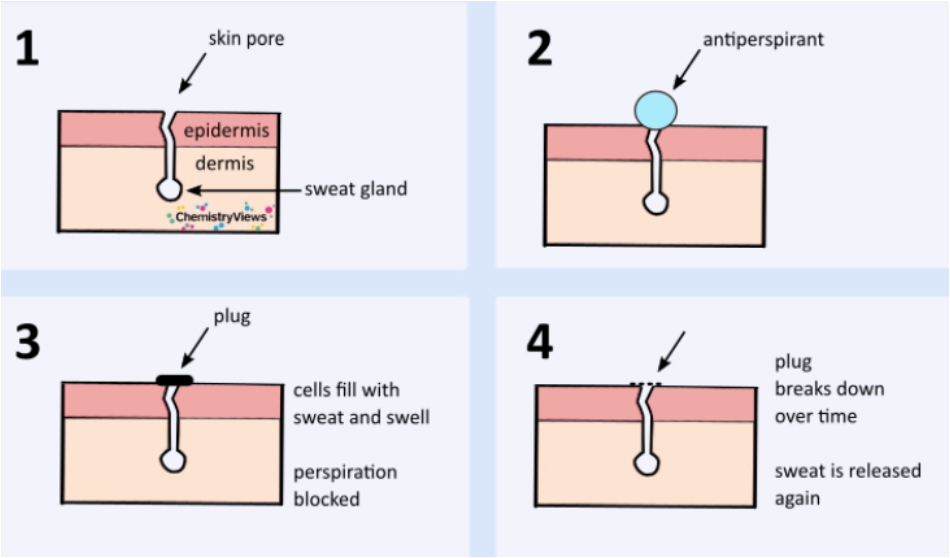

Figure 1-4: Antiperspiration mechanism of aluminum chlorohydrate on human body.[21]

1.3 Water treatment

Aluminum chlorohydrate also functions as an active coagulant for water treatment.[17,18] The two most predominantly used inorganic coagulants are aluminum-based and iron-based coagulants. Aluminum-based coagulants are mainly alum (aluminum sulfate), aluminum chlorohydrate (ACH), sodium aluminate, and polyaluminum chloride (PACl), whereas iron-based coagulants are mainly iron chloride and iron sulfate.[23,24,25,26]

Chemical coagulation involves destabilizing the charged colloidal particles and the clustering of the fine particles into larger structures (flocs) that can be precipitated out of the solution. The method of coagulation generally falls into two categories: charge neutralization and swept coagulation.[17,27] In charge neutralization, the strong negative surface charges of the water's impure particles cause repulsion to each other, but these negative charges can be neutralized by the addition of aluminum salts into the water. The neutralized impurity particles then start to form flocs and precipitate. The whole process is swift, taking about 0.01-1 sec, and works better in an acidic range because at a lower pH the contaminants have a lower negative charge.[27]

In the other method, swept coagulation, the contaminant particles get adsorbed onto the surface of the aluminum ion, and then either get trapped inside the aluminum hydroxide floc or swept down by the sinking floc. When the aluminum hydroxide floc size and mass is large enough, it starts to precipitate.[27] In water treatment, swept coagulation is the more commonly used process because of the difficulties in achieving the rapid mixing required in charge neutralization. The process of swept coagulation is shown in the figure 1-5.

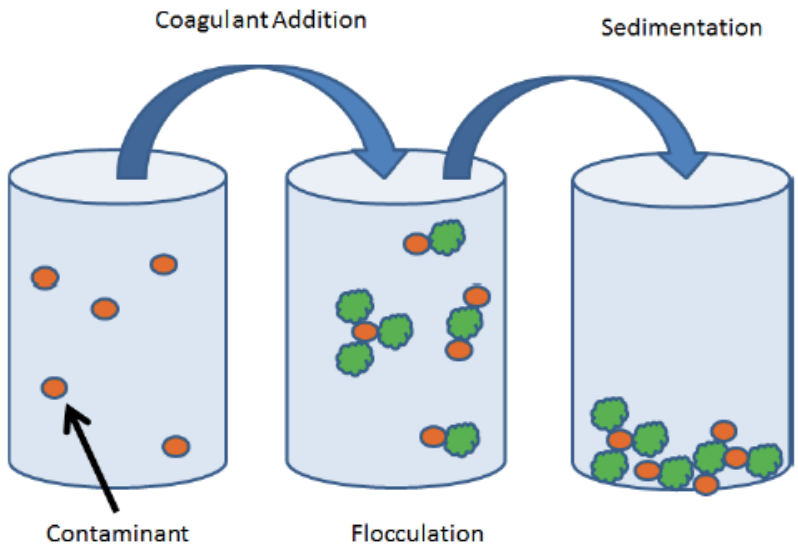

Figure 1-5: Schematic diagram of the process of coagulation in water.[28]

The most critical parameters of a coagulant include pH, concentration, mixing speed, temperature, and retention time. The higher the valence of the counter ion, the more the impurity particles are destabilized, meaning a relatively smaller quantity is needed for coagulation. ACH is a pre-hydrolyzed coagulant that produces a wide range of hydrolysis species regardless of the process conditions during the treatment, and because they form multicharged polynuclear complexes with increased adsorption ability, they are very useful and becoming more popular compared to other coagulants.[28] The following figures shows the effectiveness of ACH (figure 1-7) and a relative comparison of the activity of ACH, alum, and polyaluminum chloride in water treatment (figure 1-6 and 1-8).[29]

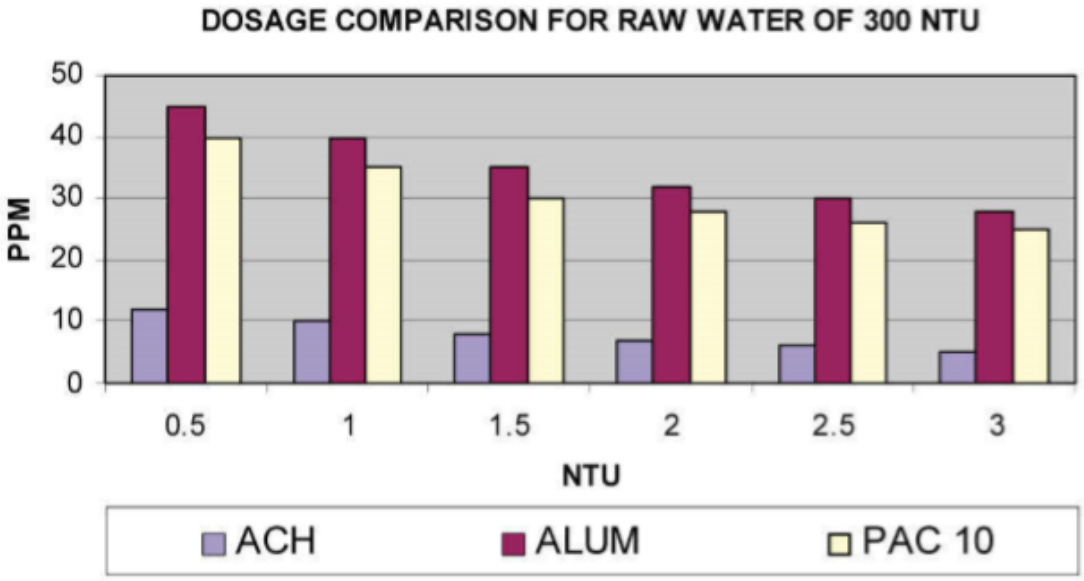

Figure 1-6: Comparison of different coagulants for water treatment. (ACH= aluminum chlorohydrate, alum= aluminum sulfate, PAC10= polyaluminum chloride).[29]

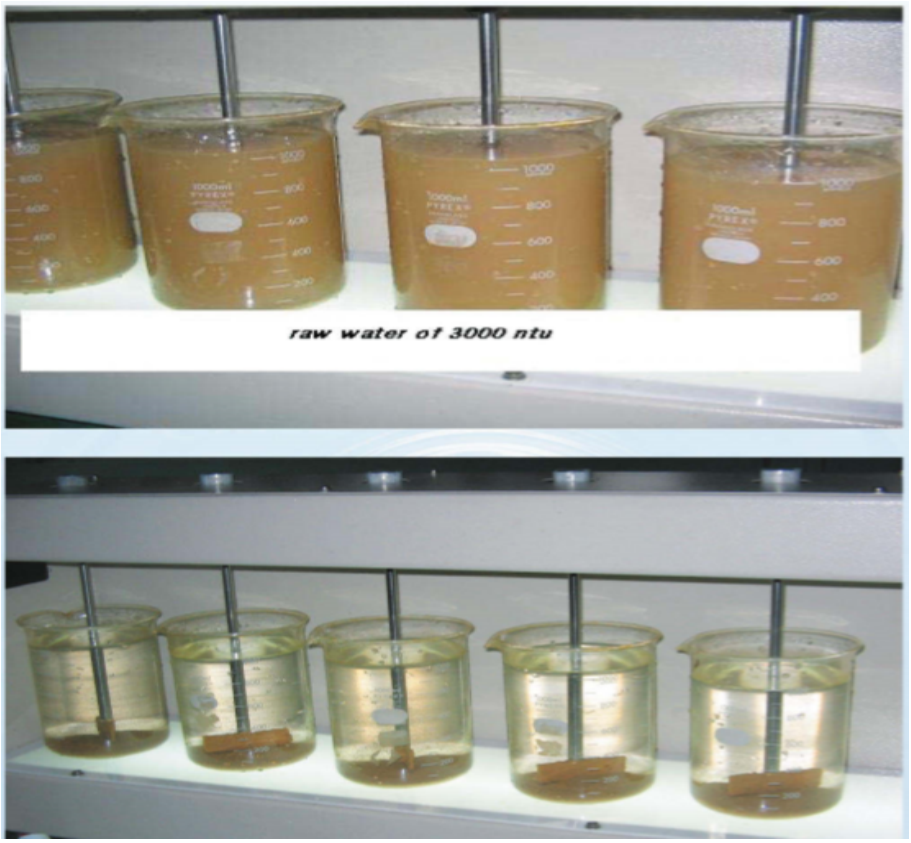

Figure 1-7: Effectiveness of aluminum chlorohydrate as a coagulant for water treatment.[29]

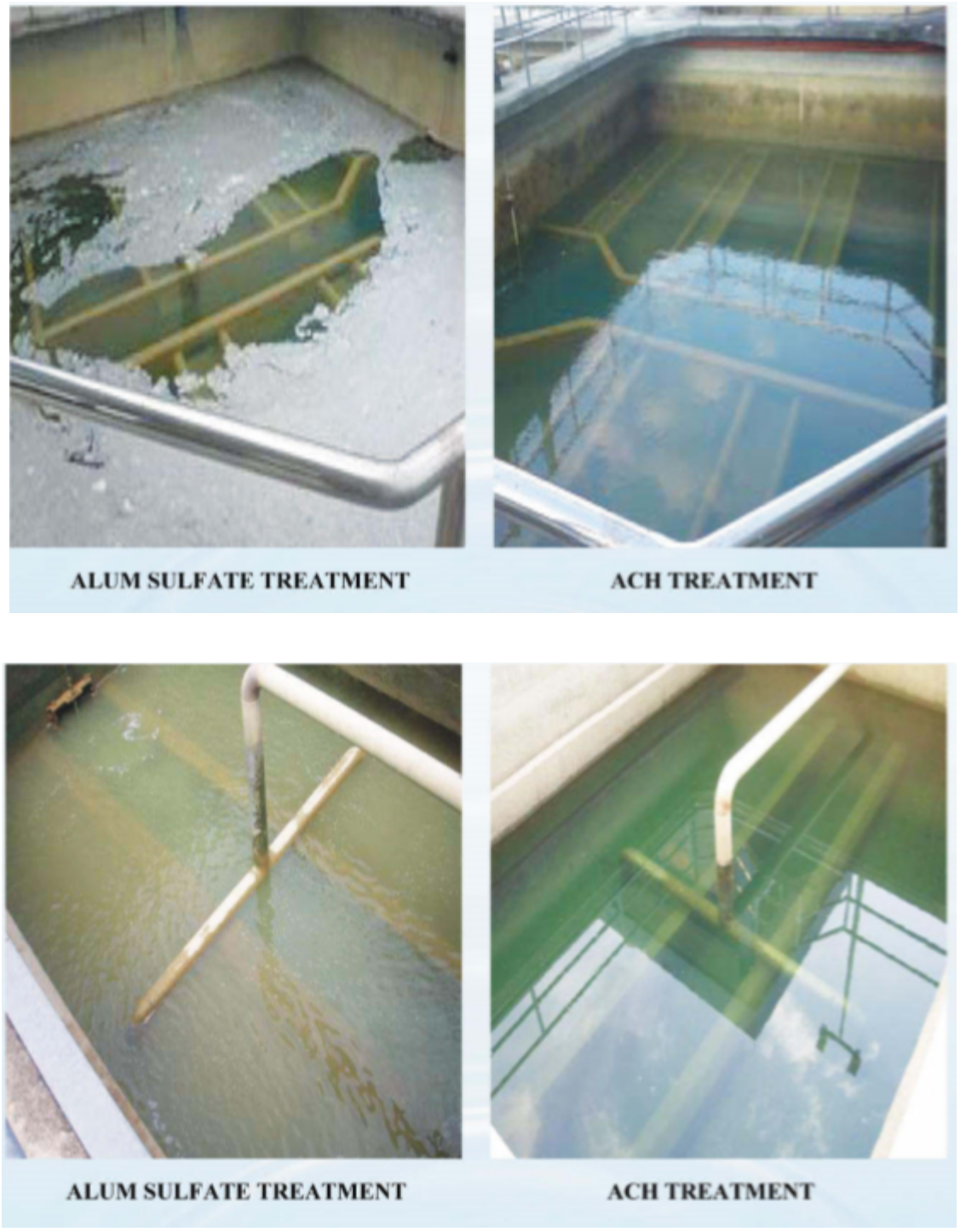

Figure 1-8: Comparison between the efficiency of alum and aluminum chlorohydrate in water treatment.[29]

ACH contains 23% Al_2O_3 and has a basicity >83%, whereas alum has 8.3% Al_2O_3 and no basicity. PACl has about 10% Al_2O_3 and 50% basicity. Because of its high basicity and

concentrated aluminum, effective water treatment usually requires two to three times the amount of PACl and alum as ACH. In fact, ACH coagulant has many advantages, including:

- Requires lower amount to achieve water treatment goals (2 to 3 times lower than PAC and alum)
- Functions at a wide range of pH
- Less sensitive to water temperature
- Reduces chemical sludge and residue production
- Lowers turbidity in treated water
- Forms larger and heavier flocs more quickly than other coagulants

1.4 Scope of the study

Despite extensive studies on the structure of aluminum chlorohydrate,[7,10,12] neither the structure nor the geometrical parameters of ACH are well understood. This is due to the complex composition of ACH, which forms numerous different polymeric species upon hydrolysis. In addition, ACH hydrolysis forms about 200 different aluminum clusters.[21] Even though there are numerous studies about the structure of the ACH, no systematic study has been done on the synthesis of the ACH.[13] Therefore, to better understand the structure and activity of ACH and its many oligomer/polymers, a better understanding of the methods and parameters of ACH synthesis is necessary.

The most widely used ACH preparation method is the redox reaction of metallic aluminum with hydrochloric acid at 80-100°C (Rxn 1),[30] which forms $[Al(H_2O)_6]^{3+}$. Over time, as the acid is consumed and the pH begins to rise, the $[Al(H_2O)_6]^{3+}$ undergoes numerous hydrolysis reactions to form hydroxo and oxo-bridged polymers of aluminum(III), shown partially in reactions 2a and

2b. ACH is ultimately a highly concentrated solution of Al(III) in which the soluble polymeric forms of the Al(III) are metastable and remain in the solution for long periods.

$$2\ Al\ (s) + 6H^+\ (aq) + 12\ H_2O\ (l) \rightarrow 2\ [Al(H_2O)_6]^{3+} + 3\ H_2\ (g) \quad \text{(Eqn. 1)}$$

$$2\ [Al(H_2O)_6]^{3+} \rightarrow 2\ [(H_2O)_5Al\text{-}OH\text{-}Al(H_2O)_5]^{5+} + H_3O^+ \quad \text{(Eqn. 2a)}$$

$$2\ [Al(H_2O)_6]^{3+} \rightarrow 2\ [(H_2O)_5Al\text{-}O\text{-}Al(H_2O)_5]^{4+} + 2H_3O^+ \quad \text{(Eqn. 2b)}$$

Industrially, aluminum ingots (20 kg each) are the preferred aluminum source. Because these ingots have relatively low surface area, the ACH reaction usually takes 4-7 days (up to 10 days) and the addition of external heat. However, this is a long time to wait for the reaction to occur and can be improved upon.

Therefore, the purpose of this study is to develop a faster and more efficient way to synthesize ACH, and considers the surface area of the metal, acid strength, and temperature of the system as the key factors. Even though this study is conducted in a laboratory, the data is scaled up to what would be industrial size for comparison purposes. Finally, the problems that can arise when synthesizing at an industrial scale, such as an increased turbidity of the solution, are discussed and accounted for, which increases the real-world applicability of the results.

Scope of the study:

- Explore a faster and more efficient way to prepare aluminum chlorohydrate

  Key factors:

  i. Surface area of Al
  ii. HCl concentration
  iii. Temperature of the reaction

- Study the kinetics of the ACH synthesis reaction
- Investigate the effect of metal impurities on aluminum chlorohydrate formation
- Propose a possible mechanism for the formation of aluminum chlorohydrate formation

Chapter 2

Synthesis of Aluminum Chlorohydrate (ACH)

2.1 Introduction

There are several methods in practice to prepare aluminum chlorohydrate. It can be prepared as a solution or a powder, and the composition of the final product (iron impurity levels, specific gravity, and pH) might vary, depending on the application.

One of the primary methods to prepare ACH comprises the oxidation of metallic aluminum with either hydrochloric acid or aqueous aluminum chloride at moderate (~80-90 °C) or boiling conditions.[30,31] The typical reaction is as follows:

$$3HCl + 6Al + 15H_2O \longrightarrow 3\,Al_2(OH)_5Cl\cdot 2H_2O + 9H_2$$

$$AlCl_3 + 5Al + 15H_2O \longrightarrow Al_2(OH)_5Cl\cdot 2H_2O + 15H_2$$

This is a redox reaction that can be written as follows:

Oxidation half reaction: $Al \longrightarrow Al^{3+} + 3e^-$

Reduction half reaction: $2H^+ + 2e^- \longrightarrow H_2$

Overall reaction: $2\,Al(s) + 6\,H^+(aq) \rightarrow 2\,Al^{3+}(aq) + 3\,H_2(g)$

This reaction readily produces a large amount of hydrogen gas. Aluminum ingots or powder are generally used as the source of aluminum. Aluminum ingots are slow to react and generally take up to 7-10 days to produce ACH. Aluminum powder has a somewhat faster reaction rate (1-4

days); however, because it has the potential to explode when exposed to air, static, or sparks, the proper handling of aluminum powder is extremely critical.

Another way to prepare ACH is reacting aluminum alkoxide $Al(OR)_3$ with hydrochloric acid in an aqueous phase (US. Patent no. 3, 887, 691).[32] The product of this reaction readily separates into two phases, one of which includes alcohol co-products. The reaction occurs at room temperature at a considerable rate, possibly faster at higher temperatures. However, the alcohol co-products produced in this method tend to become trapped in the product and may change the properties of the ACH solution (US. Patent no. 4, 267, 161).[33] Therefore, this method requires complete removal of all the alcohol co-products before the ACH can be recovered. Alternatively, they proposed a method to prepare ACH that reacts aluminum alkoxide with methanol to produce aluminum methoxide; the aluminum methoxide solution is washed to remove all of the higher alcohols and then reacted with hydrochloric acid at moderate to high temperatures (130-450 °F).

$$2Al(OR)_3 + HCl + 7H_2O \longrightarrow Al_2(OH)_5Cl \cdot 2H_2O + 6ROH$$

ACH can also be prepared by reacting aluminum chloride or hydrochloric acid with aluminum hydroxide.[31]

$$2Al(OH)_3 + HCl + H_2O \longrightarrow Al_2(OH)_5Cl \cdot 2H_2O$$

$$5Al(OH)_3 + AlCl_3 + 6H_2O \longrightarrow 3Al_2(OH)_5Cl \cdot 2H_2O$$

All of these previous methods of producing ACH result in copious amounts of hydrogen gas, which is an explosion hazard. Therefore, in effort to avoid this unwanted production of H_2 gas, an alternative approach to prepare ACH is the electrolysis approach, which results in minimal

levels of H_2 gas production. The electrolysis of aluminum chloride to produce ACH method is described in U.S. patent 2, 392, 531.[34] This approach uses a diaphragm cell containing an aqueous solution of aluminum chloride, and the cathode and anode are separated into different compartments. However, in this method, the yield of ACH is not satisfactory for two reasons. The first reason is the ACH might become contaminated. The other reason is that most of the produced chlorine gas leaves the system. In fact, the recovery of chlorine is a difficult process, thus a method to keep it in the system was developed (US. Patent no.3, 113, 911).[35]

J.L. Jones[35] found that the loss of chlorine could be avoided by introducing an adjacent cathode compartment where the produced chloride ion reacts with the aluminum oxide to form aluminum chloride before it reaches to the anode compartment. Thus, the aluminum chloride can be recirculated to the cathode compartment to produce ACH. The reaction includes:

I. $5H_2O \longrightarrow 2.5\ H_2 + 5OH^-$

II. $2AlCl_3 + 5OH^- \longrightarrow Al_2(OH)_5Cl + 5Cl^-$

III. $2Al_2O_3 + 6HCl \longrightarrow 2AlCl_3 + 3H_2O$

IV. $2H_2O \longrightarrow O_2 + 4H^+$

This electrolysis process, however, generates a wide range of aluminum hydroxy complexes and its use in industry is very limited.

Because all of the methods discussed in this section come with some drawbacks, this study focuses on the improvement of the redox method of preparing ACH, which is the most widely used method in industry today. In this study, all the experiments follow the procedure of using metallic aluminum and hydrochloric acid to prepare the ACH at moderate to higher temperature. However, some key parameters are changed, namely surface area and temperature. Although

ingots are mostly used in industry for this reaction, this study focused on the advantages of using small aluminum pellets (3-6 mm in diameter) in terms of increased surface area over ingot and decreased reactivity relative to Al powder. Moreover, some industrial procedures emphasized the risk of thermal runaway and avoided allowing the reaction to reach a boil. Reaction temperatures were stringently monitored to keep the reaction between 80-90 °C. We show here that this risk is not real and running the reaction under boiling conditions has no risk of thermal runaway, nor does it cause any decrease in product quality as long as the solution water level is maintained during the reaction.

2.2 Composition of Aluminum Chlorohydrate (ACH)

The reaction of aluminum with hydrochloric acid forms ACH and hydrogen gas. This reaction is exothermic, and the rate of the reaction is known to depend on the following factors: aluminum surface area, hydrochloric acid concentration, and temperature. In addition, although aluminum and hydrochloric acid react to form ACH, it takes some time to produce what is known as industrially accepted ACH or specification grade ACH. For this reason, as the reaction is occurring, the solution must be continually checked against the industrially accepted specifications of ACH to ensure its quality. This is done by examining the specific gravity and pH measurements of the solution. If SG and pH specifications are met and the turbidity is acceptable, generally all of the remaining specifications are also met.

The final product specification of ACH in this study follows the industrially accepted specifications listed below:[3]

Alumina, % Al_2O_3	23.0-24.0
Chlorides, % Cl	7.9-8.3
Basicity, %	>83
Specific Gravity (at 60°F)	1.33-1.35
Turbidity	<50 NTU
Al, %	12.0-12.7
pH	3.4-4.0

The ultimate objective of this study is to determine a general procedure for using aluminum pellets to prepare solutions of ACH in the range of 20 -25% by mass ACH and turbidity of <50 NTU, and to determine the quality of this product (pH, turbidity, specific gravity) with respect to the quality of ACH generated by using aluminum ingot. Moreover, the general kinetics of the reaction are desired, so as to gage the relative efficiency of the ingot vs pellet processes. One initial concern in this study was that the ACH turbidity may be compromised by the faster rate of reaction and temperatures found pellets compared to ingot. To this end, this study analyzes the amount of ACH and hydrogen gas produced as a function of time, how surface area and acid concentration affect the rate of the dissolution reaction, and how the amount of heat generated per unit time impacts turbidity.

2.3 Industrial Procedure of ACH Synthesis

One industrial process for preparing ACH from aluminum ingots and hydrochloric acid was described to us by an unspecified producer in general terms below.

Large aluminum ingots (~16,000 lbs.) are loaded into a large tank and covered with water, and HCl acid is added (with an estimated final strength of 5% HCl by mass) to start the dissolution process. Next, the solution is heated to just below boiling (~95 °C), and steam is used to dilute the evolved hydrogen gas to safe levels. The process takes a total of 5 days during which both additional water and acid are added to keep the reaction going and to keep the ingots cover with solution. The reaction is monitored by measuring [Al^{3+}], pH, and SG of aliquots drawn at various time points in the reaction. When the reaction is done, the solution is allowed one day to cool and then drained. This cooling day is included in the 5-day total reaction time. In this process, 62% of the aluminum ingot mass is dissolved during the reaction period, and the process yields 6,000 gallons of industrial specification quality ACH.

2.4 Experimental

2.4.1 Materials

Two different types of aluminum used in this study: *type I* Al ingot and *type II* Al pellet. Metallic Al has various levels of impurity mixed with it depending on the extraction methods. These impurities include different kinds of metal mixed with Al. The detailed composition of the Al is given in table 2-1.

Table 2-1(a): Composition of the Al pellet and ingot used in the study.

	Types of Al	Surface area (cm^2/g)	Al %
I	Ingot	0.3	99.824
II	Pellet (3.2-9.5 mm)	3.9-5.8	99.824

Table 2-1(b): The total composition of the metallic impurity mixed with the Al metal.

Types of Al	Fe (ppm)	Si (ppm)	Mg (ppm)	Ni (ppm)	Zn (ppm)
Pellet/Ingot	850	500	10	40	10

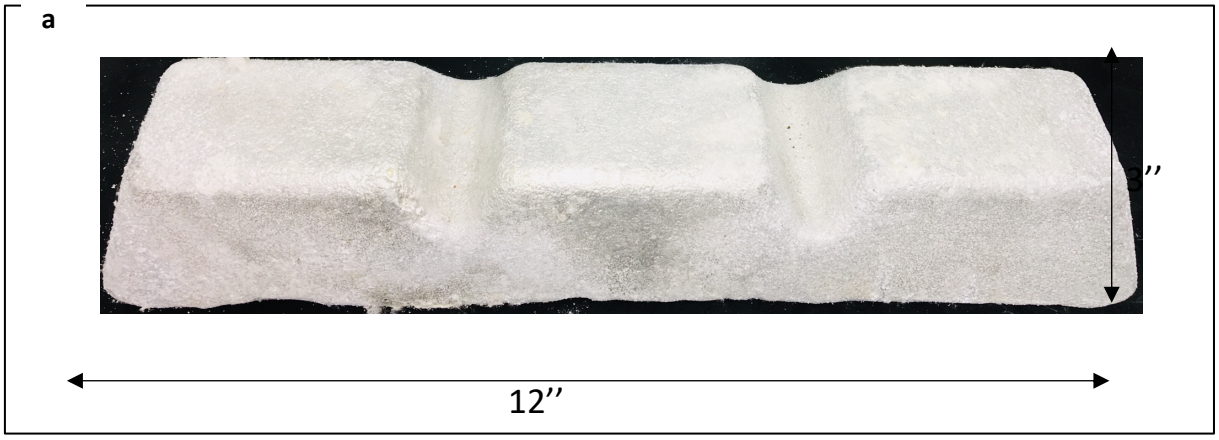

b

Figure 2-1: a) Aluminum ingot and b) pellet used to synthesize ACH.

Al pellets and ingots used in this study provided by C-KOE (C-KOE metals, L.P.). The specific gravity was measured using portable density meter (Anton Paar DMA 35). pH of the ACH solution was measured using a Symphony benchtop meter (B10P, VWR)). The [Al^{3+}] concentration in ACH solution determined using inductively coupled plasma-optical emission spectrometry (ICPE- 9000, Shimadzu) and the chloride ion concentration measured using a chloride selective electrode. Turbidity of the ACH solution determined using a portable turbidity meter (Hanna Instruments 93703).

2.4.2 Optimization of ACH Synthesis

A parametric study in which the form of the Al (pellet or ingot) and therefore surface area of the aluminum per unit mass was examined with respect to the time required to complete the process and the quality of the product. During this parametric study, we also examined other important factors, including reaction temperature, active heating, acid strength, aluminum loading (used a large molar excess of Al). The most common measurement of reaction progress was the specific gravity (SG) and pH or reaction aliquots at room temperature. For all of the experiments in this study, reaction time is defined as the time for the reaction solution to reach 1.33 specific gravity and pH in the range of 3.5-4.0.

While numerous reactions were run with different parameters, the procedure below describe the typical procedure followed. Descriptions of deviations from this are given in follow-up experimental procedures or in the results and discussion section.

2.4.2.1 Synthesis of ACH

Experiment 2.1

a. A 500 mL round bottomed flask was charged with 78.4 g Al pellet (type II pellet, 5.8 cm^2/g surface area) and 167 mL water. To this mixture was added 158 mL (2/3 of the total 237 mL) of 20% HCl (6.8 M) upon which H_2 gas was observed to bubble from the solution. As the reaction is exothermic and extremely vigorous, the HCl added periodically instead of altogether once. Over time, the rate of H_2 evolution increased as the reaction warmed up and became more vigorous. The temperature was observed to rise slowly and then quickly, reaching a maximum of 96 ^oC, which then levelled off and began to cool. Once this exothermic phase had past, another 79 mL of 20% HCl was added and the reaction flask was transferred into preheated oil bath (100 ^oC) and fitted with a reflux condenser. Once the specific gravity of the reaction solution reached 1.33, the flask removed from the oil bath and cool down to the room temperature.
b. An experiment identical to run 2.1 (a) was done except that the boiling solution, once it began to cool was moved to a sand bath at 90 °C. Once this reached a steady temperature of 87 °C, it was monitored periodically until the SG reached 1.33. Time to end of reaction 72 hours. The pH of the final product was 3.5, specific gravity 1.34 and the turbidity 22 NTU.

Experiment 2.2

The goal of this experiment is to examine the effect of the different sizes of the aluminum pellets (i.e. surface area of the aluminum) on the reaction rate of ACH formation in a small-scale reaction (220.0 g pellets). The amount of Al pellet loadings in the reaction might affect the reaction rate, and an excess over the stoichiometric amount of Al loadings may keep the reaction rate much steadier. In this experiment, compared to the HCl acid volume, Al loadings are at 150% excess over the stoichiometric amount. However, temperature and acid concentration are kept the same as discussed in the previous section (experiment 2.1 a).

Along with the type II Al pellet (3.95 cm^2/g surface area, 99.824% Al), two other sizes of Al (4.4 cm^2/g and 5.8 cm^2/g surface area, 99.824% Al) pellet are used in this study.

Experiment 2.3

The effect of the surface area of the metallic aluminum is examined in large-scale reactions (2268 g pellets/ingot) where 150% excess aluminum is used, and the reaction is kept at boiling conditions. Three different sizes of type II Al pellets (3.2 mm, 6.4 mm, and 9.5 mm) and type I Al (ingot) is used to prepare ACH. All three Al pellets and the ingot have 99.824% pure Al mixed with other trace metallic impurities (table 2-1).

In order to perform the large-scale reactions, a polypropylene tank is used instead of a round bottomed flask. The reactor is a polypropylene tank with insulation to prevent any heat loss. A heater is attached to the tank, so that when the exothermic reaction phase is passed, the desired temperature can be maintained. A thermocouple is attached to the reactor to automatically monitor and record the temperature every 5 s. The top of the reactor is connected to a reservoir through a pipe; this reservoir collects evaporated acid to prevent any damage to the fume hood

due to acid corrosion. The reservoir is then connected to an exhaust to release the generated hydrogen. The reactor has a tap at the bottom so samples can be collected at regular intervals. The reactions conditions maintained in this experiment are: 150% excess Al (pellets/ingot), 20% HCl and 100 °C boiling temperature.

Experiment 2.4

Turbidity is one of the important parameters of the ACH specifications and it requires to preferably less than 50 Nephelometric Turbidity Unit (NTU). To optimize the reactor settings to keep the turbidity low, two different reactors is designed and fabricated (experiment 2.4.1-2.4.3) and tested with an 8" deep bed of 3.2 mm diameter pellets (5.76 cm^2/g surface area). ACH solution is circulated through the reactors during the synthesis in two different manners: active and passive circulation. All tests were performed at boiling conditions and lasted approximately 24-28 hours.

Experiment 2.4.1. No Circulation

A reactor was fabricated from a 6' long Lexan tube. The reactor had a port near the top for adding acid and a port just above the pellet bed for taking liquid samples. The bottom was sealed with a large Viton stopper. The top of the reactor was connected to a large tube that carried the hydrogen gas to a nearby ventilation hood. Three thermocouples were attached to the outside wall of the reactor for monitoring the temperature along the length of the reactor. A ribbon heater and a controller using thermocouple feedback was added to keep the bed at boiling temperature. Approximately 385 g of 3.2 mm pellets, 970 mL of water, and 278 mL of 20% HCl were used for each run.

Experiment 2.4.2. Active Circulation

This is an active approach towards providing bed hydration (figure 2-2). A diaphragm pump was used to draw boiling liquid from above the bed and inject it into the bottom of the bed. A liquid volume turnover time of 10 minutes was used to determine the pump flow rate. The same recipe, pellet size, and bed depth described in the previous section were used for these experiments. An additional heater and controller were used to make sure the fluid on top of the bed, the pump intake, was boiling. All the tests with circulation there was no evidence of ACH crystallization or gelling.

Experiment 2.4.3. Passive Circulation

The passive circulation approach involves modifying the reactor by adding a stovepipe in the center (figure 2-3). This is a passive, gravity driven approach to bed hydration. A 12-inch stand pipe was placed at the center of the bed. Approximately 30 holes were drilled on the bottom quarter of the pipe to allow liquid to reach the bottom of the bed. The hydrogen rising from the bottom of the bed creates a void that draws the liquid in from the bottom of the pipe.

All the experiments including the reaction parameters and results are summarized in table 2-2.

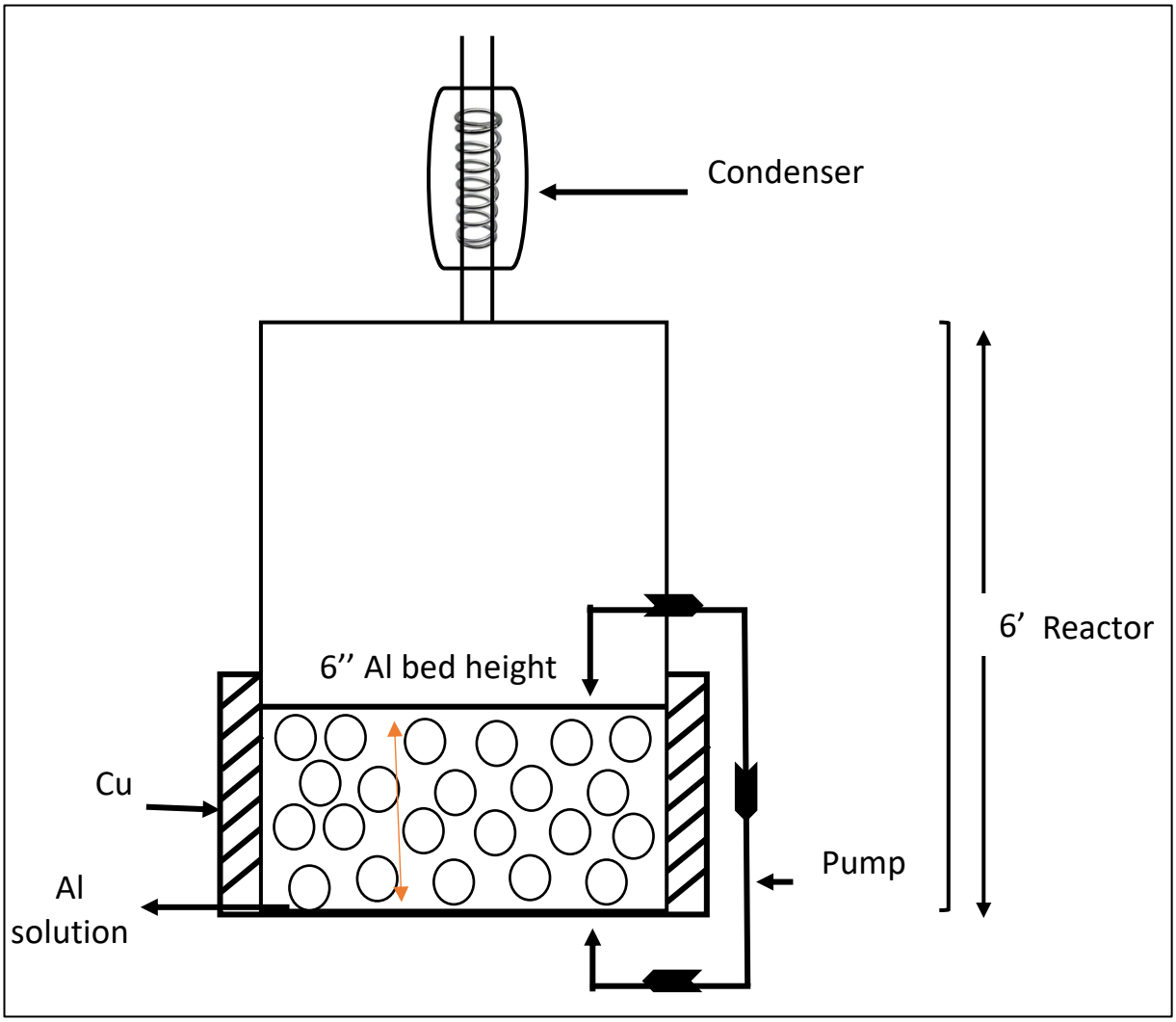

Figure 2-2: Schematic diagram for instrumental set-up for active circulation.

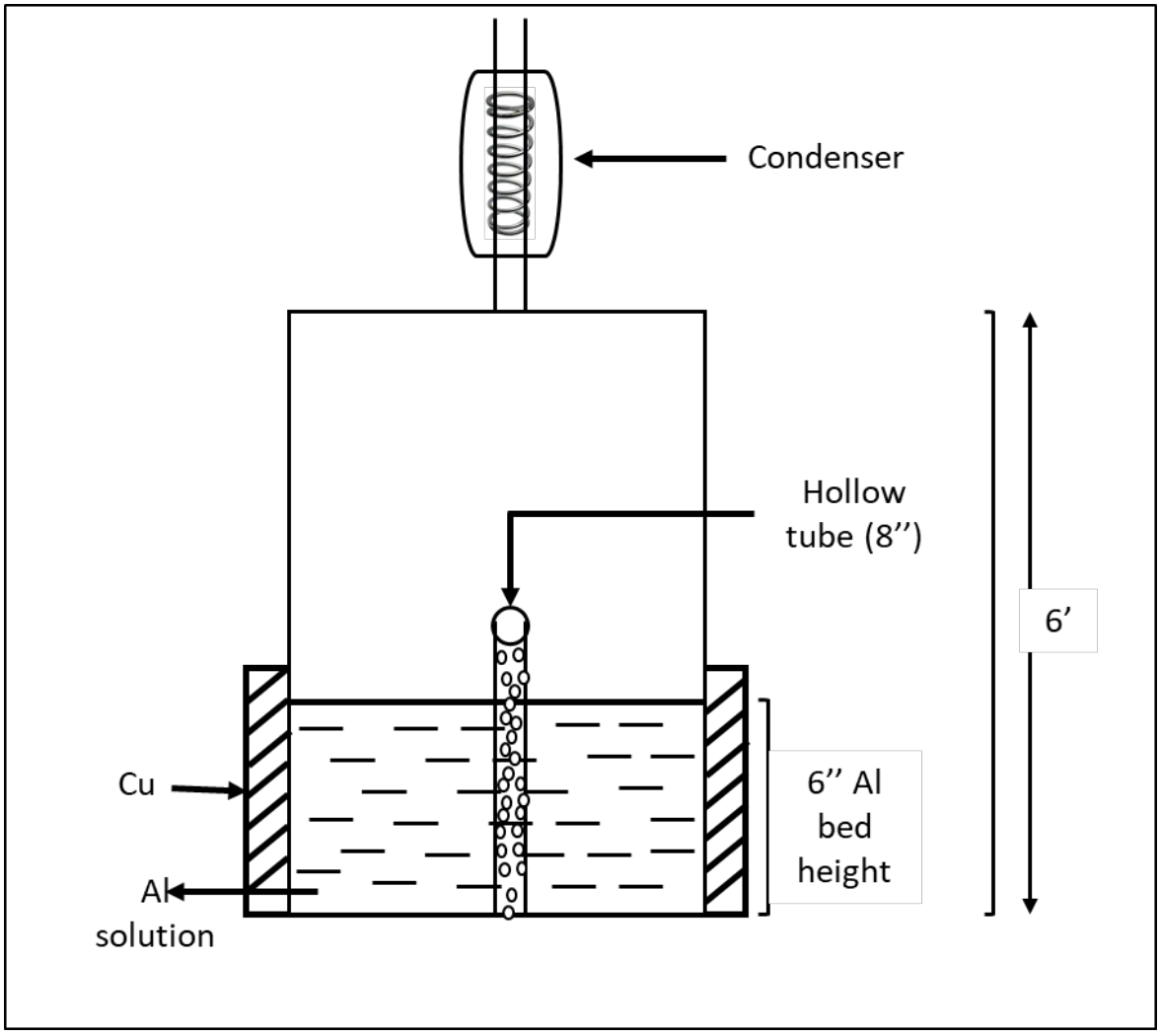

Figure 2-3: Schematic diagram for instrumental set-up for passive circulation.

Table 2-2: Summarized experimental conditions including the reaction parameters and results from section 2.1-2.4.

Experiment No.	Types of Al	Surface area (cm^2/g)	Reaction Conditions			Al dissolved (%)	Time (h)	Turbidity (NTU)
			HCl (20%) (mL)	Al (g)	Tempe-rature (℃)			
2.1	Pellet	3.95	167	78	85	76	72	13
	Pellet	3.95	167	78	100	90	72	22
2.2	Pellet	3.95	500	200 (150% excess)	100	75	46	17
	Pellet	4.4	500	200 (150% excess)	100	66	24	15
	Pellet	5.8	500	200 (150% excess)	100	56	22	26
2.3	Ingot	0.3	6900	2268 (150% excess)	100	90	160	10
	Pellet	3.95	6900	2268 (150% excess)	100	73	32	23
	Pellet	4.4	6900	2268 (150% excess)	100	61	30	25
	Pellet	5.8	6900	2268 (150% excess)	100	64	24	7.9
2.4	Pellet	5.8	278	385 (150% excess)	100	65	24	125
	Pellet	5.8	278	385 (150% excess)	100	62	24	34
	Pellet	5.8	278	385 (150% excess)	100	64	24	10

2.5 Results and Discussion

2.5.1 Preliminary Studies of the Reaction ‘take-off” and Temperature as a Function of Acid Strength

The reaction of HCl with aluminum produces an appreciable amount of heat, and the reaction speeds up as the temperature of the bath increases. The reaction will accelerate in a non-linear fashion until the solution boils, at which point no further temperature increase is possible as long as the aluminum solid remains covered with solution. We wanted to get a feel for how quickly the reaction takes-off when Al pellet and HCl acid of different strengths are mixed at room temperature. These conditions mimic the initial bath conditions of the industrial process

but at a much smaller scale. In a typical reaction, 100 mL of HCl is mixed with 19 g Al pellet (type II, 9.5 mm pellet) and the temperature monitored by a thermocouple. Three acid concentrations are analyzed: 8% HCl by mass (2.4 M), 10% HCl by mass (3 M), and 12% HCl by mass (3.6 M). All of the reactions follow the same procedure: A 250 mL glass beaker is charged with 100 mL HCl solution at room temperature and a thermocouple is inserted. After 10 minutes, 19 g Al pellets (9.5 mm pellet) are added, starting the reaction. Figure 2.2 shows how the temperature of each of the three different solutions changes with time. The important data from these reactions is reported in Table 2-3.

As seen in Figure 2-4, all three reactions are slow to increase in temperature until a certain lag period has been reached, and then the temperature rapidly increases to a maximum, and thereafter cools. The lag period is between 12-17 min and the maximum temperature achieved depends on the acid concentration. The lowest concentration (2.4 M) reached 80 °C, the 3.0 M HCl reached 90 °C, and the most concentrated 3.6 M HCl reached 100 °C.

It can be concluded that the maximum temperature reached in this set of experiments depends on the acid strength; however, the lag period is independent of the acid concentration. This exothermic reaction produces a lot of heat at the beginning, but the reaction quickly begins to cool after reaching a max temperature.

In this experiment, no effort was made to retain the heat produced; however, the hydrogen gas created does carry away much of the reaction heat. The rapid cooling of the reaction after reaching peak temperature shows that the reaction may not always generate enough heat to keep the solution at its maximum temperature (boiling), so it may require insulation to prevent excess heat loss. Lastly, the heat capacity of the reaction is highly dependent on the overall

reaction mass, and thus larger scale reactions are likely to hold heat (temperature) better than small scale ones. As these factors, along with the size of the pellet and the solid/liquid ratio, affect heat transfer, care must be taken when extrapolating data from smaller reactions to much larger ones.

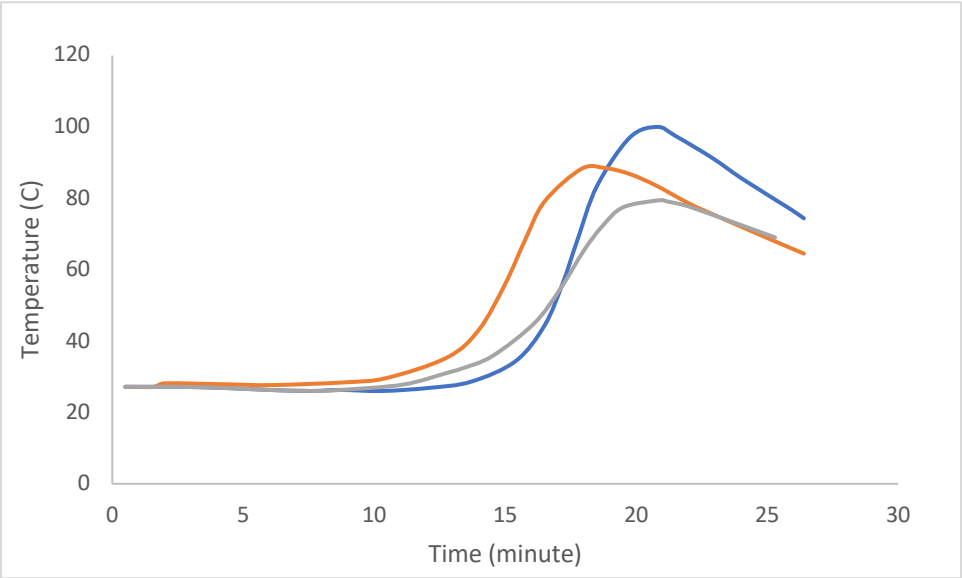

Figure 2-4: Monitoring the reaction temperature as a function of HCl concentration with time. The white line represents the temperature profile of the 8% HCl, the orange line represents the 10% HCl, and the blue line represents the 12% HCl. Each line shows the maximum temperature achieved through exothermic reaction of Al and HCl.

Table 2-3: Monitoring the reaction temperature as a function of HCl concentration during ACH synthesis.

Al metal (g)	Concentration of HCl (M)	Concentration of HCl (%)	Time to peak temp. (min.)	T_{max} (^{o}C)
19.26	2.4	8	11	80
19.23	3.0	10	10	90
19.33	3.6	12	11	100

If the ACH reaction is simply run at room temperature, it is unlikely to generate enough heat to run to completion (industry standard is SG =1.33) at any reasonable time period. As shown in Figure 2.5, the temperature profile for a mixture of reaction of 71 mL HCl (20%, 6.8 M) and 23.6 g of Al in a 250 mL round bottom flask shows a quick rise to 103 ^{o}C. After reaching this temperature, an additional 50 mL water is added to dilute the acid to the desired final concentration. After the water is added, the temperature briefly holds at 95 °C but is followed by a fairly rapid temperature decline to 35 °C over 50 min. The SG after 24 h reaction time is only ~1.03, so it is apparent that higher temperatures (80 °C or higher) must be maintained for the reaction to proceed at a reasonable rate.

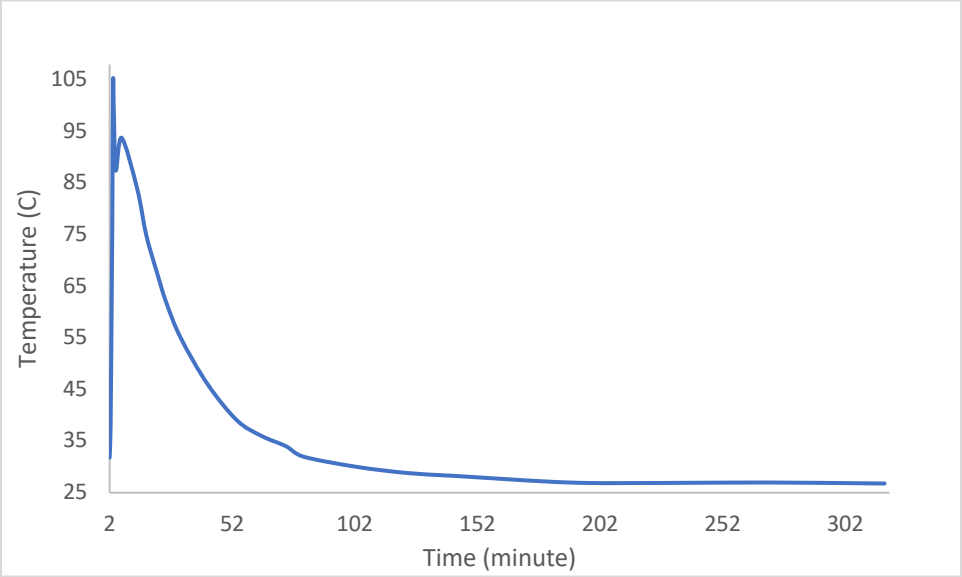

Figure 2-5: The temperature profile for the exothermic reaction of Al pellet with HCl showing the initial temperature peaks followed by the sudden drop to room temperature, without external heating or insulation of the reactor.

2.5.2 Effect of Temperature

The data from experiment 2.1 summarized in the table 2-4. For a small-scale reaction, there are no significant effects on the reaction rate when keeping the reaction at boiling condition (table 2-4). The produced H_2 gas during the reaction keeps the solution in stirring. The reaction progresses very slowly once the solution becomes denser (specific gravity ranges around 1.25-1.26). Total reaction time is about 72 hours, and the reaction rate is considerably slow for both reactions. However, the percentage of Al dissolved is much higher in the boiling condition (90% dissolved) compared to the non-boiling conditions (76% dissolved).

Table 2-4: Total reaction time to prepare ACH using varying condition in a small-scale reaction.

Exp. No.	Types of Al	Al dissolved (%)	Time (h)	Reaction condition
01	Pellet (9.5 mm)	90	72	Boiling temperature (100 °C)
02	Pellet (9.5 mm)	76	72	Non-boiling temperature (85-87 °C)

2.5.3 Effect of Surface Area on ACH Reaction Rate

With 150% excess Al, the reaction completed (specific gravity of the solution reached the desired 1.33) in about 46 hours compared to the 72 hours needed for the stoichiometric amount of Al loadings (table 2.5). The larger the surface area (smaller the size) of the Al pellet, the faster the reaction rate of ACH synthesis. The largest surface area Al pellet used in this study (5.76 cm^2/g, 3.2 mm type II pellet) took about half the time (22 h) to complete the reaction compared to the smallest surface area (3.95 cm^2/g, 9.5 mm type II) Al pellet, and $1/7^{th}$ the time to complete compared to the Al ingot (160 h, surface area 0.3 cm^2/g, type I Al).

The amount of Al dissolved (%) and the total reaction time (time required to achieve the specific gravity 1.33) are summarized for these reactions in the table 2-5.

Table 2-5: Comparison of the three different size Al pellets as a function of total reaction time to prepare ACH.

Types of Al	Surface area (cm^2/g)	Al dissolved (%)	Time (h)
Pellet (9.5 mm)	3.95	75	46
Pellet (6.4 mm)	4.36	66	24
Pellet (3.2 mm)	5.76	56	22

The specific gravity alone is not a measure of the reaction completeness as evidenced by the fact that unacceptable Al percentage and chloride ion percentage can be found even with specific gravity readings within the desired range. Although specific gravity is an accurate measure of the reaction completeness, the 150% excess Al is needed to ensure a high (23-24%) Al and low (7-8%) Cl^- content that meets ACH specifications because Al and Cl^- percentage are very sensitive to Al loading.

However, the procedures followed in these experiments are for small scale reactions and are not directly applicable to industrial processes. The current industrial ingot process (C-KOE, a commercial company for ACH production), yields 6000 gal of ACH after a 5-day procedure starting with 16,000 lb. Aluminum ingots, and only 62% of the Al is converted to ACH. As because the goal of this study is improving the current ingot process by replacing the ingot with aluminum pellet, first it must be determined if the data collected from the experiments 2.2 can approximate industrial data. As this work was not done on industrial scale, the product yield was converted to what would be expected if the reaction were done in the same reactor using essentially the same amounts of aluminum, water, and acid. First, 6000 gal ACH is set as 100%

yield, which is what is currently obtained using the industrial ingot process. Therefore, the number of gallons of ACH produced and how this compares to the number of gallons produced by the current ingot process can be calculated. Also, the productivity of the reaction can be calculated by dividing the quantity of product by the time it took to produce it; this is reported in gallons ACH produced per hour of reaction time.

Table 2-6: Productivity (gallon/h) comparison of the produced ACH using different sizes of Al pellet and Al ingot.

Types of Al	Surface area (cm^2/g)	Al dissolved (%)	Time (h)	ACH yield[a] (gallon)	Productivity[b] (gal/h)
Ingot	0.27	62	120	6000	50
Pellet (9.5 mm)	3.95	75	46	7258	158
Pellet (6.4 mm)	4.36	66	24	6800	283

a) Estimate of the amount of ACH that would have been produced in a single batch, scaled to compare with the current ingot process data. b) Productivity is the yield in gallons divided by the reaction time.

As reported in table 2-6, one benefit of using aluminum pellets with more surface area than ingots are a 2- to 5.7-fold increase in productivity. As with all of the experiments in this study, the time of the reaction is the time for the solution to reach a specific gravity (SG) of 1.33.

The effect of surface area on ACH reaction rate is further investigated with larger scale reaction (experiment 2.3). The large-scale studies show that ACH production using large aluminum ingots typically take anywhere from 3-6 days, whereas ACH can be produced from pellets in as little as 24 hours, depending on the pellet size and process conditions.

The relative rate of the reaction is 6.5 times faster for the highest surface area used in this study compared to the Al ingot.

One of the specifications of Industrial grade ACH is turbidity, which required to be lower than 50 NTU. Even though ACH synthesized in small scale reactions always met the turbidity requirement in this study, ACH from large scale reactions suffer from higher turbidity (>50 NTU). The data from experiment 2.3 summarized in the following table 2-7.

Table 2-7: Total reaction time and productivity for Al pellet with varying surface area in a large-scale (3 gallon) ACH synthesis reaction.

Types of Al	Surface area (cm^2/g)	Al dissolved (%)	Time (h)	Productivity[a] (mol/L.h)	Relative rate[b]
Ingot	0.27	90	160	0.036	1
Pellet (9.5 mm)	3.95	73	32	0.16	4.5
Pellet (6.4 mm)	4.36	61	30	0.19	5.3
Pellet (3.2 mm)	5.76	64	24	0.24	6.5

a) Productivity data is calculated by plotting the $[Al^{3+}]$ as determined by ICP-OES versus time and fitting a line to the data. The rate is the slope of this line and is reported in $molL^{-1}h^{-1}$ of $[Al^{3+}]$ (figure 2-6). b) Relative rate is the rate of a given reaction relative to that of the ingot reaction and is obtained by dividing the rate of any given run by the rate of 0.036.

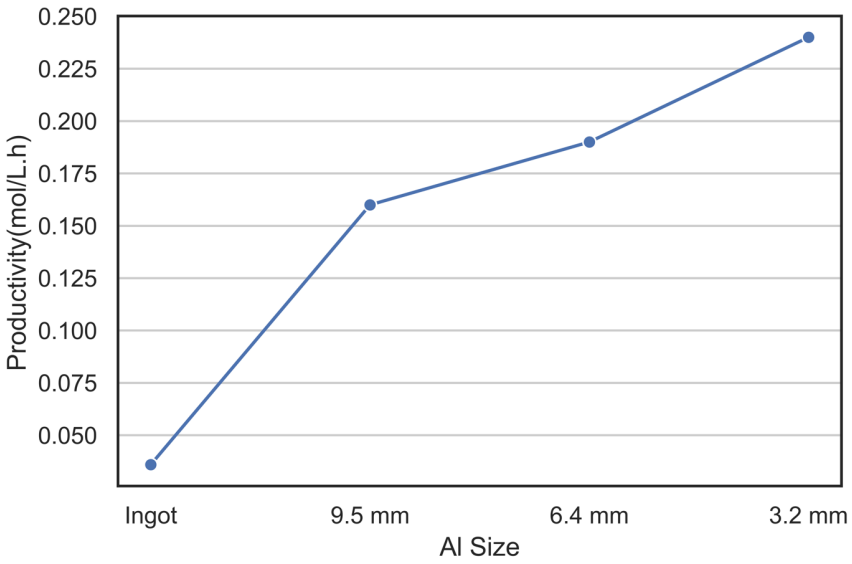

Figure 2-6: Productivity (mol/L.h) of ACH synthesis for varying sizes of Al pellet in a large-scale reaction (3 gallon).

2.5.4 Factors Affecting Turbidity of ACH Solution

The turbidity of the ACH is an important factor and industrial specifications require it to be less than 50 NTU. In large scale studies, problems with ACH turbidity became apparent and were traced to issues arising from the thick pellet bed not allowing good circulation of the acid solution during the reaction.

Under conditions in which the reaction bed is simply left in contact with the acid solution, the reaction with acid progresses until the solution reaches boiling and significant amounts of hydrogen gas and steam are released from within the pellet bed. As only 25% of the total bed volume is accessible to the acid solution (the void volume), the large volume of gas displaces a significant portion of the acid solution. While the weight of the acid solution constantly pushes the solution down into the bed, the positive gas pressure is enough to leave insufficiently hydrated pockets within the bed, which probably results in ACH and higher aluminum oxides crystallizing out onto the bed pellets. These crystals effectively clog the bottom of the bed. This

is apparent as a white solid found on the aluminum pellet bones post reaction and in some cases causes large clumps of pellet bones to stick together. During the ACH reaction, some of this solid is dislodged by the bed agitation and bubbles and becomes suspended in the ACH product.

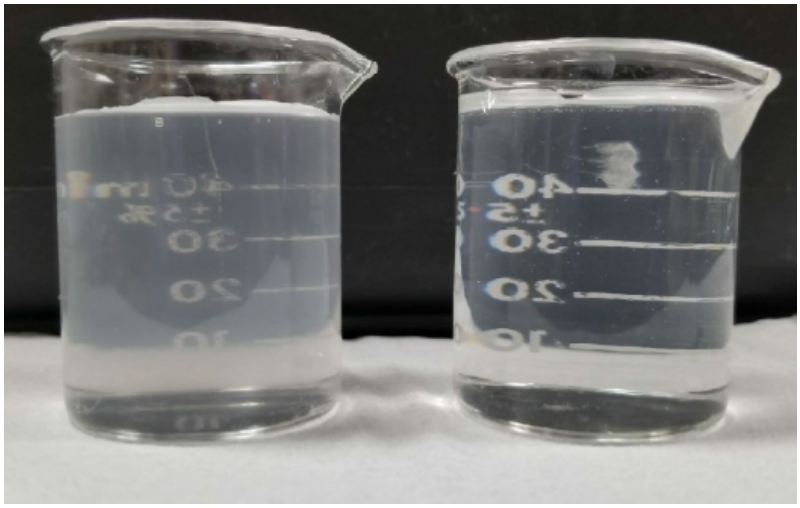

Figure 2-7: a. ACH with turbidity>50 and b. ACH with turbidity<50.

These fine suspended aluminum oxide particles do not all readily dissolve to reform ACH, and the result is a high turbidity in the ACH product. A series of lab scale reactions were performed to see if circulating the acid solution from the top to the bottom of the pellet bed would alleviate this problem.

The experiment with external heating to insure the fluid in the bed would be boiling. This resulted in an ACH product with high turbidity that was out of specifications even after 24 hours (experiment 2.4.1). Solid (crystalized) ACH was observed in the bottom of the bed making the bones very difficult to remove.

The combination of deep pellet beds (8-inches and more) and boiling result in an ACH product that meets SG specifications but fails turbidity specifications. This situation leads to solid ACH in the bed, which may be responsible for the increased turbidity.

To avoid dehydrating and crystalizing of ACH, an approach of circulating liquid to the bottom of the reactor bed has considered. The results in Table 2-8 show that circulating the fluid to the bottom of the bed eliminates the high turbidity that results from using a deep bed of pellets (both active and passive circulation).

Table 2-8: ACH synthesis data for the experiments in terms of circulation of fluids through the reactor.

Types	Temperature (°C)	Specific gravity	Turbidity (NTU)
No circulation	102	1.34	125
Active circulation	100	1.33	34
Passive circulation	100	1.33	10

2.5.5 Kinetic study

In this study, ACH is synthesized by reacting metallic aluminum and hydrochloric acid at boiling temperature (100 °C). The optimum parameters for ACH synthesis was determined in experiments 2.1 – 2.4: 150% excess metallic Al, boiling temperature (100 °C) and 20% HCl. Specific gravity of the solution is monitored throughout the reaction and once it reaches 1.33, the reaction is stopped by cooling down the solution. Using these optimized reaction conditions, the ACH reaction rate increased significantly with the increased surface area of the metallic Al. Using the data from experiments 2.3, a kinetic relation of the surface area of the Al and the reaction rate of the ACH synthesis can be established. To determine the concentration of Al^{3+} in the ACH solution, aliquots were collected at regular intervals during the experiments and analyzed using the ICP-OES. The concentration of Al^{3+} is plotted against time to calculate the rate of the reaction (Figure 2-8). The reaction is assumed to be isothermal. The slope of the

graph gives the rate of the reaction. In addition, figure 2-6 shows the rate of dissolution of Al in the solution. The data shows that the aluminum pellets react faster than the aluminum ingot. The smallest pellets used in this study (3.2 mm) react 6.5 times faster than the aluminum ingot, whereas the moderate size pellets (6.4 mm) react 5.3 times faster than the ingot.

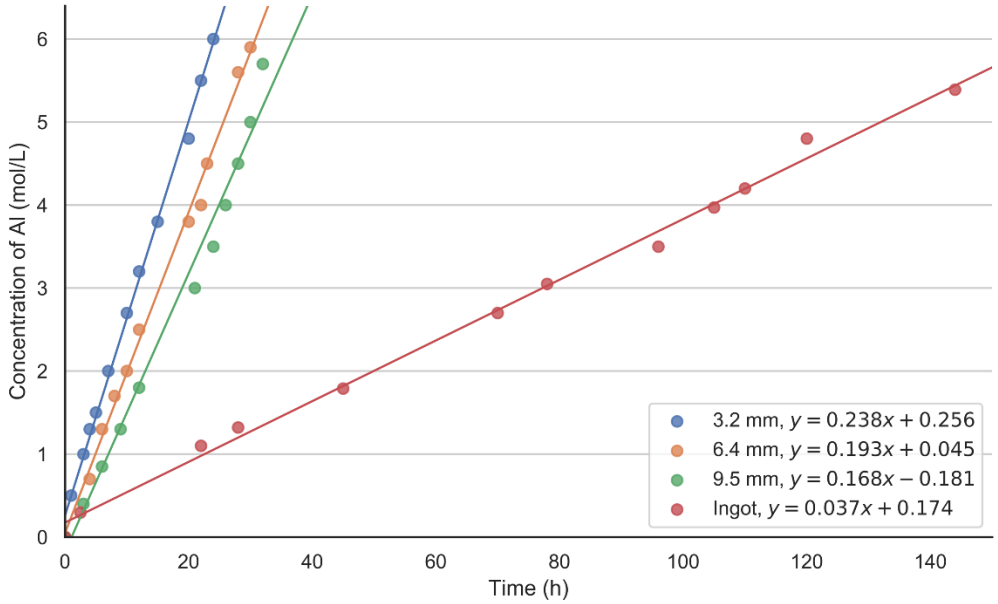

Figure 2-8: Concentration of Al in solution vs time for both aluminum pellets and ingot.

The exothermic reaction of metallic Al and HCl is:

$$2Al + HCl + 7H_2O \longrightarrow Al_2(OH)_5Cl{\cdot}2H_2O + 3\,H_2$$

The rate equation of ACH synthesis can be written as follows:

$$Rate = k[H_3O^+]_i[Al_{SA}] \quad ; [Al_{SA}] = \text{Surface area of the Al}$$

$$[H_3O^+]_i = \text{Initial acid concentration}$$

As the initial concentration of the acid is constant, the rate equation can be re-written as

$$Rate = k_{obs}[Al_{SA}] \; ; \; k_{obs} = k[H_3O^+]_I \; (k_{obs} = \text{observed rate constant})$$

The concentration of the dissolved aluminum increases with time and follows a zero-order reaction rate (figure 2.7). The observed rate can be expressed as:

$$K_{obs} = ([Al^{3+}]/t) \quad \text{..... (Eqn. 1)}$$

The rate constant can be determined from the slope of the graph (table 2-8).

It is possible to establish a relationship between the surface of the Al and the rate constant of the reaction using this experimental value. A plot of the calculated rate constant as a function of surface area (figure 2-9) gives the following equation:

K = 0.037X+ 0.03, which can be expressed as:

Rate of the reaction = 0.037(surface area) + C …… (Eqn. 2)

Table 2-8: Experimental rate constant of ACH synthesis for different sizes of Al pellets and ingot.

Sizes of Al	Surface area (cm^2/g)	Equation	Rate constant, K_{obs} ($[Al^{3+}]/t$)
Ingot	0.3	Y= 0.036X+.17	0.036
3.2 mm pellet	5.8	Y=0.24X+.25	0.24
6.4 mm pellet	4.4	Y=0.19X+.04	0.19
9.5 mm pellet	3.9	Y=0.17X-0.18	0.17

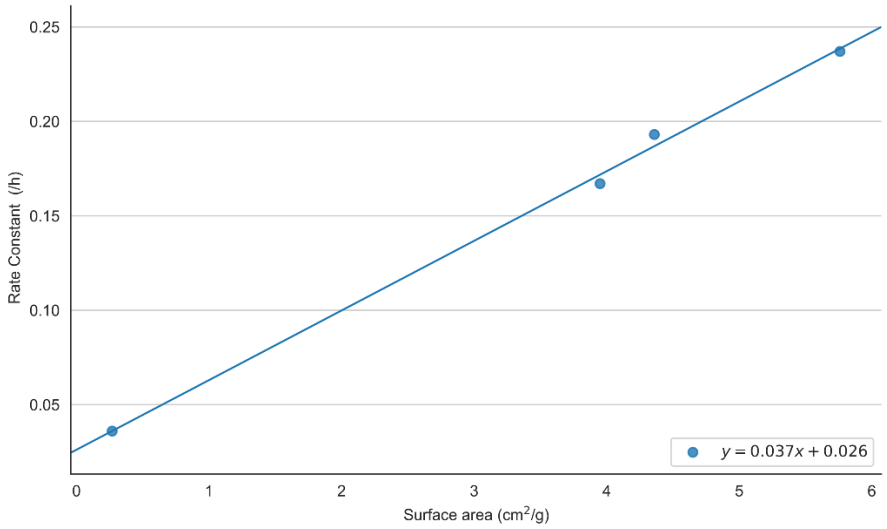

Figure 2-9: Reaction rate determination as a function of surface area for different sizes of Al pellets and ingot.

Therefore, the rate of the reaction is directly related to the surface area of the metallic Al, and the reaction rate of the ACH synthesis can be derived using this equation if the other parameters are exactly the same as in this study (acid concentration, temperature).

2.6 Conclusion

Aluminum ingots or pellets are used to make ACH in a heterogeneous reaction with aqueous hydrochloric acid. The reaction is exothermic, produces copious amounts of hydrogen gas, and ultimately generates product grade ACH when the specific gravity (SG) of the solution reaches 1.33 to 1.35. Other product specifications include 7.90 – 8.40% chloride by mass, 23-24% Al_2O_3 by mass, and turbidity (<50 NTU). Two conditions, aside from meeting product specifications, were imposed. In experiment 2.1 (a), the reaction temperature was not allowed to exceed 87 °C. In experiment 2.1 (b), the reaction was allowed to boil. The results show that if the temperature is fixed at 87 °C or below, the rate of heat removal from the reactor determines the overall speed of the reaction. Reactor designs with high rates of heat dissipation or with the ability to withstand boiling conditions are needed to realize the full potential of aluminum pellets. Under boiling

conditions, heat dissipation is no longer the driver of the reaction rate, and a substantial (~ 6-fold increase in rate) can be realized using pellets over ingots. Boiling was not observed to hurt the product quality or turbidity; however, it is important the Al pellets always be covered with liquid, or the turbidity can suffer. In all reactions, whether using pellets or ingots, a black precipitate, which was determined to be a fine iron powder, formed and settled to the bottom of the reactor. The relative amount of the iron powder observed directly correlates with the iron content of the Al sample. If this precipitate is not removed by settling or filtration, the turbidity of the product is considerably increased. There are substantial opportunities to reduce batch reaction time by using Al pellets in lieu of ingots and by allowing the reaction temperature to reach boiling to carry off the excess reaction heat. In the experiments in which boiling was permitted to occur the maximum temperature reached was 105 °C (221°F). As stated previously, boiling has no detrimental impact on product quality or turbidity. The rate of reaction is highly dependent upon the size of the pellets in terms of the surface area. The smaller the pellet, the higher the surface area and the faster the rate of reaction.

Chapter 3

Investigation of the Effect of Metal Impurities on Aluminum Chlorohydrate (ACH) Synthesis

3.1 Introduction

Aluminum chlorohydrate (ACH) is an active ingredient of many antiperspirant and deodorants. It is also used in water treatment to remove dissolved organic matters and small impurities particles. The widely used industrial method of preparing ACH is redox reaction of metallic Al and hydrochloric acid.[30] Following half-reactions occur during the synthesis:

$$\text{Oxidation half reaction: } Al \longrightarrow Al^{3+} + 3e^-$$

$$\text{Reduction half reaction: } 2H^+ + 2e^- \longrightarrow H_2$$

Al ingot or pellet used for synthesizing ACH contains trace metallic impurities mixed with Al. Among these impurities (Fe, Si, Co, Ni, Mg), Fe and Si are the major constituents (1-900 ppm). Depending on the purity of Al used for the ACH synthesis, the Fe content in ACH powder or solution also varies (75-200 ppm). Klug et al.[36] reported that the low-iron ACH (~ 20 ppm) is more effective in antiperspirant activity than iron rich ACH. The typical ACH solution used for cosmetics contains about 75 ppm Fe, whereas for water treatment it is 100 ppm.

High purity Al (99.999%) can be used to prepare ACH in order to get low iron product. However, it is found that ACH reaction rate is significantly lower (about 6 times) with high purity Al (99.999%) than less pure Al (99.824%). Apparently, the metal impurities (mostly Fe) mixed with Al, significantly affect the ACH reaction rate.

In the process of electrochemical or photochemical generation of H_2, using a metallic co-catalyst as a redox mediator is very common and highly efficient.[37-41] The various noble metal (Pt, Au, and Pd) and relatively cheaper and earth abundant metal (Fe, Co, Ni, Mo) co-catalysts facilitate the charge separation and surface reaction, which consequently increases the catalytic activity.[42-50] One of the better co-catalysts is Ni-based, which display excellent activity in terms of H_2 generation.[51-60] Ni and its compounds are well-known for their robust activities in a wide range of both homogeneous and heterogeneous reactions.[61] Because of their ability to adopt multiple oxidation states and to form complexes, uses of Ni and their compounds as catalyst are well recognized.[62-68] As because the ACH synthesis reaction proceed with production of significant amount of H_2 gas, the transition metal present in Al can act as a co-catalyst and facilitate the reaction rate.

To increase the efficiency of the ACH, it is critical to identify how and why the metallic impurities present in Al affecting the reaction rate. The effect of metallic impurities present in Al is comprehensively examined in this study. Moreover, different transition metals such as Fe, Mn, Cu, and Ni added to the ACH reaction and the reaction rate is monitored against the types of metals added.

3.2 Experimental

3.2.1 Materials

Total 4 different types of Al pellets and grains used in this study. Type I and II Al pellet has same surface area (5.8 cm^2/g) but differs in the purity. Type I is more pure (99.999%) than type II (99.824%) pellet. Similarly, type III and IV Al grains has same surface area (42 cm^2/g) with

different purity. The detail composition of Al pellets and grains are given below in table 3-1 and 3-2.

Table 3-1: Various types of Al pellets and grains with their size, surface area, and composition.

	Types of Al	Surface area (cm^2/g)	Al %
I	Pellet (3.2 mm)	5.8	99.999
II	Pellet (3.2 mm)	5.8	99.824
II	Grain	42	99.922
IV	Grain	42	99.804

Table 3-2: Amount of impurity content in Al pellets, and grains used in this study for ACH synthesis.

Types of Al		Fe (ppm)	Si (ppm)	Mg (ppm)	Ni (ppm)	Zn (ppm)
I	Pellet	1	7	1	0	0
II	Pellet	850	500	10	40	10
III	Grain	275	200	4	30	20
IV	Grain	999	504	10	60	0

3.2.2 Sample Preparation

The reaction parameters are kept at the optimum condition (150% excess Al, boiling temperature (100 °C), 20% HCl). About 220.0 g of aluminum pellet, or grain is added to 449.0 mL 20% HCl and 475.0 mL water in a round-bottom flask. To avoid the vigorousness of the reaction, hydrochloric acid is added in a stepwise manner over an hour period. Once the reaction steadies and the temperature decrease to 80 °C, external heating is started to keep the temperature at boiling (100 °C) throughout the reaction time. The reaction is terminated once the solution's specific gravity reaches 1.33. Finally, the reaction is cooled down to room temperature.

In order to examine the transition metal effect on ACH reaction rate, small amount (800-2400 ppm) of metallic salt (Fe, Mn, Cu and Ni) added to the reaction at the beginning of the synthesis (table 3.3).

To investigate the effect of the metal impurities present in the aluminum, 2 different Al pellets, and 2 different grains, each with a unique amount of impurity, are used for ACH synthesis (table 3-1 & 3-2). They all contain different metal particles, mostly on a very small scale (1-900 ppm).

Fe and Si are the most dominant impurities in the aluminum used in experiment 12, though the main focus is on Fe impurity in this study.

All the experiments carried on can be divided into three major parts: experiment 3.1, 3.2 and 3.3 (table 3-3). Experiments 3.1 focuses on the different types of impure Al pellets and grains, experiments 3.2 focuses on the effect of externally added Fe on these pellets and grains, and finally, experiments 3.3 focuses on the effect of different transition metal on ACH synthesis.

Table 3-3: Summarized experimental conditions for ACH synthesis conducted in this study.

Experiment No.	Types of Al	Surface area (cm^2/g)	Al (%)	Fe (ppm)	Externally added metal
3.1	Pellet	5.8	99.999	1	-
	Pellet	5.8	99.824	850	-
	Grain	42	99.922	275	-
	Grain	42	99.804	999	-
3.2	Pellet	5.8	99.999	1	Fe
	Pellet	5.8	99.824	850	Fe
	Grain	42	99.922	275	Fe
	Grain	42	99.804	999	Fe
3.3	Pellet	5.8	99.824	850	Fe
	Pellet	5.8	99.824	850	Mn
	Pellet	5.8	99.824	850	Cu
	Pellet	5.8	99.824	850	Ni

3.3 Results and Discussion

3.3.1 Effect of Metallic Impurity on ACH Reaction Rate

The purest aluminum pellet (type 1) used for this experiment (99.999% pure) took about 138 hours to complete the reaction, which is 6.5 times more than that of the type II aluminum pellet (99.824% pure), which took about 21 hours to complete, even though all of the other reaction parameters are the same, including the surface area (5.8 cm^2/g).

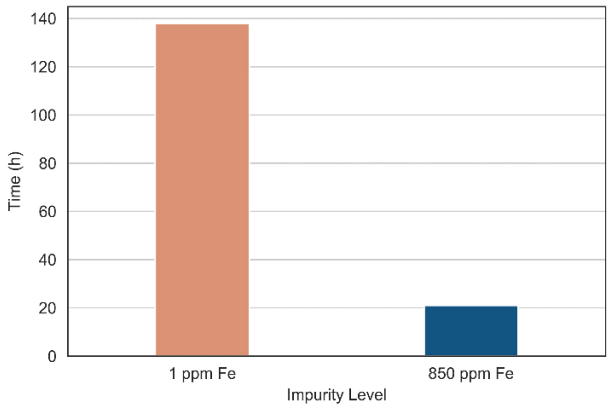

Figure 3-1: Total reaction time of ACH synthesis for different types of Al pellet (type I, 99.999% Al, 1 ppm Fe and type II, 99.824% Al, 850 ppm Fe).

Because specific gravity is used to determine reaction completion (SG 1.33 = completion), specific gravity is plotted with time for both Al pellets (figure 3-2). For the pure type I Al pellet, the change in specific gravity is steadier than for the type II pellet.

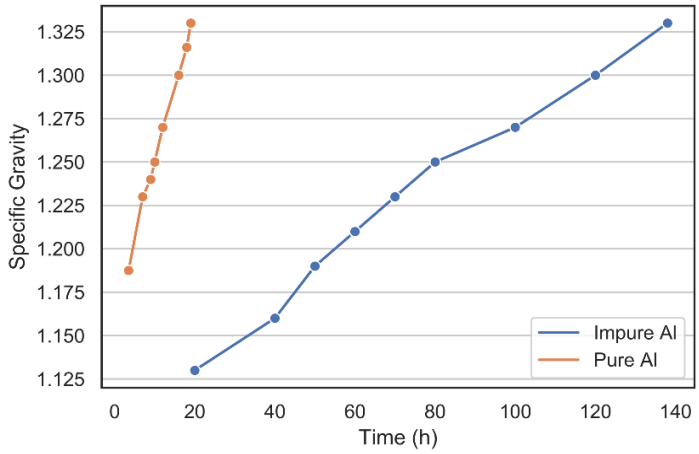

Figure 3-2: Changes of specific gravity with time for ACH synthesis; Type I Al contains 99.999% pure Al and 1 ppm Fe, and type II Al contains 99.824% pure Al and 850 ppm Fe.

The type III and IV Al grains each have the same surface area but different purity levels. Type III, the less impure grain, took more time to reach reaction completion than the type IV grain (figure 3-3). Data from experiments 3.1 are summarized in table 3-4. The total reaction time for all four types of aluminum varies from 19 to 138 hours depending on the type of Al used in the experiment, even though all the other parameters of experiment remain the same.

Table 3-4: Total reaction hours of ACH synthesis using different kinds of Al pellets and grains in terms of Fe impurity content.

Types of Al		Surface area (cm^2/g)	Iron content (ppm)	Reaction time (h)
I	Pellet	5.8	1	138
II	Pellet	5.8	850	21
III	Grain	42	275	31
IV	Grain	42	999	19.5

The total reaction time (time required to reach the specific gravity of the solution to 1.33) either increased or decreased as a function of iron content in the aluminum pellet. The reaction rate increased significantly with the higher Fe impurity level.

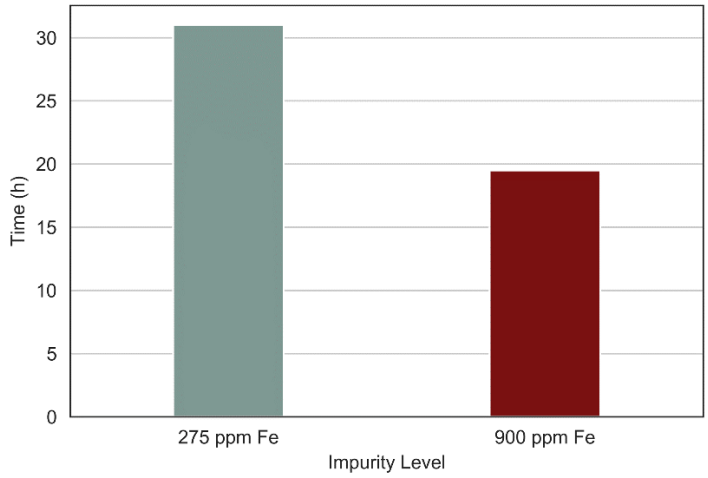

Figure 3-3: Total reaction time of ACH synthesis using Al grain with varying Fe impurity content.

3.3.2 Effect of Externally Added Fe on ACH Reaction Rate

To further investigate the impact of iron impurity on the ACH synthesis reaction, different amounts of iron salt were added to the initial reaction solution and the reaction time was monitored. The reaction times for all four types of aluminum (pellets and grain) with the externally added iron salt are summarized in the table 3-5.

Table 3-5: Total reaction time for ACH synthesis using different types of Al pellets and grains with externally added Fe.

Types of Al		Surface area (cm^2/g)	Iron content (ppm)	Externally added Fe (ppm)	Reaction time (h)
I	Pellet	5.8	1	2400	38
II	Pellet	5.8	850	2400	13
III	Grain	42	275	2400	21
IV	Grain	42	999	2400	12

The ACH reaction rate increased with the addition of iron salt to the solution. The most significant improvement can be seen for the purest aluminum pellets (type I = 99.999% pure) used in this study; the reaction time decreased from 138 to 38 hours, which means the reaction happens 3.5 times faster with the externally added iron salt.

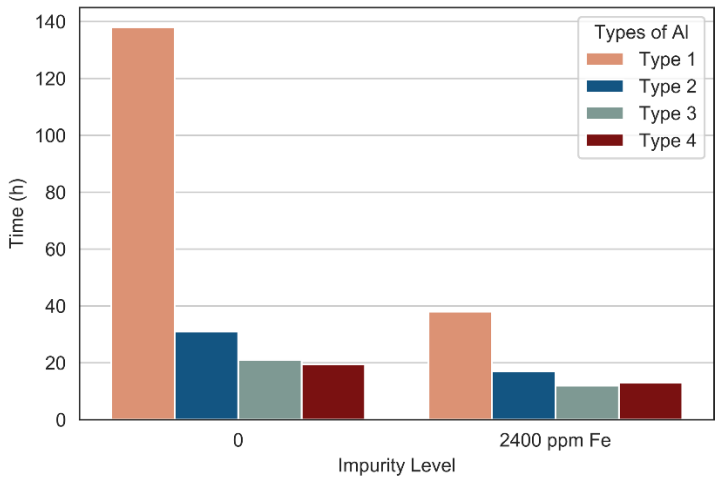

Figure 3-4: Total reaction time of ACH synthesis for all four types of Al used with externally added Fe-salt. Type I Al pellet contains 1 ppm Fe, type II pellets contains 850 ppm Fe, type III Al grain contain 275 ppm Fe and type IV contains 999 ppm of Fe as impurity with the Al.

3.3.3 Optimizing the Fe-loadings in ACH Synthesis

To optimize the amount of iron impurity added externally to the solution, in experiment 3.2 different amounts of iron salt are added to the type II aluminum pellet (3.2 mm size). The results are summarized in the following table (table 3-6).

Table 3-6: Total reaction time of ACH synthesis using various loadings of Fe into Al pellet.

Surface area (cm^2/g)	Fe content (ppm)	Externally added Fe (ppm)	Reaction Time (h)
5.8	850	0	21
		800	15.5
		1600	13
		2400	13

The specific gravity changes for both the reactions follows a similar trend, with the only exception of a relatively higher rate for the externally added iron solution (figure 3-5). Another noticeable factor in this experiment is that the reaction rate does not change after reaching the saturated level of iron salt addition. The reaction times for both the 1600 ppm and 2400 ppm (externally added) iron are the same, which means that the addition of external impurity increases the reaction rate; however, at the saturation point, adding more impurity does not affect the reaction rate in any way, meaning there is no point in adding further impurity (figure 3-6).

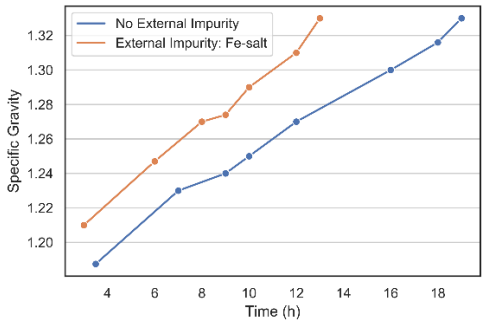

Figure 3-5: Changes of specific gravity as a function of time with and without externally Fe loadings in the ACH synthesis (type II Al pellet, 99.824% Al).

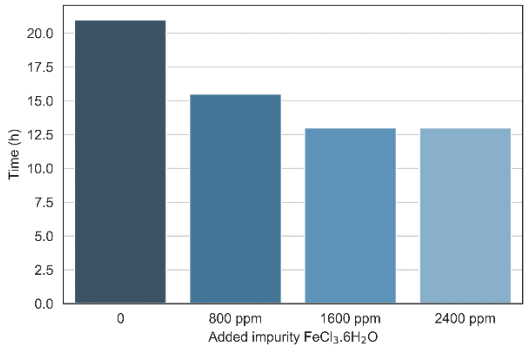

Figure 3-6: Total reaction time for various Fe loadings in 3.2 mm sized Al pellet (type II, 99.824% Al).

3.3.4 Effect of Transition Metals on ACH Reaction Rate

Along with Fe, Cu, Co, and Ni are investigated in the synthesis of ACH as co-catalysts. Type II Al pellets (99.824% Al, surface area 5.8 cm^2/g) are used in experiment 3.3. This pellet has 850 ppm of Fe impurity along with other trace amounts of metals. $FeSO_4 \cdot 7H_2O$, $Co(NO_3)_2 \cdot 6H_2O$, $CuSO_4 \cdot 5H_2O$ and $NiSO_4 \cdot 6H_2O$ are externally added to the reaction solution at ppm level, and their effect on the rate of the ACH reaction is observed. The total reaction time (time required to obtain the specific gravity 1.33) varies for the four transition metals (figure 3-7). Ni showed the most pronounced effect on the rate of the ACH reaction; it increases the reaction rate by 5.5 times (table 3-7). Co and Fe affect the reaction rate in a similar way, but less so than for Ni. Finally, Cu has the least effect on the reaction rate; in fact, this effect is negligible.

Table 3-7: Total reaction time for ACH synthesis using various transition metals with 3.2 mm Al pellet.

Surface area (cm^2/g)	Fe content (ppm)	Externally added salt	Externally added salt amount (ppm)	Reaction time (h)
5.8	850	-	0	21
		Fe	2400	13
		Co	2400	14
		Cu	2400	19
		Ni	2400	4

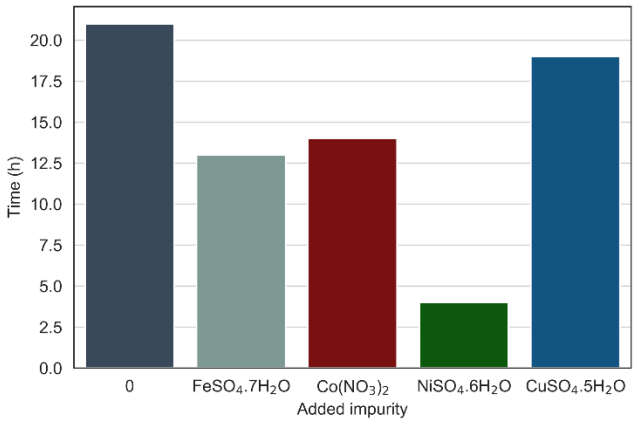

Figure 3-7: Total reaction time of ACH synthesis using various transition metals added to the 3.2 mm sized Al pellets.

3.3.5 Optimizing Ni-loadings in ACH Synthesis

Among the transition metals studied, Ni is the most efficient in increasing the reaction rate of ACH formation. Because of this, the effects of different amounts of Ni on the reaction rate are

also studied: 800, 1600, and 2400 ppm. The results show that specific gravity changes follow almost exactly the same trend (figure 3-8).

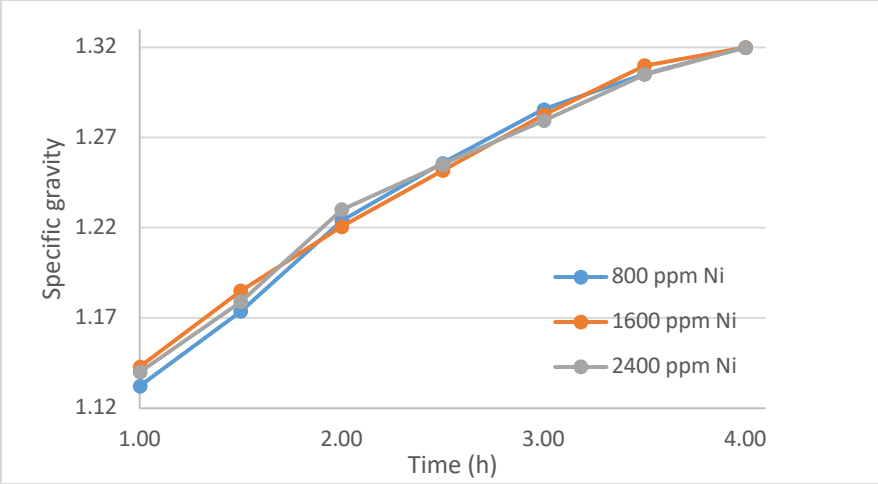

Figure 3-8: Changes of specific gravity with time for varying loadings of Ni in 3.2 mm Al pellet.

As can be seen in table 3-8, the rate of reaction does not change with each increment of Ni-loadings. The three reactions completed in 4 hours (time required to reach to the specific gravity 1.33), which indicates that the reaction becomes saturated after some level of Ni-salt addition.

Table 3-8: Summarized data for various Ni-loadings in 3.2 mm Al pellets for ACH synthesis.

Surface area (cm^2/g)	Fe content (ppm)	Externally added Ni (ppm)	Reaction time (h)
5.8	850	800	4
		1600	4
		2400	4

The effect of Ni on the ACH reaction rate while using the purest aluminum (99.999% Al) is investigated in experiment 18. Ni shows the most dramatic increase in the reaction rate with this pellet. The reaction time using Ni and the type I pellet decreased from 138 hours (type I with no added salt) to 24 hours, whereas Fe with the type I pellet decreased the reaction rate to 38 hours (figure 3-9). Therefore, the addition of the transition metal salts shows a significant effect on the reaction rate of ACH synthesis, and Ni has the most pronounced effect of the four transition metals studied here.

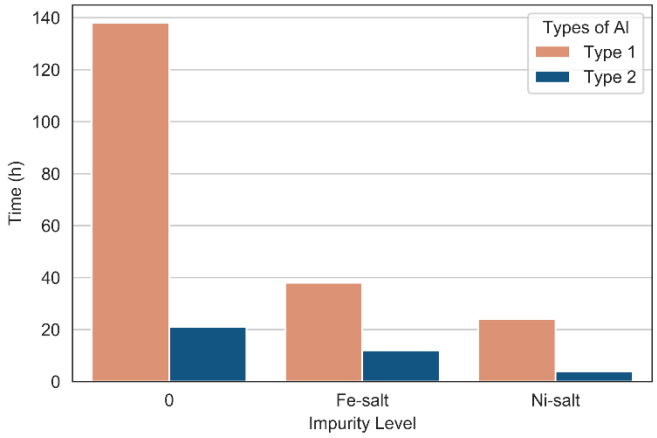

Figure 3-9: Total reaction time for Al pellet with Fe and Ni salt. Type I Al pellet has 99.999% Al and 1 ppm Fe impurity, and type II has 99.824% Al and 850 ppm Fe impurity.

The reactivity of Ni over the other transition metals in ACH synthesis can also be explained in terms of H_2 production. From experiment 3.3, the amount of H_2 gas produced during ACH synthesis is plotted as a function of time in figure 3-10.

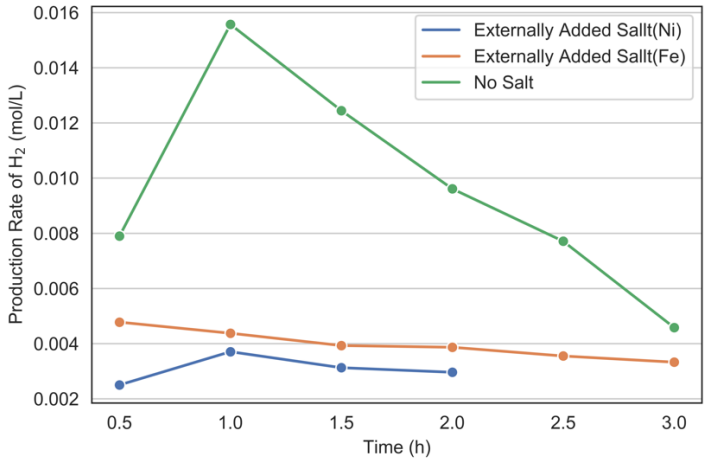

Figure 3-10: Production rate of H_2 gas vs. time with and without the addition of external transition metals (Fe and Ni-salt) in ACH synthesis reaction using type II Al pellets (3.2 mm, 99.824% Al).

The production of H_2 gas decreases with time in all of the cases. The production of H_2 is relatively lower when there is no externally added salt in the system as compared to the Fe-added reaction. However, a significant rise in the H_2 production can be seen for the Ni promoted reaction, which also aligns with the fact that the Ni-catalyzed reaction completes in only 4 hours.

3.3.6 EDX Spectra and SEM Imaging of Al Pellet

The leftover Al pellet after the ACH synthesis reaction was collected and analyzed using the EDX (Energy Dispersive X-ray Spectroscopy) spectra and SEM (Scanning Electron Microscopy) to investigate the fate of the externally added metallic salt during the reaction. The SEM image shows the morphology of the Al pellet surface after the ACH synthesis. The pure Al pellet showed much more of a regular shape (figure 3-14(b)) compared to the impure one (3-14(a)). The EDX spectra showed that the externally added salt deposited on the Al pellet (figure 3-11-3-13). Formation of the metallic particle observed during the ACH synthesis (collected through the magnetic stir bar) and this metallic particle deposited into the Al pellet.

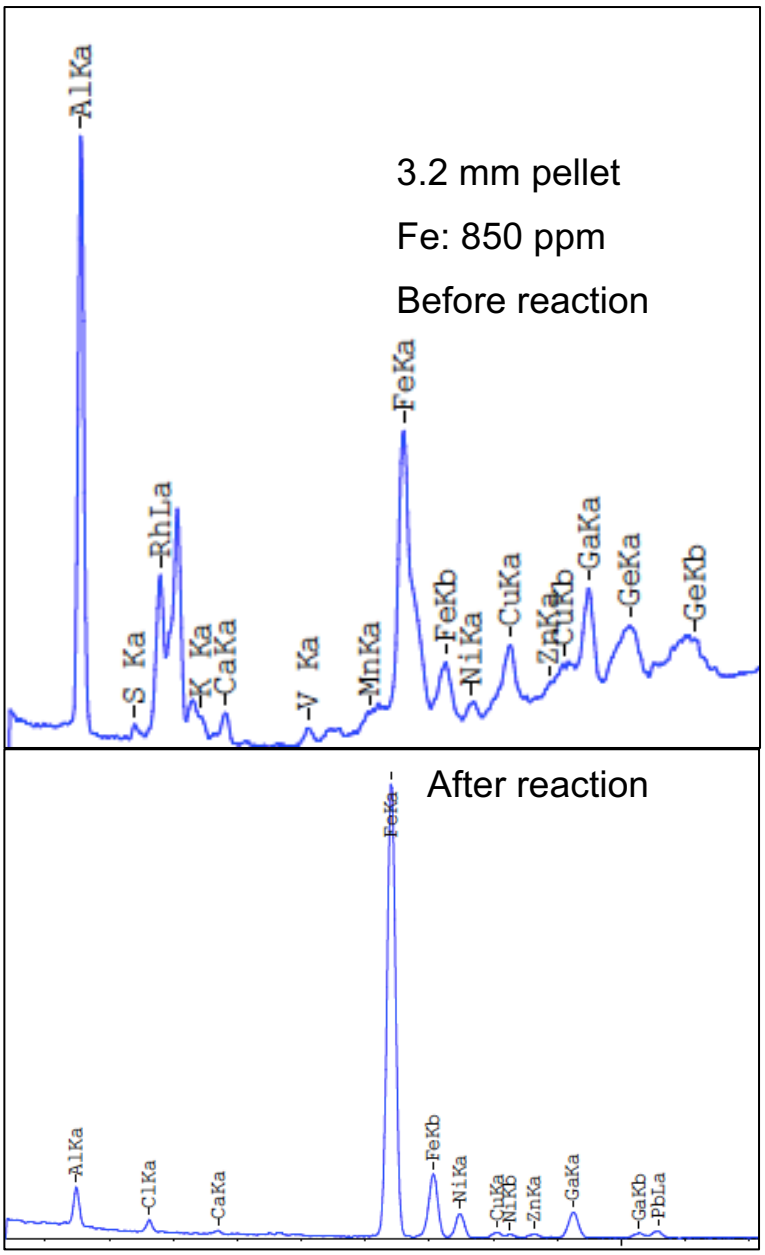

Figure 3-11: EDX spectra of the Al pellet collected before and after the ACH synthesis in the case of type II Al pellet (3.2 mm, 99.824% Al) used in this experiment.

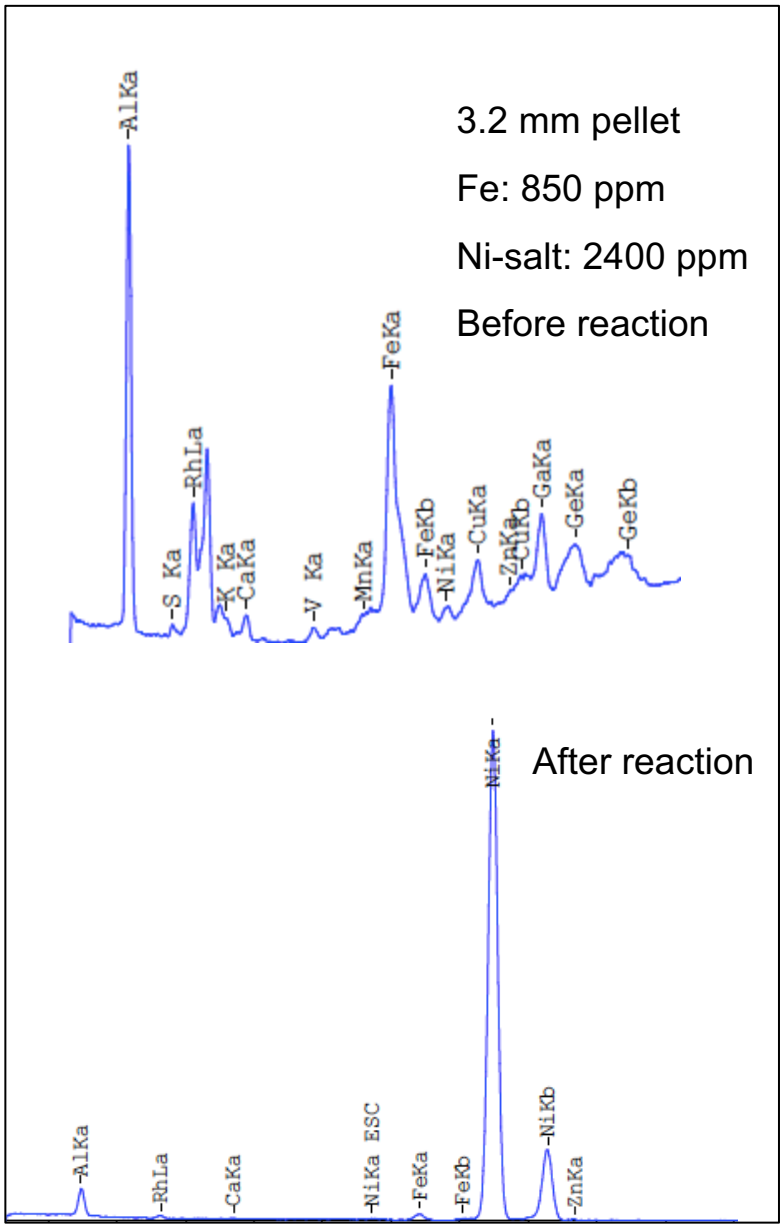

Figure 3-12: EDX spectra of the Al pellet collected before and after the ACH synthesis in the case of Ni-catalyzed type II Al pellet (3.2 mm, 99.824% Al) used in this experiment.

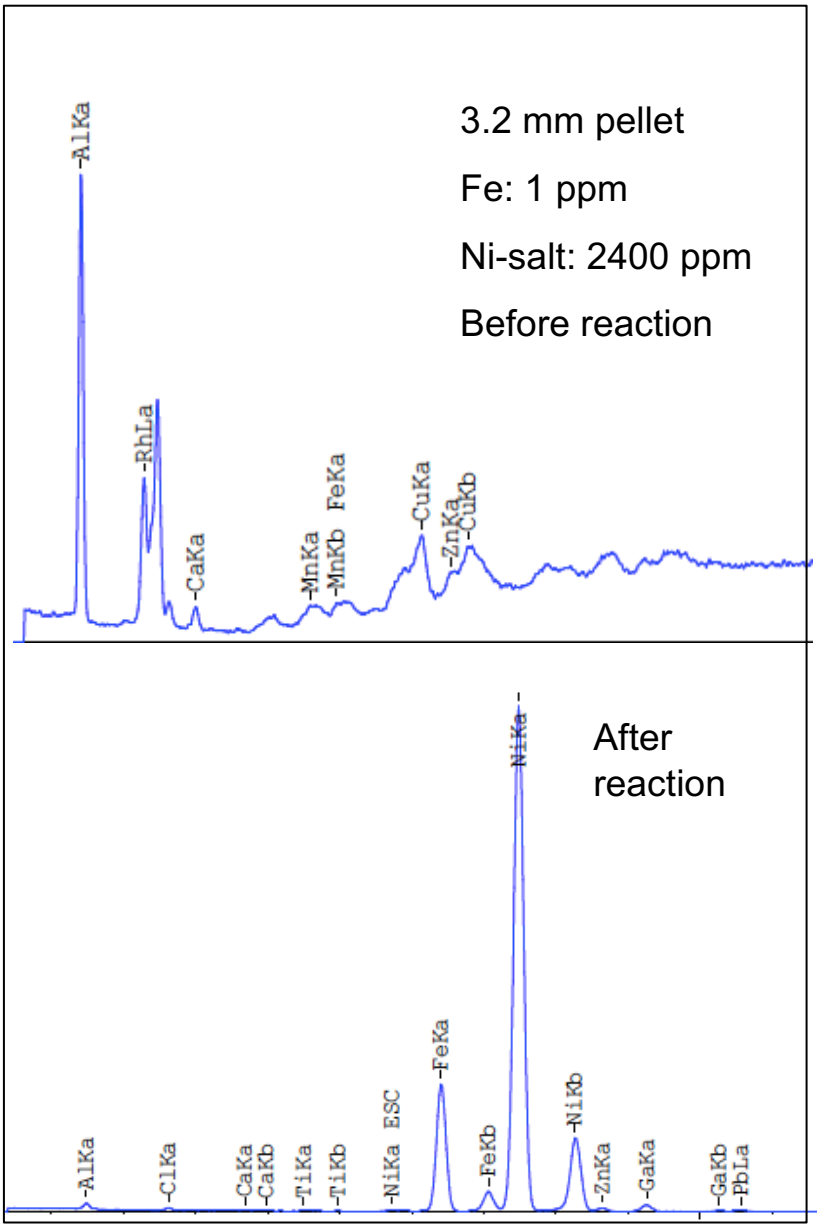

Figure 3-13: EDX spectra of the Al pellet collected before and after the ACH synthesis in the case of Ni- catalyzed type I Al pellet (3.2 mm, 99.999% Al) used in this experiment.

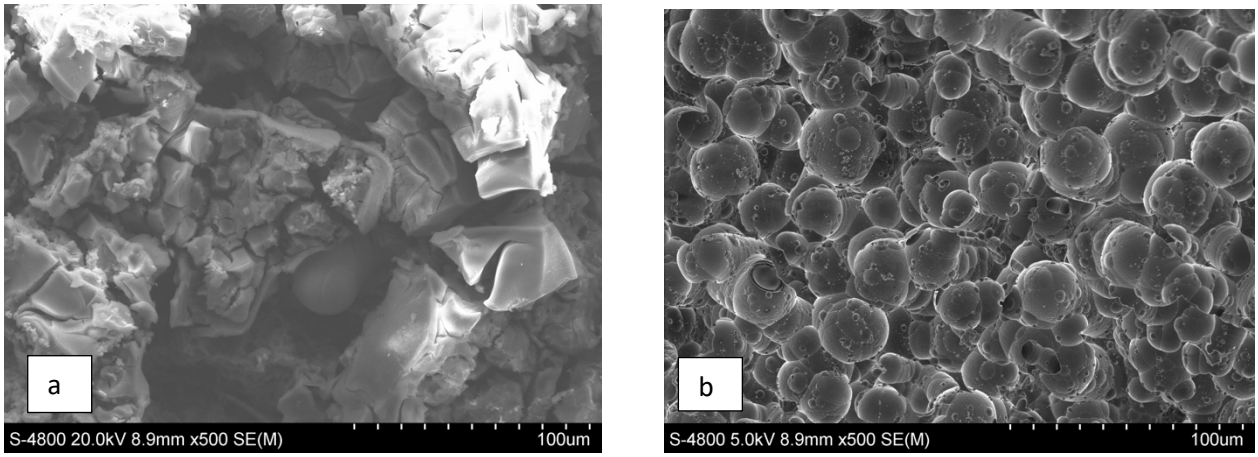

Figure 3-14: SEM image of the Al pellet collected after the ACH synthesis for Ni loading in a. type II pellet (99.824% Al) and b. Type I pellet (99.999% Al).

3.3.7 Kinetic Study

When there are externally added impurities in the ACH solution, the reaction rate increases rapidly. Along with the surface area, the amount and types of impurity affect the reaction rate, and changes in specific gravity with time are plotted in figure 3-15 for the various transition metal impurities added. From this graph, the rate equations for the metal catalyzed ACH reaction are derived.

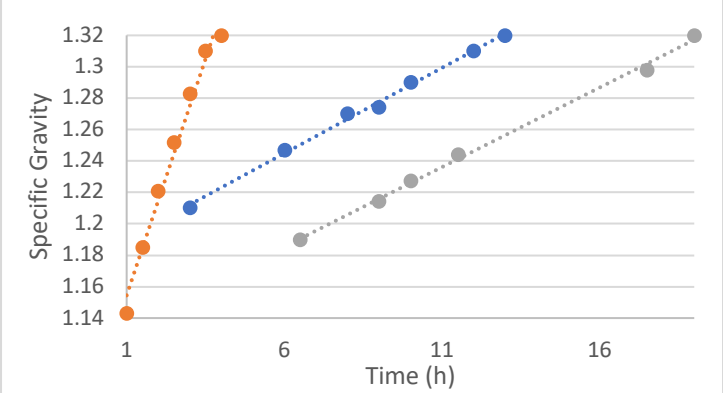

Figure 3-15: Changes of specific gravity with time in ACH synthesis with various transition metal loadings in the solution with 3.2 mm size Al pellet (type II).

The slope of the equation provides the rate of the specific gravity changes with time. The observed rate can be written as:

$K_{obs} = ([Al^{3+}]/t_{sg}-t_0)$ …… (Eqn. 3); where, t_{SG} = time required to reach the specific gravity 1.33, and t_0 = initial time.

The calculated observed rate constant is summarized in table 3-9.

Table 3-9: Calculated rate constant for the ACH synthesis with various metallic impurities added to the system.

Size of Al pellet (mm)	Surface area (cm^2/g)	Fe impurity (ppm)	External impurity	Rate constant, K_{obs} $([Al^{3+}]/t_{sg}-t_0)$
3.2	5.8	850	-	0.24
3.2	5.8	850	Fe	0.5
3.2	5.8	850	Cu	0.3
3.2	5.8	850	Ni	1.5

As seen in table 3-9, the transition metal catalyzed reaction has a higher rate constant than the non-catalyzed reaction. In addition, among the metal catalyzed reactions, Ni has the highest rate constant, followed by Fe and finally Cu, which is five times less than Ni. This is supported by the data from experiment 3.3 in which the Cu reaction took 5 times longer to complete. Therefore, the rate of the ACH synthesis reaction not only depends on the surface area, but also depends on the types of impurities present or added to the metallic aluminum.

3.3 Mechanism of the Transition Metal Catalyzed ACH Synthesis

The reaction rate of ACH is dependent on the surface area of the metallic aluminum. Along with this, small impurities present in the aluminum pellets also significantly affect the reaction rate. Two hypotheses are proposed to explain the effect of impurities on the reaction rate: 1) internal strain due to defects[69,70] and 2) catalyzed H_2 production.

The reaction rate of ACH increases by about 4.5 times when the amount of Fe present in the aluminum pellet increases from 1 ppm to 275 ppm. The purest Al (99.999% pure) used in this chapter has a reaction rate very similar to that of the aluminum ingot, even though the pellets have a larger surface area than the ingot. The data suggest that the presence of Fe impurity in Al makes it more reactive towards the redox reaction through internal strain caused by the Fe defect. Even though the reaction of Al and HCl is an exothermic reaction, because of the formation of Al_2O_3 layer on top of the Al, the reaction initially progresses very slowly. The internal strain cause by the Fe impurity in the Al pellet may make it comparatively unstable and helps to rupture the formed Al_2O_3 layer and increases the reaction rate of the ACH synthesis. In addition, the presence of 3-d transition metals reduces the corrosion resistance of Al, which consequently increases the reaction rate.

The other possible reason for the increased reaction rate is that the present metallic Fe acts as an active catalyst site for H_2 production. In fact, transition metals are widely used as active catalysts in the production of H_2.[1] Among the 3-d series, Ti has the highest H_2 overpotential, which decreases with the increasing atomic number until Ni.[1] Ni has the lowest H_2 overpotential, and after Ni the overpotential starts to increase. These documented changes in overpotential are well matched with the experimental results found in this study. The addition of Ni-salt increases the ACH reaction rate more significantly than the addition of Fe, Co and Cu; especially Cu, which has the least effect on the ACH reaction rate (section 3.2.4). According to the data,

the reactivity of the transition metals in this study is Ni (reaction time: 4 hours) >> Fe, Co (reaction time: 13 hours)> Cu (reaction time: 19 hours).

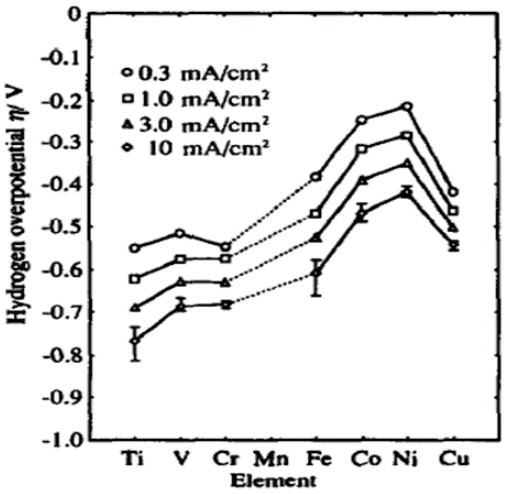

Figure 3-16: Hydrogen overpotential for 3-d transition metals.[2]

In addition, metallic aluminum oxidizes easily to form a layer of aluminum oxide, which prevents further reaction of aluminum; however, water-soluble inorganic salts can produce localized pitting and rupture of the alumina layer on aluminum particles.[71] Such effects have been employed to promote aluminum-water hydrogen production reactions. This effect demonstrated here using the externally added various metallic salt (Fe, Co, Cu and Ni). Among these transition metals, Ni was substantially efficient in the ACH synthesis reaction.

This study proposes a mechanism for how these transition metals affect the rate of H_2 production. The Ni acts as a reactive site for both proton adsorption and electron capture. The adsorbed protons react with the captured electrons to form H atoms, and subsequently to form H_2 and desorb it from the Ni sites (figure 3-17).

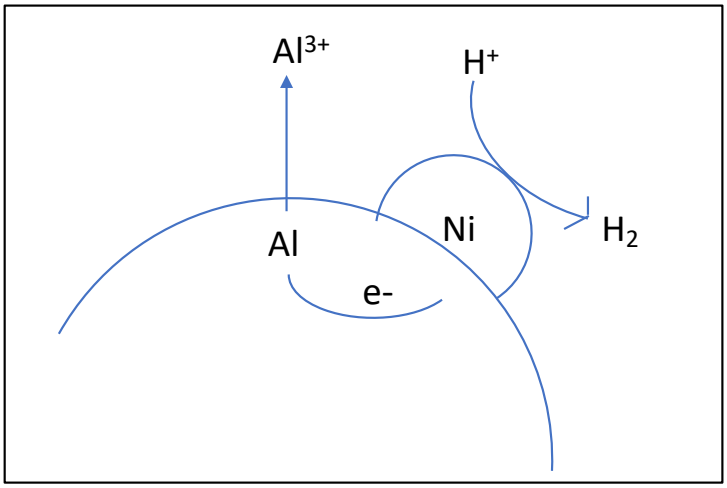

Figure 3-17: H_2 generation using Ni as a co-catalyst on the aluminum surface.

It is important that the adsorption of proton and desorption of H_2 both occur at a reasonable rate to produce H_2 on the catalyst surface. If the catalyst surface has weak bonding strength, the adsorption of H atoms would not be efficient enough to initiate the H_2 generation reaction. Again, if the surface bonding strength is too strong to release the produced H_2, the reaction will be incomplete. Therefore, an optimum balance between adsorption and desorption of H into the catalyst surface is required.

Norskov and co-workers[40] used density functional theory to calculate the hydrogen adsorption free energy of various transition metals, and generated a volcano curve by plotting these calculated free energies versus the experimentally determined hydrogen evolution reaction current density (figure 3-18).

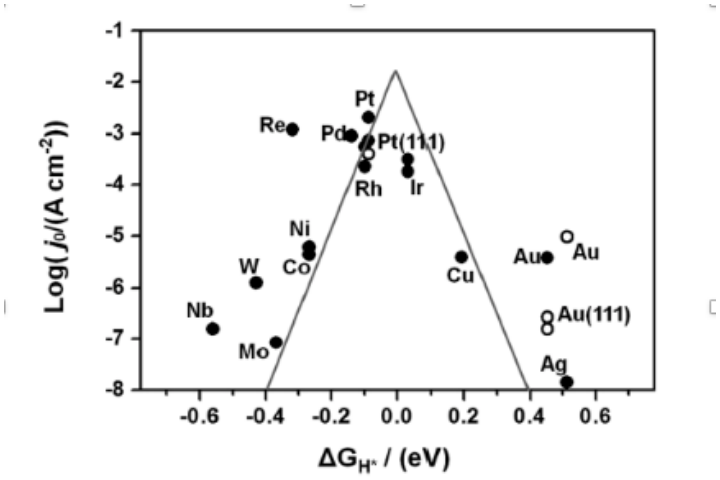

Figure 3-18: Volcano plot of exchange current density as a function of DFT-calculated Gibbs free energy of adsorbed atomic hydrogen on pure metals.[40]

As can be seen in figure 3-18, Pt and other noble metals are situated at the top of the volcano, which means they are excellent hydrogen generation catalysts, followed by the transition metals. These theoretical values match data from previous research.[64] In addition, as seen in figure 3-18, Ni is higher than Co and Cu, meaning that Ni is better at H_2 production. This is also seen in the data from experiments 3.3 in this study.

3.4 Conclusion

The reaction rate of the ACH synthesis can be controlled by the Al surface area when the optimum reaction conditions are strictly followed (150% excess Al, 100 °C, and 20% HCl). However, further investigation of the ACH synthesis reveals that the reaction rate also depends on the purity of the Al metal. The reaction rate decreases with the increasing purity of the Al. In this study, the primary focus is on the Fe impurity present in the Al. Fe destabilizes the Al structure by functioning as an internal strain or acting as a co-catalyst for the H_2 generation reaction and increasing the reaction rate. The results from experiment 3.2 suggest that destabilizing the Al structure with Fe impurity is the reason for the higher reaction rate. However,

when Fe-salt is added to the system, the reaction rate also significantly increases, indicating that both hypothesis 1 and 2 are valid in explaining the increased reaction rate of ACH synthesis.

In addition, data from experiments 3.3 show that replacing Fe-salt with other transition metals affects the reaction rate of ACH synthesis, depending on the metal added and their H_2 overpotential value. With all of the other reaction parameters (surface area, acid concentration, excess Al and the temperature) the same, among the 3-d transition metals used in this study, Ni has the lowest H_2 overpotential, and it increases the reaction rate by 5.5 times compared to the uncatalyzed reaction. Thus, it can be concluded that the reaction rate of ACH synthesis can be controlled by the purity and the surface area of the Al, and by the addition of transition metals.

Chapter 4

Speciation of Al during the Formation of ACH Using Electrospray Ionization-Ion Trap- Time of Flight-Mass Spectrometry (ESI-IT-TOF-MS)

4.1 Introduction

Water treatment and antiperspirants are the two major applications of ACH. ACH is a complex mixture of polymeric water-soluble Al complexes at a pH between 3.5 and 4.0.[2,17] As a concentrated solution, ACH is an effective coagulant and flocculant which induces the coagulation of many colloidal impurities in raw water and crosslinks to form a polymeric gel which precipitates out of solution.[18,23] During this process, not only are many bacterial, viruses, proteins and other biological debris removed, but also it induces the co-precipitation of many heavy metal ions, including Pb^{2+}, to considerably purify the water.[5] These ions are proposed to get caught up in the giant polymeric web that's forms during the flocculation process.

As an antiperspirant, the ACH solution is converted into a waxy-like powder or solid by careful dehydration of the ACH solution. When done properly, the ACH powder is easily re-dissolved in water. Application of this powder to the skin, under the arm, results in the formation of a polymeric aluminum oxy, hydroxy, aqua film, which precipitates or captures the oils and proteins in perspiration and blocks the pores in the skin, preventing perspiration.[6,21] Because of the dermatological application, the ACH must have a mild pH and not irritate the skin, nor cause damage to the clothing.[21]

Because there are numerous uses for ACH, several different grades of ACH are sold, such as those listed in Table 4-1.[72] Key considerations in the ACH grade are the Al_2O_3 and chloride content, pH, and turbidity for solutions.

Table 4-1: Industrial specifications of ACH powder and solution

Grade	Water treatment grade (Solution)	Cosmetic grade (Solution)	Water treatment grade (Powder)	Cosmetics grade (Powder)
Solubility	Soluble in water	Soluble in water	Soluble in water	Soluble in water
Al_2O_3	>23%	23-24%	>46%	46-48%
Cl	<9%	7.9-8.4%	<18%	15.8-16.8%
Basicity	75-83%	75-90%	75-83%	75-90%
pH	3.5-4.0	4.0-4.4	3.5-4.0	4.0-4.4
Specific Gravity	1.33-1.35 g/mL	1.33-1.35 g/mL	1.33-1.35 g/mL	1.33-1.35 g/mL

For many applications, ACH is overkill and cheaper solutions of polymeric aluminum chloride (PAC) are used. The chief difference being that PAC has a lower soluble Al_2O_3 content (i.e. 15%), a lower pH, typically near 1.0, and may contain a greater percentage of other impurities, Fe being the most common. PAC may be sufficient for treatment of wastewater, but not acceptable for treatment of potable water, similarly PAC would generally not be suitable nor pass the quality requirements for use in cosmetics or antiperspirants. In this study, we define ACH as either being water-treatment grade or cosmetic grade and the general specifications are shown in Table 4-1. We limit the scope of this work to a study of the speciation of Al observed during the production of ACH and the speciation found in water treatment grade ACH (solution or powder). While this was the limit of our study, the common methods for making these soluble aluminum products means that much of the chemistry seen in ACH synthesis is relevant to PAC and other grades of ACH.

Polymeric water-soluble aluminum (III) species are common to all PAC and ACH products. In ACH, clusters of 13 Al^{3+} ions bridged by H_2O, OH^-, and O^{2-} ions are found to be the dominant polymeric species in solution or solid.[13,14] The Al_{13} clusters are all generally related to the cluster cation $(Al_{13}O_4(OH)_{24}(H_2O)_{12})^{7+}$ which has the Keggin structure with a central tetrahedral Al ion in the center of a symmetrical, near spherical cluster of 12 octahedrally coordinated Al ions.[16,73,74] The formula can be expressed as $(AlO_4Al_{12}(OH)_{24}(H_2O)_{12})^{7+}$ and can exist in many different protonation states.[74,75] The clusters with this structure are generally referred to as Al_{13} ions. Because of their large size and overall high charge, Al_{13} ions are highly effective in the coagulation process as they can efficiently bind, neutralize, and many of the negatively-charged colloid species present in raw water.[76,77,78]

The formation process for Al_{13} ions is not fully understood, but undoubtedly begins as a condensation process of the monomeric species $[Al(H_2O)_6]^{3+}$ which is formed under high acid conditions.[74] As the reaction between the HCl and Al metal proceeds the acid concentration falls and the $[Al(H_2O)_6]^{3+}$ concentration increases, leading to dimerization reactions, such as those shown in Figure 4-1.[74] The dimer then goes through further polymerization to form trimer, tetramer, and higher polymeric species as the pH rises eventually to 3.5 -4.0.

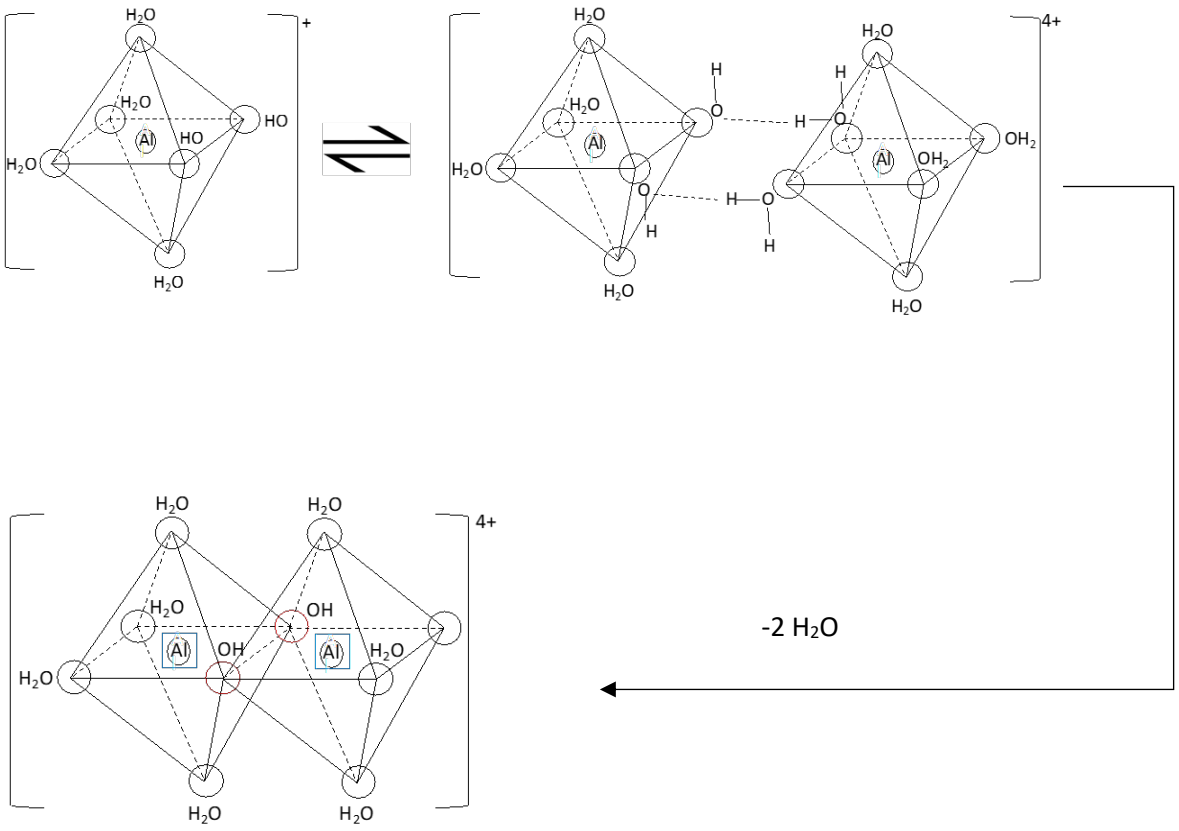

Figure 4-1: Dimerization of Al hydrolysis complex.[74]

During the hydrolysis process, a wide range of polymeric species with Al nuclearities from 1 to 200 are formed, making it difficult to characterize. There are several techniques available for characterizing the ACH polymers. ^{27}Al NMR and X-ray diffraction provides significant information to elucidate the structure of polymeric Al complex.[79] Size exclusion chromatography (SEC) was used to identify the Al polymeric complexes in acidic conditions.[7,80] Even though SEC identified several Al polymeric species, the working pH (pH ~ 1-2) was far from the real pH of the ACH solution (pH ~ 4-5). Capillary electrophoresis (CE) was applied to identify and quantify Al_{13} and Al_{30} complexes in the rea ACH application pH range of ACH (pH ~4.8).[81] The use of electron spray ionization mass spectrometry (ESI-MS) to specify the aluminum hydrolysis species at various pH and concentrations is quite common these days.[82,83,84] Several aluminum

species including the monomer, dimer, trimer, and polymeric species have been identified from these studies and matched with the relevant ^{27}Al NMR data available, demonstrating that ESI-MS can be a reliable instrument for speciation of Al hydrolysis species.[85,86,87,88]

ESI-MS is a soft ionization method used for transporting the pre-existing ions from a solution to the gas phase and then analyzing these ions with mass spectrometry techniques. Counterions in ACH, such as Cl^- anion can coordinate with the Al and help to identify the species using the ESI-MS. However, the coordination of Al with Cl^- is very weak; therefore, it is very complex to separate and identify all of the species from a mass spectrum of ACH solution.[89] Some strong ligands such as EDTA could be used to identify, but they rapidly convert all of the aluminum species into a stable complex and make it impossible to get the kinetic data.[90,91,92]

Speciation of aluminum hydrolysis using electrospray ionization mass spectrometry was comprehensively studied by Sarpola et al.[82,83,87] They investigated aluminum chloride hexahydrate ($AlCl_3{\cdot}6H_2O$) and aluminum sulfate octadecahydrate [$Al_2(SO_4)_3{\cdot}18H_2O$] using the ESI-MS at varying pH ranges and concentrations of aluminum solution. By using the ESI-TOF-MS, they found that the speciation of Al varies with the pH variation: dimeric and trimeric Al species were dominant at pH 3, whereas larger polymers like Al_{13} were dominant at pH 5. In fact, the largest polymer reported was the Al_{30} cluster $[Al_{30}O_{35}(OH)_{17}]^{3+}$ at pH 5. They also studied the $AlCl_3{\cdot}6H_2O$ hydrolysis species using a triple quadrupole tandem mass spectrometry technique. With this technique, no anionic spectra were observed, and the signals of the monomeric species were dominant all over the spectra. At higher collisional energies, a bridging oxo-ligand formed between two hydroxo groups with the loss of a water molecule. They observed that even the smaller dimeric and trimeric complexes were able to capture aqua ligands.

Urabe et al. also studied the hydrolysis of $AlCl_3 \cdot 6H_2O$ in solution using ESI-Q-MS (electrospray ionization-quadrupole-mass spectrometry) and ESI-TOF-MS (electrospray ionization-time of flight-mass spectrometry).[86,89] They observed the formation of mostly positively charged monomeric complexes when there was no pH adjustment of the Al solution. They also found some singly charged polymers (Al_2, Al_3, Al_4 and Al_5) in the solution. However, they found Al_{13}^{3+} (m/z = 279-309) and Al_{13}^{2+} (m/z = 409 + 9n, n = 0-7) in the partially neutralized $AlCl_3$ solution.

Among the several polymeric species of Al hydrolysis studied, Al_{13} is widely noted as the key ingredient for the coagulation of colloidal particles in water treatment industries.[80] Several ESI-MS studies were performed on purified Al_{13} to identify and elucidate the structure of the Al_{13} complex.[16,74] Al_{13} is usually synthesized from $AlCl_3 \cdot 6H_2O$ through base (NaOH) treatment and is then purified prior to ESI-MS analysis. Simple Al salts such as aluminum chloride or aluminum sulfate form similar types of polymeric hydrolysis species as ACH does. However, one of the major advantages of ACH over alum or chloride salt is that ACH does not require a pH adjustment to form the larger multi charged polymeric species, which make ACH more useful in water treatment.[23]

Nearly all of the mass spectrometry-based studies of Al hydrolysis and Al_{13} formation start with aluminum chloride or aluminum sulfate and then add base to adjust the pH. Some studies start with the isolated Al_{13} salt.[74,78] As ACH is made from the reaction of aluminum metal and HCl (aq), the speciation during this reaction is still unexplored. Moreover, to our knowledge there are no reports of the differences in Al speciation in ACH solution (SG 1.33) and solid ACH powder. Herein, Electrospray Ionization-Ion Trap-Time of Flight- Mass Spectrometry (ESI-IT-

TOF-MS) is used to examine the speciation of Al clusters during the synthesis of ACH and in the ACH solution and solid phase products.

4.2 Experimental

4.2.1 Sample Preparation

4.2.1.1 Synthesis of ACH

Water (435 mL) and 200 g Al pellets (3.2 mm, surface area 9.5 cm^2/g) were added to a large 5.0 L round bottomed flask. Upon addition of 500 mL of 20% HCl (6.8 M), the reaction was observed to begin with the release of gas bubbles. Over time, the rate of H_2 evolution increased as the reaction warmed up and became more vigorous. The temperature was observed to rise slowly and then quickly, reaching a maximum of 96 ^oC, which then levelled off and began to cool. Once this exothermic phase had past, another 115 mL of 20% HCl was added and the reaction flask was transferred into preheated oil bath (100 ^oC) to maintain the boiling temperature. Once the specific gravity of the solution reached 1.33, the flask removed from the oil bath and cool down to the room temperature. Measurement of the dried Al bones revealed that 56% of Al charge had dissolved. Reaction time was 21 h. Final volume of the ACH was 740.0 mL. Specific gravity of the solution recorded as 1.34 and turbidity 26 NTU.

4.2.1.2 Sample Preparation for ESI-MS Study:

During ACH synthesis, aliquots (5.0 mL) were collected at 4, 8, 12, and 21 hours. Each sample was diluted with Millipore water (2.5% v/v) and the pH of the samples was measured in the range of 4.2-5. The solutions were then divided into two parts. One part is used for the analysis right after dilution (fresh solution) and another part kept for 7 days (aged solution) before analysis.

In order to prepare the powder ACH samples, the collected aliquot dehydrated in an oven at 90 °C for 3 hours. After drying, the aliquots formed a white solid crystal, which was then crushed to form a water-soluble white powder. Samples for ESI-MS analysis was prepared by dissolving 0.1 g of this Al powder into 4.0 mL Millipore water (2.5% w/v). The salt readily dissolved into the water and the pH of the solutions was between 3.8 and 4.2. These samples also divided into two parts: fresh and aged (7 days) samples.

To investigate the Al hydrolysis complex formation in a Ni-catalyzed ACH synthesis compared to an uncatalyzed one, the samples were prepared following the same procedure described above. $NiSO_4 \cdot 6H_2O$ (800 ppm) was added to the reaction (3.2 mm Al pellets and 20% HCl mixture) at the beginning, and it took about 4 hours to achieve the specific gravity 1.33. During synthesis, aliquots (5.0 mL) were collected at 1 h and 2 h. Collected samples then dried into powder and samples for ESI-MS was prepared by mixing them with water (2.5% w/v).

4.2.2 Mass Spectrometry

The mass spectra were recorded with a Shimadzu LC-IT-TOF-MS spectrometer. In order to verify the reliability of the ESI-TOF-MS, phosphomolybdic acid hydrate ($H_3Mo_{12}O_{40}P \cdot xH_2O$) was used as a test sample using the same techniques as Hercules et al.[93,94] $H_3Mo_{12}O_{40}P \cdot xH_2O$ was dissolved in deionized water and left for about 20 hours to equilibrate, and then analyzed using the ESI-MS. The results of this study show that the mass spectra found for the molybdenum core are the same as Hercules et al. reported.[93,94]

For the Al analysis the LC part was not used; instead a pump syringe was used to introduce the sample at a flow rate of 10 μL/min. The capillary voltage was kept at 4.5 kV because a lower voltage than this showed less intense mass spectra. The CDL temperature was 180 °C and heat

block temperature was 150 °C. The ESI-MS spectra were recorded on a positive ion mode and analyzed using Shimadzu lab solutions software.

4.3 Results and Discussion

In order to determine the structure of the Al polymeric species, the mass spectra were analyzed using the following general technique. A general molecular formula of $[Al_xO_y(OH)_zCl_m{\cdot}nH_2O]^{a+}$ was assumed. Aluminum, oxygen, and hydrogen have only one naturally abundant isotope ^{27}Al (100%), ^{18}O (99.76%), and ^{1}H (99.98%), whereas chlorine has two isotopes, 35Cl (75.78%) and ^{37}Cl (24.22%). Thus, the presence of chlorine is easy to detect and can provide additional insight about the structure of the compound. Dominant peaks in the spectra were first fit to a specific Al_x stoichiometry and charge of the Al complex. The gaussian like distributions of peaks around a specific Alx stoichiometry were then fit, in part, by varying the number of waters (n) and charge. For example, when the Al complex adds a water molecule, the m/z peak has a difference of 18 u is observed for a single charged Al complex, 9 u for a double charged complex, and 6 u for a triple charged complex. The mass spectra of Al_{13} cluster with varying water peaks forms a Gaussian curve that was observed for all of the mass spectra acquired in this study.[82,83]

4.3.1 Identification of Al Hydrolysis Complex

The mass spectra of the ACH powder contains wide ranges of peaks and appears noisy. The significant difference between the mass spectra of 4 h and 21 h (final product) is that the 4 h spectra contains mostly single charged complexes whereas the 21 h spectra contains predominantly multi-charged complexes. The mass spectra of the intermediate solution (12 h)

shows almost equal intensities of double and triple charged Al_{13} species, whereas the final product mass spectra shows much intense triple charged than double charged Al_{13} species.

Mass spectra of ACH solution also forms Al_{13}^{3+} complex in 21 h solution, but there are no Al_{13}^{2+} peak found there. The 4 h solution have few Al_2 and Al_3 single charged species along with Al_{13}^{3+} complex, even though the intensity of the peaks at the mass spectra are reasonably low as compared to the 21 h solution. Table 4-2 summarizes all of the identified Al complexes using the ESI-MS of the ACH powder and aqueous solution at various hours of the synthesis for the aged solution.

Table 4-2: Identified species of aluminum hydrolysis using the ESI-MS of aged ACH powder and aqueous solution.

Symbols	Species	m/z	Reaction time (h)	ACH
Al_2	$[Al_2(OH)_5(H_2O)_n]^+$, n=0-3	139	4	Powder, Solution
Al_3	$[Al_3O_2(OH)Cl_3(H_2O)]^+$	235	4	Powder, Solution
Al_3	$[Al_3(OH)_6Cl_2(H_2O)]^+$	253	4	Powder
Al_4	$[Al_4O_3(OH)_3Cl_2(H_2O)]^+$	277	4	Powder
Al_5	$[Al_5O_2(OH)_8Cl_2]^+$	373	21	Powder
Al_5	$[Al_5O_2(OH)_4Cl_4(H_2O)]^+$	375	21	Powder
Al_{13}	$[Al_{13}O_{10}(OH)_{17}(H_2O)_{n]}^{2+}$,n=0-3	400	12, 21	Powder
Al_{13}	$[Al_{13}O_4(OH)_{28}(H_2O)_n]^{3+}$, n=0-7	303	4, 12, 21	Powder, Solution
Al_{14}	$[Al_{14}O_7(OH)_{25}(H_2O)]^{2+}$	457	12, 21	Powder, Solution

4.3.2 Mass Spectrometry Analysis of Fresh Samples (ACH Solution and Powder)

The 4 h samples for both fresh ACH solution and powder shows only a few peaks in the mass spectra. The mass spectra peaks in the lower m/z area and comparably lower intensities indicate mostly single charged small species present in both of these spectra. None of the mass spectra show any Gaussian shape water coordination with the Al complex or chloride ion exchange with OH^-, which make it difficult to clearly identify the peaks in the mass spectra.

In case of final product ACH for both fresh solution and powder, the mass spectra are similar to each other. The 6u differences in between peaks in the mass spectra indicate triple charged large polymeric species present there. However, the identity of these peaks was inconclusive for both fresh samples of ACH solution and powder. Because the formation of polynuclear aluminum species is comparatively slower than the monomeric and dimeric complexes, to ensure the formation of stable Al complexes, the samples were allowed to equilibrate for about 7 days before mass spectra analysis. This aged sample's mass spectra are analyzed and discussed in section 4.3.3.

4.3.3 Mass Spectrometry Analysis of Aged Samples (ACH Solution and Powder)

4.3.3.1 Aged Sample (ACH powder)

The 4 h sample mass spectra (m/z = 100-300 region) shows a series of peaks with 18u differences (figure 4-1). This is mostly because of the loss of water molecules. The Gaussian shape of the spectra also resembles the water hydrolysis spectra. In addition, the peaks with 18u differences can be attributed to the coordination of Cl^- in exchange of OH^-, as the difference between OH^- and Cl^- is also 18u. The ^{37}Cl isotopic peak also confirms the Cl^- incorporation in some cases.

All of the sample solutions (4 h, 12 h, and 21 h) with a mass spectrum in the region m/z = 300 – 400 form Gaussian curves. In this region, the peaks have a m/z difference of 9u or 6u due to the water coordination, and are identified as double and triple charged species, respectively. Those peaks are mostly Al_{13} and Al_{14} species. The major difference between the 4 h and the 21 h mass spectra is that the final product does not show any of the single charged species at the beginning of the spectra (100-300 m/z).

The 4 h and the 21 h mass spectra both have two Gaussian curves with the highest peak intensity at m/z = 340 and m/z = 400, respectively. The m/z = 400 series converges with the m/z = 340 series, making it quite complicated to identify which peaks belong to which series. Therefore, both series are identified as Al_{13} species, although part of the m/z = 400 series can also be attributed to Al_{14} or Al_{15} species.

The 12h solution mass spectra resembles the final product spectra in that there is no di-, tri-, or tetramers present. The 12 h and 21 h sample mass spectra also formed two Gaussian curves with 9u and 6u differences, which are identified as double and triple charged Al complex.

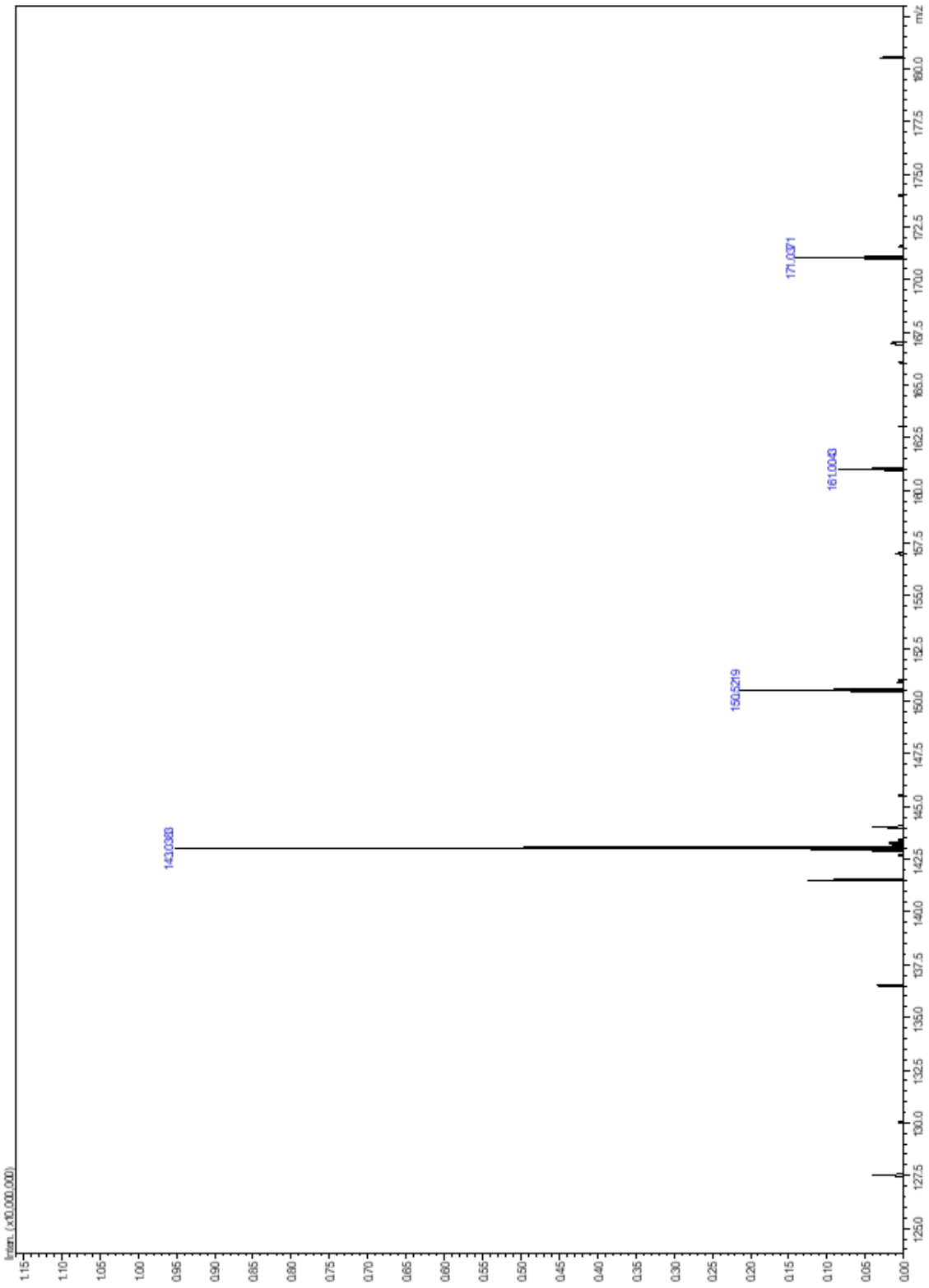

Figure 4-2(a): The ESI-MS spectra generated from the 4 h reaction sample solution (diluted 2.5% v/v Al solution).

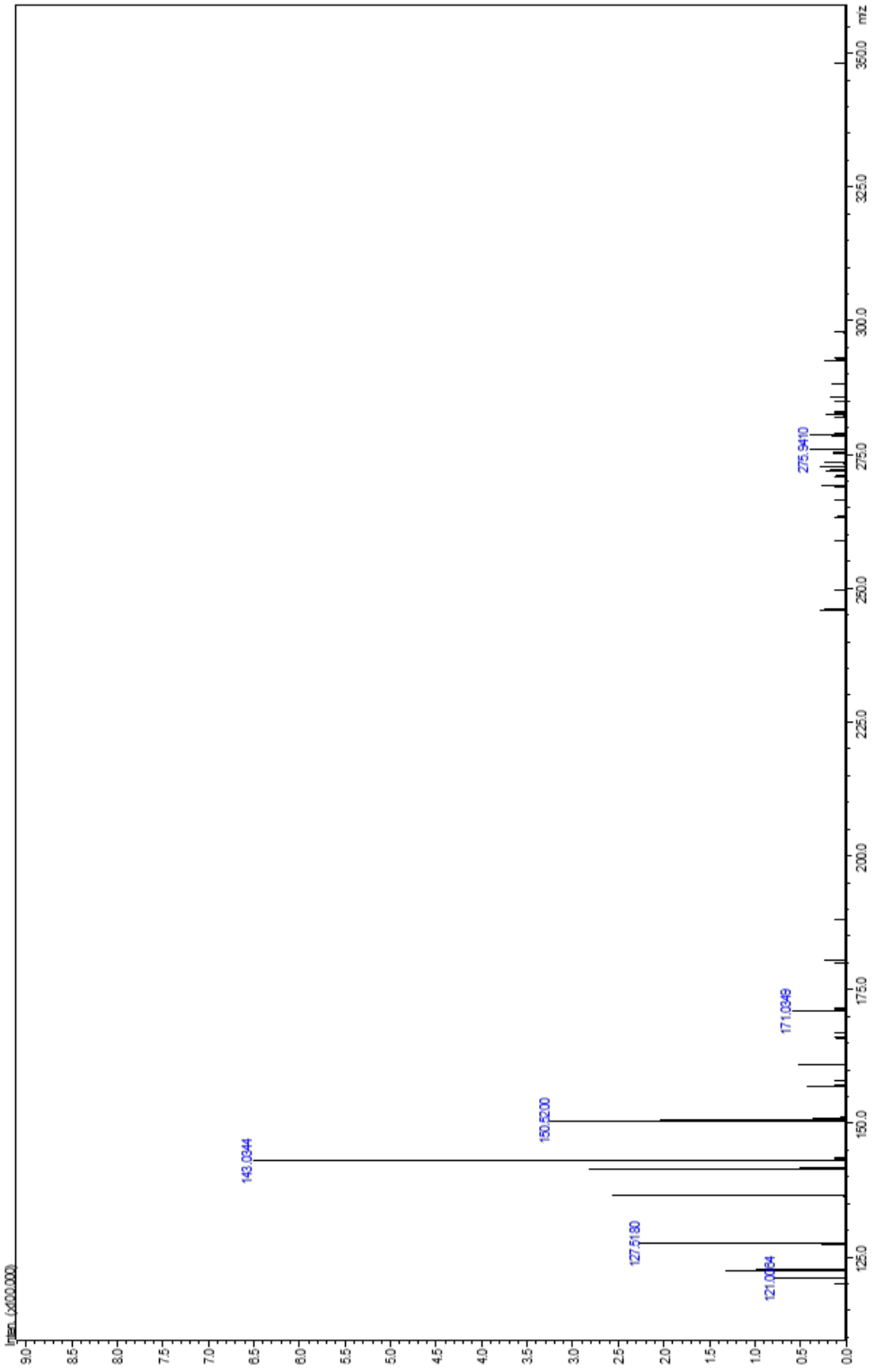

Figure 4-2(b): The ESI-MS spectra generated from the 4 h reaction sample powder (2.5% w/v Al solution).

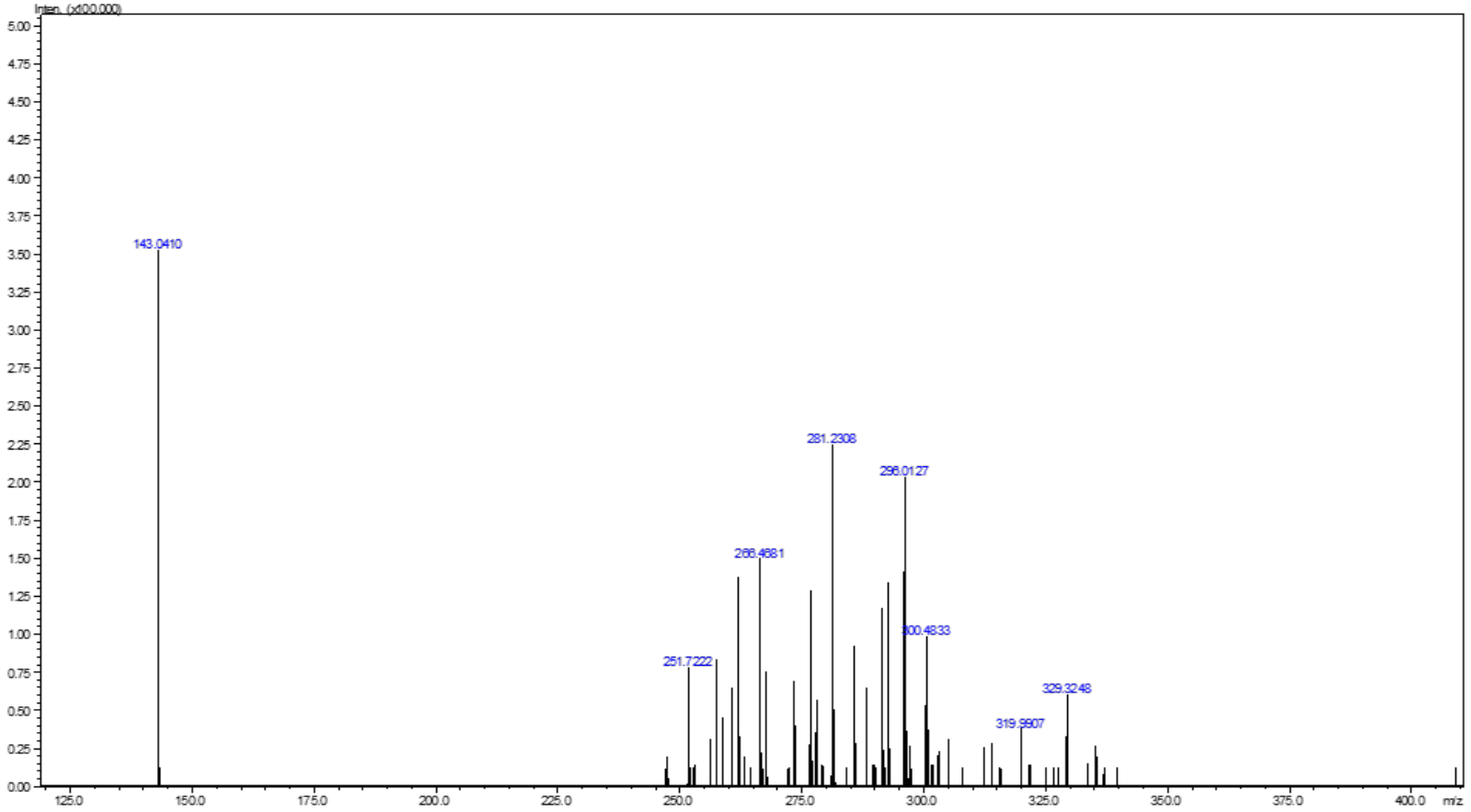

Figure 4-3 (a): The ESI-MS spectra generated from the 21 h reaction sample ACH solution (2.5% v/v solution).

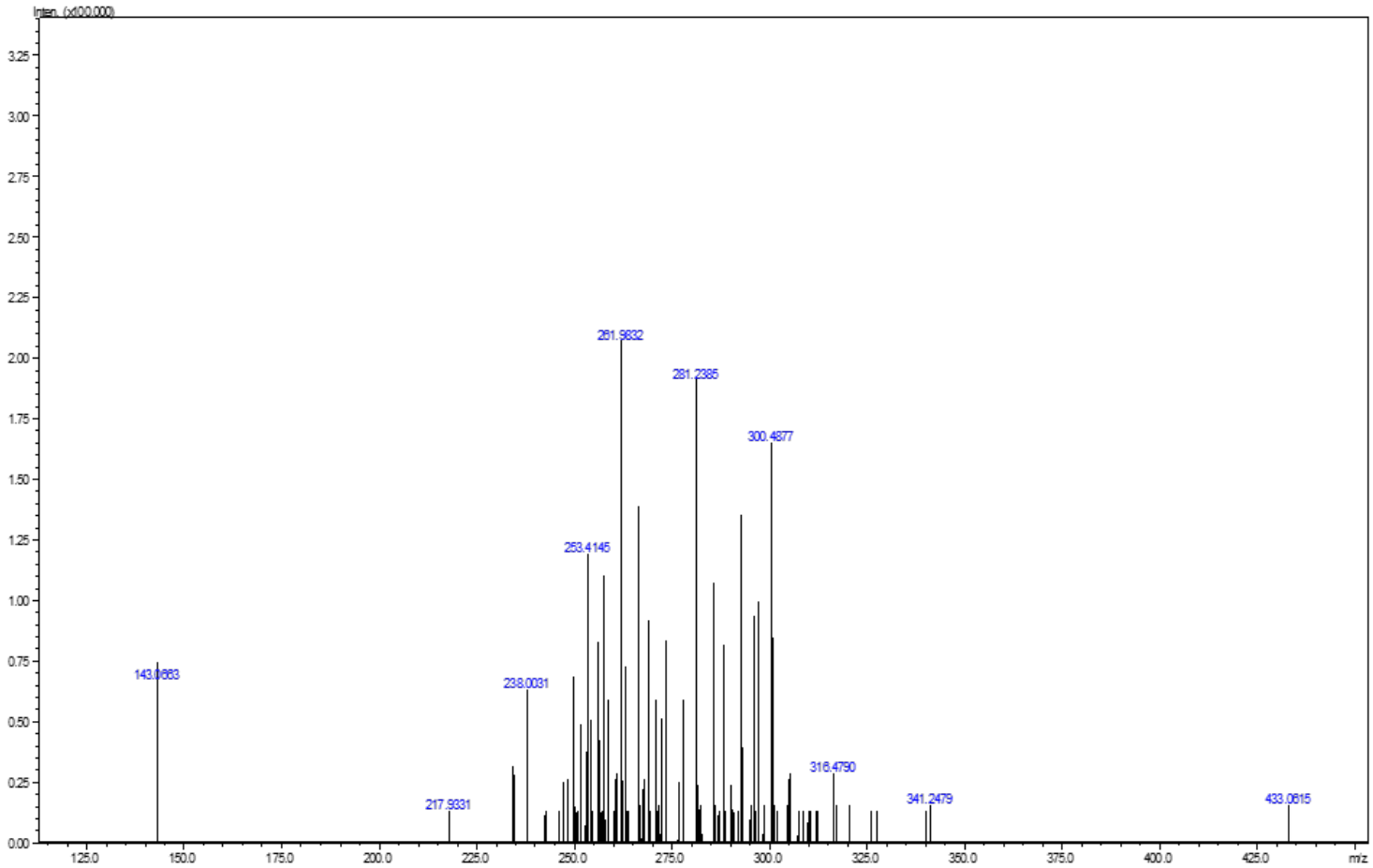

Figure 4-3 (b): The ESI-MS spectra generated from the 21 h reaction sample ACH powder (2.5% w/v solution).

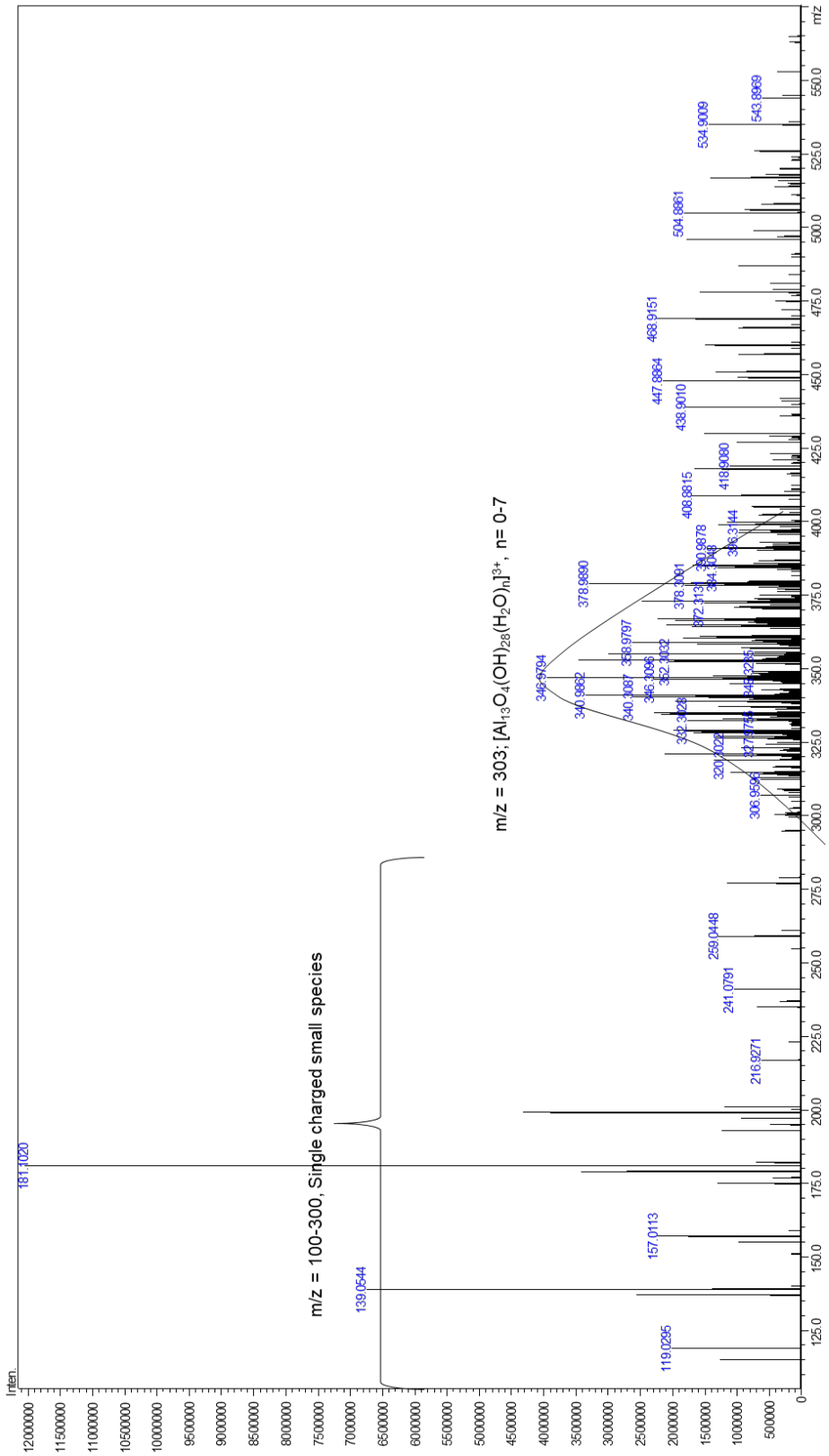

Figure 4-4: The ESI-MS spectra generated from the 4 h reaction aged sample (ACH powder dissolved in water, 2.5% w/v) in m/z = 100-500 region.

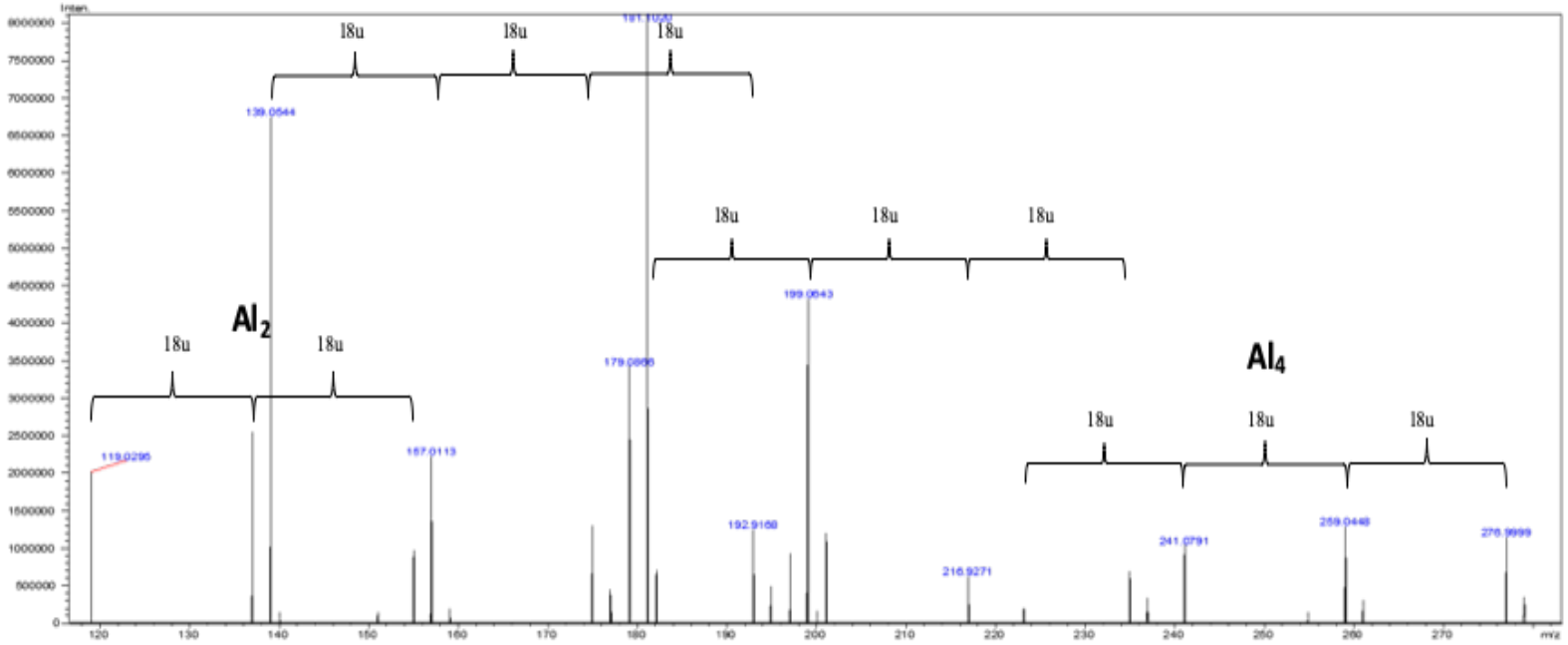

Figure 4-5: The ESI-MS spectra generated from the 4 h reaction aged sample (ACH powder dissolved in water, 2.5% w/v) in m/z = 100-300 region.

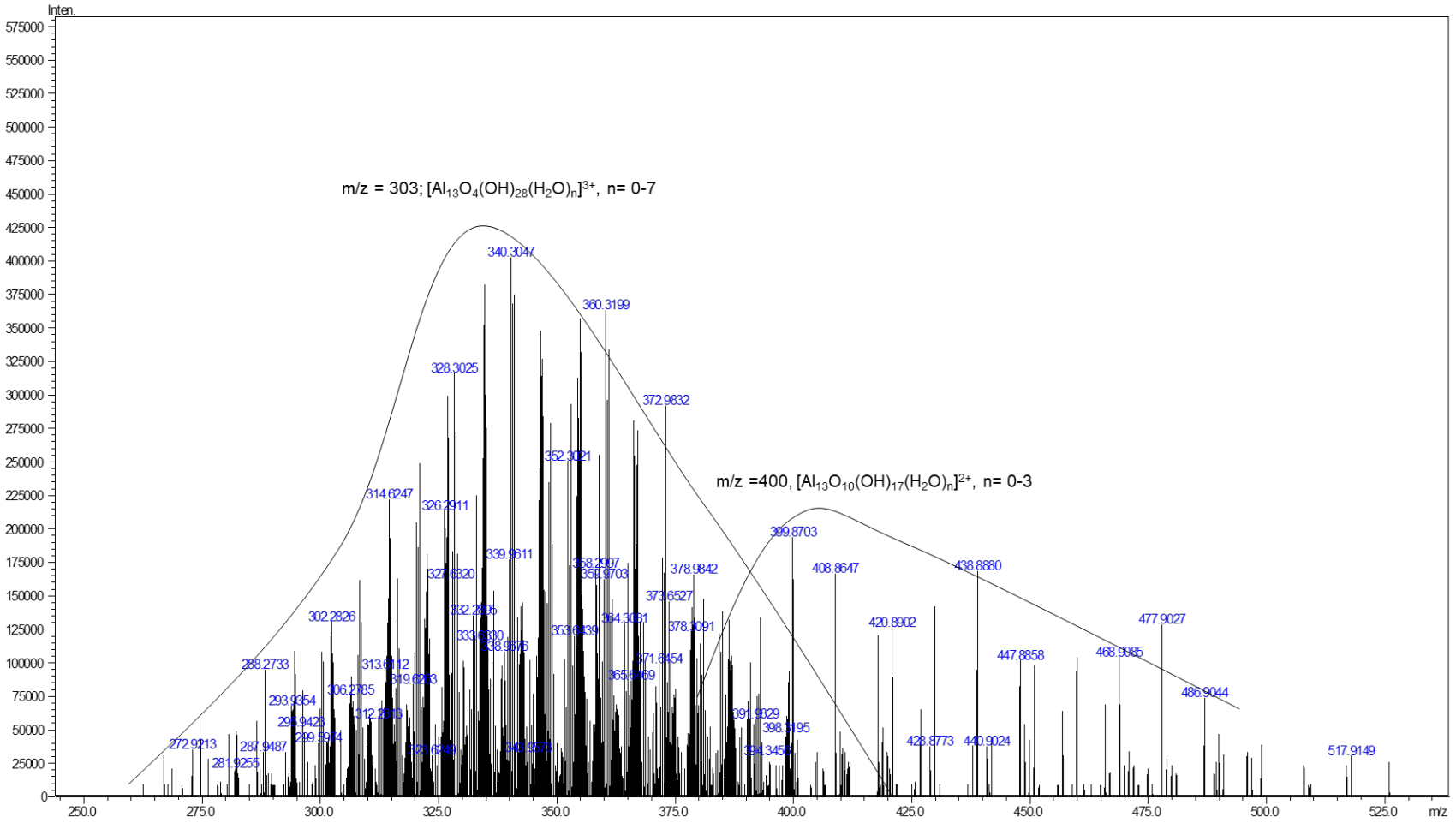

Figure 4-6: The ESI-MS spectra generated from the final product (21 h) reaction aged sample (ACH powder dissolved in water, 2.5% w/v).

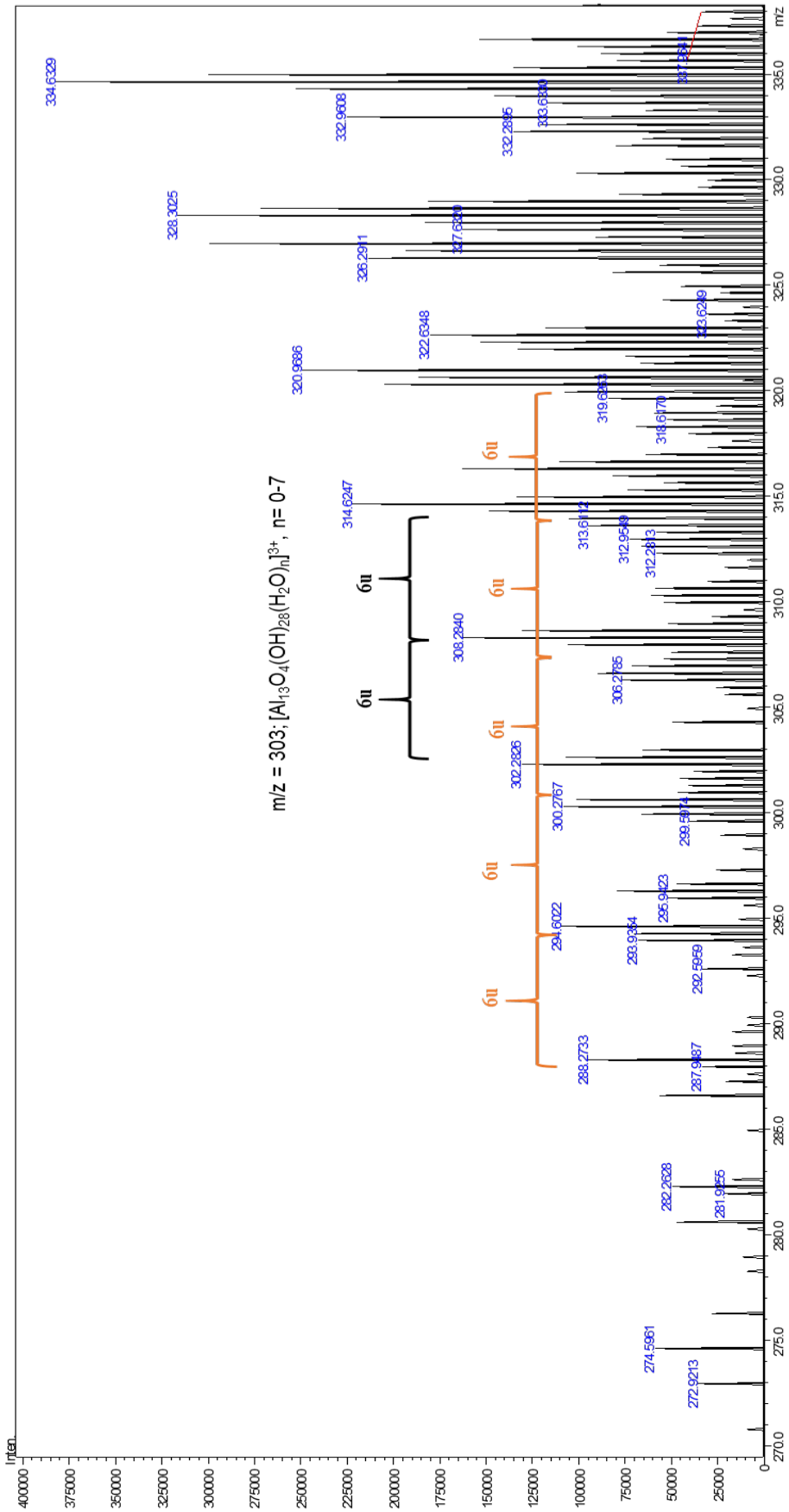

Figure 4-7: The ESI-MS spectra of ACH powder ((dissolved in water, 2.5% w/v) and allowed to equilibrate for 7 days (m/z = 270-335).

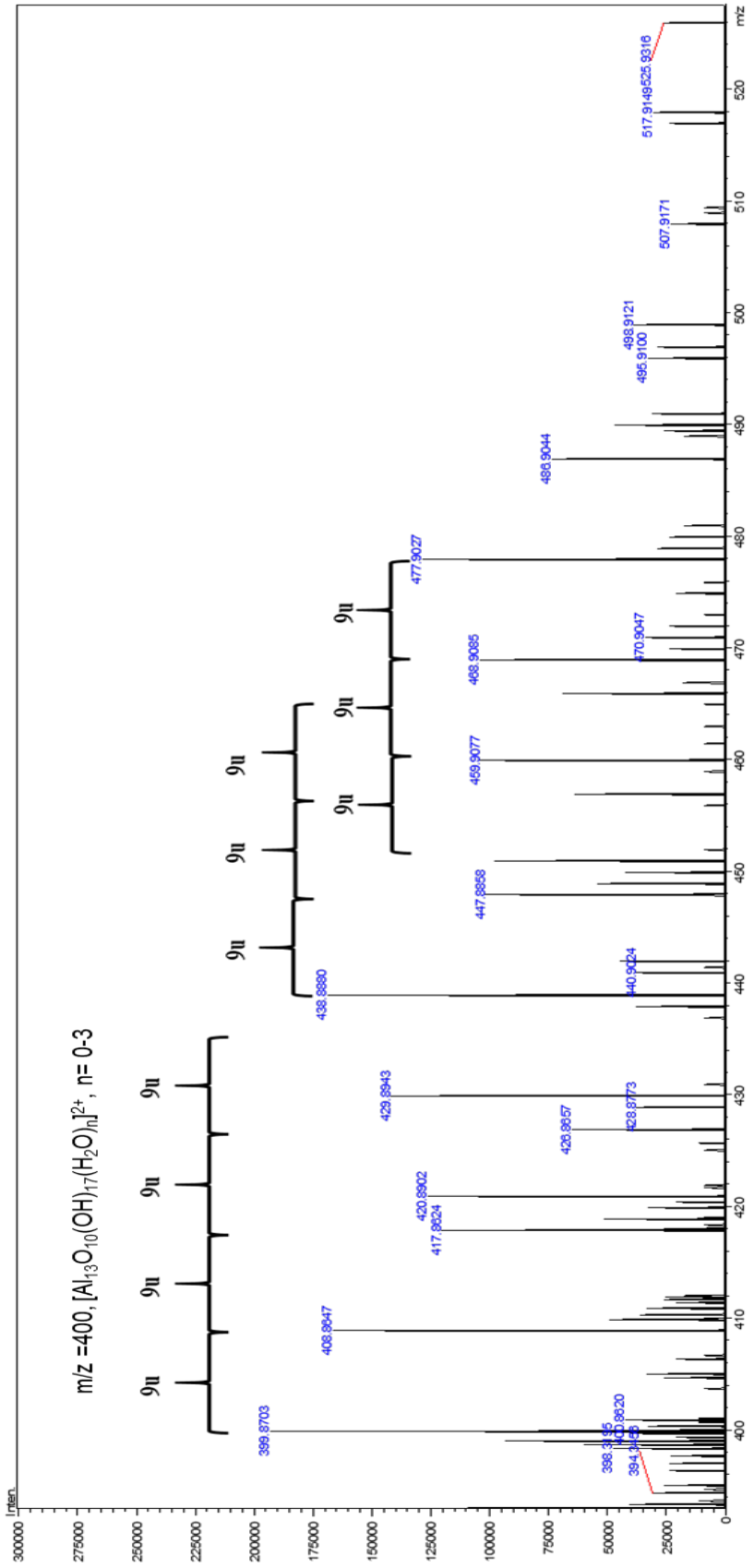

Figure 4-8: The ESI-MS spectra of ACH powder ((dissolved in water, 2.5% w/v) and allowed to equilibrate for 7 days (m/z = 400- 500).

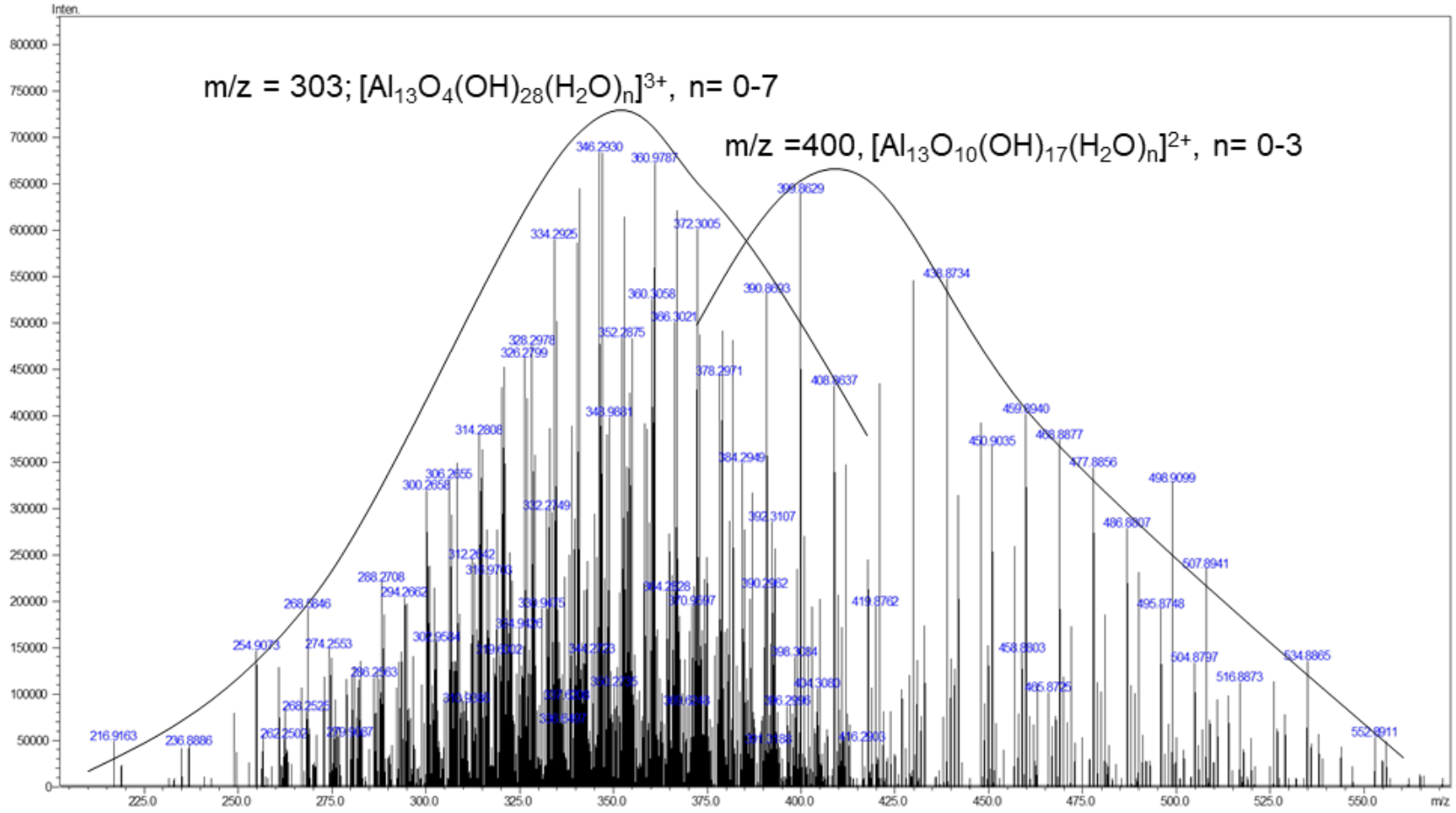

Figure 4-9: The ESI-MS spectra generated from 12 h reaction aged sample (ACH powder dissolved in water, 2.5% w/v).

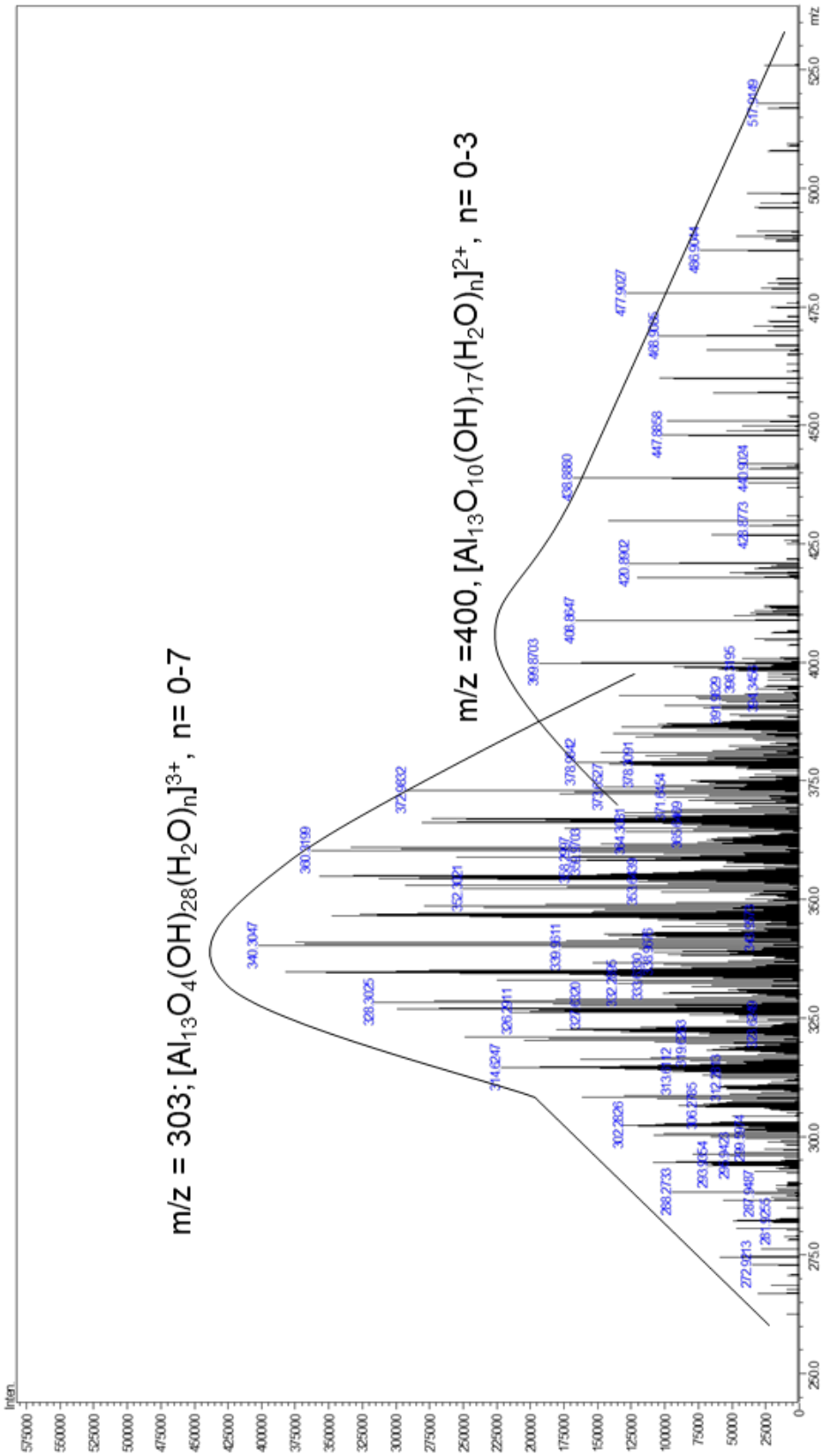

Figure 4-10: The ESI-MS spectra generated from Ni-catalyzed 1 h reaction aged sample (ACH powder dissolved in water, 2.5% w/v).

The mass spectra for the Ni-catalyzed ACH reaction was also analyzed. The first hour mass spectra for the Ni-catalyzed ACH reaction are the same as the mass spectra for the 12 h solution un-catalyzed reaction; in addition, the final product mass spectra for both reactions are the same regardless of the reaction time. Thus, it can be concluded that the reaction with and without 3-d transition metals followed the same path, but with a relatively higher rate of reaction for the transition metals catalyzed reaction.

Lee et al. proposed that the polymerization of the aluminum hydrolysis starts with the monomer formation, which leads to the formation of dimers, trimers and so on. In this study, the data collected for the 4 h solution showed these dimer, trimer, and tetramer species, which leads to the formation of further oligomers.

Furthermore, Lee et al. hypothesized that Al_{13} forms through the polymerization of the pentamer and the octamer species. In this study, the presence of the pentamer species in the 21 h sample solution was identified, but as data was only collected up to m/z = 600, the octamer species was not identified. However, based on their work, it can also be hypothesized that the Al_{13} species found in this study formed through the polymerization of the pentamer species with the octamer species.

4.3.3.2 Aged Sample (ACH solution)

As compared to the ACH powder, the mass spectra of the ACH solution is less intense for all cases of 4, 12, and 21 h solutions. There are some significant differences between the mass spectra of the ACH powder and solution. The 4 h mass spectra for the ACH solution have few single charged species (Al_2 and Al_3), but it does not follow the trend of water enriched Al complex formation as similar as ACH powder. 12 h and 21 h mass spectra are quite similar in ACH

solution, and both of them has highly polymerized Al_{13}^{3+}, Al_{14}^{3+} and Al_{15}^{3+} species present there. There is no single or, double charged species found in the 21 h mass spectra for the ACH solution.

The dehydrated ACH powder contains about 46% Al_2O_3, whereas the ACH solution contains 23% Al_2O_3.[84] Therefore, the ACH powder goes into intensive polymerization during hydrolysis and form Al_{13} enrich salt. However, hydrolysis of ACH solution forms lesser degree of polymerization. Even though ACH solution does undergo polymerization and forms Al_{13} and higher polymeric species, the less intensity of the mass spectra peaks as compared to the ACH powder indicates less amount of polymeric species present in the solution.

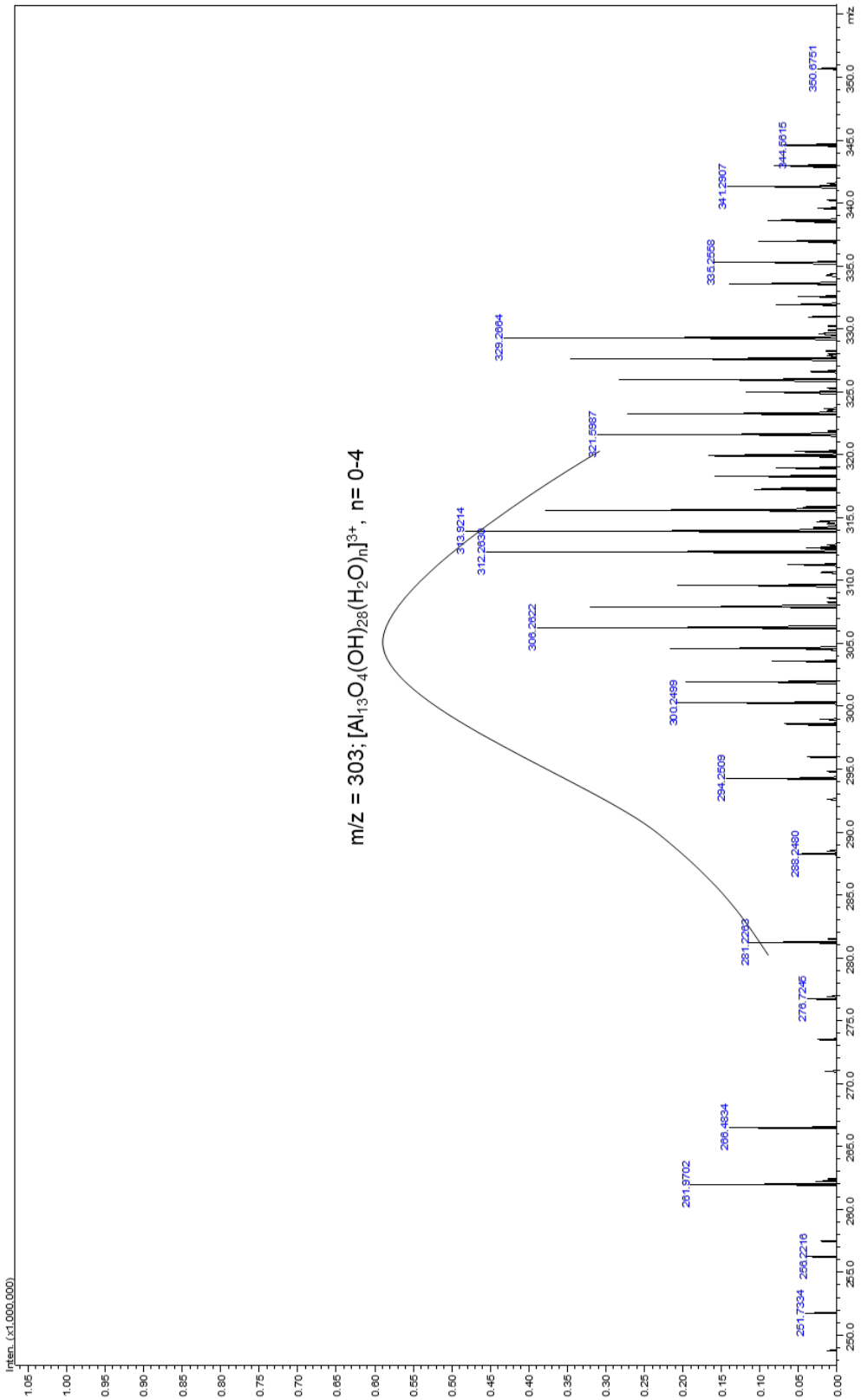

Figure 4-11: The ESI-MS spectra generated from the final product (21 h) reaction aged sample (ACH solution dissolved in water, 2.5% v/v).

4.4 Conclusion

There are numerous studies about the speciation of the polymeric species of Al hydrolysis. All of these studies used different kinds of Al salts, including $AlCl_3$, $Al_2(SO_4)_3$, and isolated Al_{13} enrich salt; however, they all only investigated the final product. In contrast, in this study along with investigating the final product, each step towards the formation of the salt is also analyzed. How the polymerization of the Al hydrolysis occurs during the formation of the salt was thoroughly studied using ESI-MS.

Mass spectra of fresh ACH solution contains mostly smaller single charged species. However, fresh ACH powder contains double charged polymeric species at the 21 h sample solution. For the aged solution, mass spectra of dehydrated ACH powder shows that the solution at the initial stage of the reaction is enriched with stable dimer, trimer, and tetrameric species of Al. As the reaction progressed, these small single charged species started to disappear, and the solution became enriched with Al_{13}^{2+} and Al_{13}^{3+} complexes. When the reaction reached the halfway point (12 h), the Al solution had more intense Al_{13}^{2+} than Al_{13}^{3+} species, with almost no smaller single charged stable di-, tri-, or tetrameric species. As more HCl acid was consumed during the course of the reaction, the proportion of Al_{13}^{3+} to Al_{13}^{2+} increased, and the ACH salt final product (21 h) contained Al_{13}^{3+} species and Al_{14} species, but no Al_{13}^{2+}. In case of ACH solution, the aged solution forms mostly highly polymerized Al complex of Al_{13}, Al_{14} and Al_{15} species in 21 h. But the lesser intensity of the peaks of these complexes indicate a lower degree of polymerization for ACH solution in contrast to ACH powder. Both ACH powder and solution mass spectra show that the polymerization process starts at the early stage of the ACH synthesis and continue to form more stable higher polymeric species. The aged solutions of both ACH powder and solution has almost no stable smaller monomeric or, dimeric species once it equilibrated and enriched

with Al_{13} complex. Published studies suggest that the most important polymeric species of Al hydrolysis is Al_{13}, which plays a critical role in water treatment and the antiperspiration industry. This stepwise Al hydrolysis study confirms this. The data from the ESI-MS of the ACH show that the ACH salt contains concentrated stable polymeric species of the Al_{13} and higher species, which indicates that the activity of the ACH salt depends on the higher polymeric species of Al hydrolysis, including the Al_{13} species.

Chapter 5

Conclusion and Future Work

Aluminum chlorohydrate (ACH) plays a critical role in water treatment, and the antiperspirant and deodorant industry. All of the antiperspirants and deodorants available on the market at present contain aluminum salt, mostly ACH. In the water treatment, ACH is notable for its high solubility, fast processing time, decreased sludge formation, and lowered dosage units. Upon hydrolysis, ACH forms a wide variety of aluminum species ranging from small monomer-dimers to large oligomers like the Al_{13}. These large polymeric species are the key ingredient for the water coagulation and antiperspirant activity of ACH. Numerous studies have attempted to elucidate the structure of ACH and identify the polymeric species of aluminum hydrolysis. Even though the uses of ACH date back to the 1950s, no systematic studies of the ACH synthesis have been published to date. Therefore, this study presents a systematic study of ACH synthesis using metallic Al and HCl.

In addition, there are several industrial ways to prepare ACH, but all of these processes take 3 – 7, and possibly up to 10 days to complete the synthesis. Theoretically, increased surface area should increase the reaction rate. Thus, to increase surface area but maintain product quality, this study replaces industrially used Al ingots with Al pellets during ACH synthesis. Different Al pellet sizes are used to determine the optimum surface area that would maximize reaction rate, and the data show that the reaction rate increases by up to 6.5 times with the pellet with surface area of 5.8 cm^2/g. Further increases in surface area after this size did not have measurable effect on the reaction rate. For example, the grain with surface area 42 cm^2/g also increased the reaction rate 6.5 times. However, when the experiment was initially run, the product quality did not meet the specifications used in the ACH industry. The poor product quality, as determined

by the chloride ion concentration and the Al_2O_3 percentage being out of specification and the turbidity being too high, was a result of the insufficient amount of Al in the reaction system and inefficient circulation of the solution. The ion concentration issue was addressed using 150% excess Al pellets over the stoichiometric quantity. In order to resolve the turbidity problem, two different types of circulation methods (active and passive circulation) were added to the reaction setup.

In the second part of the study, the effect of 3-d transition metal impurities in the ACH synthesis is examined. Trace amounts of Fe present in the Al pellet increases the ACH reaction rate 5 times compared to the pure Al pellet. Furthermore, the ACH reaction rate increased with the addition of 3-d transition metal salts in ppm level. Among the various 3-d transition metal salts, Ni is the most effective and increased the reaction rate by 6.5 times. Based on the experimental data, a kinetic equation involving ACH reaction rate and Al surface area synthesis reaction was developed. This equation shows that the reaction rate of ACH is a function of Al surface area. To explain the effect of 3-d transition metals on the ACH reaction rate, a mechanism is proposed. The ACH reaction is a redox reaction where the metallic Al is reduced to Al^{3+} and H^+ is reduced to H_2 gas. The proposed mechanism is that the added transition metals reduce to their metallic form, are deposited on the Al pellet, and act as the reactive site for the H_2 generation reaction. Thus, the reaction rate increases with increased H_2 generation. The proposed mechanism also explains the increased reaction rate with the Ni-salt, which is in line with other studies that have found that Ni is a very effective co-catalyst for H_2 generation. EDX data from this study shows that the added metallic salt is deposited on the Al pellet during the reaction. Finally, the calculated observed rate constant for the transition metal catalyzed reaction also supports the

proposed mechanism in that when the surface area of the Al remains constant, the reaction rate depends on the types of transition metal added to the system.

Previous research shows that the hydrolysis product of the ACH forms different types of polymer species ranging from monomer to polymer.[81] In this study, ESI-TOF-MS is used to determine the spectra of the ACH hydrolyzed solution and the identity of the species formed during the reaction. The data show that the most significant species is Al_{13}, which starts to form as early as 4 hours into the reaction (total reaction time 21 hours). However, one significant difference between the first quarter of the reaction and the final product is the first quarter has stable single charged species while the final product does not. With increasing time, the amount of polymer species increased.

Klug et al. reported that ACH activity as an active ingredient of antiperspirant increases with decreasing Fe content in it.[28] Total Fe content in ACH measured using the ICP-OES (inductively coupled plasma-optical emission spectroscopy) in this study is in the range of 40-50 ppm. The Fe-catalyzed ACH synthesis has 3 times more Fe in it (about 150 ppm). Using other 3-d transition metals such as Ni, ACH can be synthesized in about 4 hours but the total Ni content in ACH is also 150-160 ppm. Thus, it is important to establish a method to remove the trace metals from the ACH solution to increase its activity. Also, it is critical to optimize the surface area and the quantities of metallic impurities of aluminum to produce the most efficient ACH synthesis process.

Industrially, the typical production time for ACH is 3-5 days with Al ingot due to the lesser surface area and slow digestion of the ingot. With using higher surface area Al pellet, the production time is reduced down to 20-22 hours in this study. By reducing the production time, the total production cost is decreased, and efficiency of the production is increased.

Reference

(1) Eza, H. Hydrogen Overpotential for Transition. **1992**, No. 4.

(2) Fitzgerald, J. J. Chemistry of Basic Commercial Aluminum Hydrolysis Complexes. *Antiperspirants and Deodorants* **1988**, *119*, 292.

(3) Geo Specialty Chemicals. 2013, accessed 1 August 2019, http://www.geosc.com

(4) Ruehl, K. 1999, WaterWorld, accessed 1 August 2019, http://www.waterworld.com

(5) Shelley, W. B.; HURLEY, H. J.; Nichols, A. C. Axillary Odor: Experimental Study of the Role of Bacteria, Apocrine Sweat, and Deodorants. *Ama Arch. Dermatology Syphilol.* **1953**, *68* (4), 430–446.

(6) Dobson, R. L. Toxicology and Pharmacology of Topically-Applied Agents on the Eccrine Sweat Gland. In *Toxicology: Proceedings of the International Congress of Pharmacology, Paris, 1978*; Pergamon, 1979; p 269.

(7) Fitzgerald, J. J.; Rosenberg, A. H. Chemistry of Aluminum Chlorohydrate and Activated Aluminum Chlorohydrates. *Cosmet. Sci. Technol. Ser.* **1999**, 83–136.

(8) Pophristic, V.; Balagurusamy, V. S. K.; Klein, M. L. Structure and Dynamics of the Aluminum Chlorohydrate Polymer Al13O4(OH)24(H2O)12Cl7. *Phys. Chem. Chem. Phys.* **2004**, *6* (5), 919–923.

(9) Brinker, C. J.; Scherer, G. W. *Sol-Gel Science: The Physics and Chemistry of Sol-Gel Processing*; Academic press, 2013.

(10) Teagarden, D. L.; Kozlowski, J. F.; White, J. L.; Hem, S. L. Aluminum Chlorohydrate I: Structure Studies. *J. Pharm. Sci.* **1981**, *70* (7), 758–761.

(11) Teagarden, D. L.; Hem, S. L. Conversion of Aluminum Chlorohydrate Oaluminum Hydroxide. **1982**.

(12) Johansson, G. On the Crystal Structures of Some Basic Aluminum Salts. *Acta Chem. Scand* **1960**, *14* (3), 771–773.

(13) Pophristic, V.; Klein, M. L.; Holerca, M. N. Modeling Small Aluminum Chlorohydrate Polymers. *J. Phys. Chem. A* **2004**, *108* (1), 113–120.

(14) Bottero, J. Y.; Cases, J. M.; Fiessinger, F.; Poirier, J. E. Studies of Hydrolyzed Aluminum Chloride Solutions. 1. Nature of Aluminum Species and Composition of Aqueous Solutions. *J. Phys. Chem.* **1980**, *84* (22), 2933–2939.

(15) Riesgraf, D. A.; May, M. L. Infrared Spectra of Aluminum Hydroxide Chlorides. *Appl. Spectrosc.* **1978**, *32* (4), 362–366.

(16) Casey, W. H.; Phillips, B. L.; Furrer, G. Aqueous Aluminum Polynuclear Complexes and Nanoclusters: A Review. *Rev. Mineral. Geochemistry* **2010**, *44* (1), 167–190.

(17) Gillberg, L.; Hansen, B.; Karlsson, I.; Enkel, A. N.; P□lsson, A.; Kemwater., K. *About Water Treatment.*; Kemira Kemwater: Helsingborg, 2003.

(18) Teh, C. Y.; Budiman, P. M.; Shak, K. P. Y.; Wu, T. Y. Recent Advancement of Coagulation–Flocculation and Its Application in Wastewater Treatment. *Ind. Eng. Chem. Res.* **2016**, *55* (16), 4363–4389.

(19) Kuno, Y. Human Perspiration. Charles C. Thomas, Springfield in the British Commonwealth Blackwell. Oxford: Scientific. Publ 1956.

(20) Killian, J. A.; Panzarella, F. P. Comparative Studies of Samples of Perspiration Collected

from Clean and Unclean Skins of Human Subjects. *Proc. Sci. Sec. Toilet Goods A* **1947**, No. 7, 3.

(21) Cosmet, O. F. *Ifscc Monograph*.

(22) Papa, C. M.; Kligman, A. M. Mechanisms of Eccrine Anidrosis. II. The Antiperspirant Effect of Aluminium Salts. *J. Invest. Dermatol.* **1967**, *49* (2), 139–145.

(23) Tang, H.; Xiao, F.; Wang, D. Speciation, Stability, and Coagulation Mechanisms of Hydroxyl Aluminum Clusters Formed by PACl and Alum: A Critical Review. *Adv. Colloid Interface Sci.* **2015**, *226*, 78–85.

(24) Gomelya, M.; Trus, I.; Shabliy, T. Application of Aluminium Coagulants for the Removal of Sulphate from Mine Water. **2014**.

(25) Verma, A. K.; Bhunia, P.; Dash, R. R. Effectiveness of Aluminum Chlorohydrate (ACH) for Decolorization of Silk Dyebath Effluents. *Ind. Eng. Chem. Res.* **2012**, *51* (25), 8646–8651.

(26) Yonge, D. T.; Duranceau, S. J.; Biscardi, P. G. Comparing Hydrolyzing to Prehydrolyzed Coagulants for Treatment of a Florida Slough. *J. Environ. Eng.* **2015**, *142* (2), 4015059.

(27) Bratby, J. Coagulation and Flocculation in Water and Wastewater Treatment. *Water Intelligence Online*. 2016, pp 9781780407500–9781780407500.

(28) Lin, J. 2017, Pre-Treatment of Coal Seam Water with Coagulation and Electrocoagulation, Unpublished MS Thesis, Queensland University of Technology, Brisbane, Australia.

(29) Chemkimia. 2014, accessed 1 August 2019, http://www.chemkimia.com

(30) US. Patent. No. 2, 196, 016.

(31) US. Patent. No. 3, 873, 686.

(32) US. Patent No. 3, 887, 691.

(33) US. Patent. No. 4, 267, 161.

(34) US. Patent. No. 2, 392, 531.

(35) US. Patent. No. 3, 113, 911.

(36) US. Patent. No. 3, 767, 549.

(37) Chen, Z.; Qin, Y.; Amine, K. Redox Shuttles for Safer Lithium-Ion Batteries. *Electrochim. Acta* **2009**, *54* (24), 5605–5613.

(38) Simon, T.; Bouchonville, N.; Berr, M. J.; Vaneski, A.; Adrović, A.; Volbers, D.; Wyrwich, R.; Döblinger, M.; Susha, A. S.; Rogach, A. L.; et al. Redox Shuttle Mechanism Enhances Photocatalytic H2 Generation on Ni-Decorated CdS Nanorods. *Nat. Mater.* **2014**, *13*, 1013.

(39) Zeng, M.; Li, Y. Recent Advances in Heterogeneous Electrocatalysts for the Hydrogen Evolution Reaction. *J. Mater. Chem. A* **2015**, *3* (29), 14942–14962.

(40) Nørskov, J. K.; Bligaard, T.; Logadottir, A.; Kitchin, J. R.; Chen, J. G.; Pandelov, S.; Stimming, U. Trends in the Exchange Current for Hydrogen Evolution. *J. Electrochem. Soc.* **2005**, *152* (3), J23–J26.

(41) Yang, J.; Wang, D.; Han, H.; Li, C. Roles of Cocatalysts in Photocatalysis and Photoelectrocatalysis. *Acc. Chem. Res.* **2013**, *46* (8), 1900–1909.

(42) Wang, Y.; Wang, Y.; Xu, R. Photochemical Deposition of Pt on CdS for H_2 Evolution

from Water: Markedly Enhanced Activity by Controlling Pt Reduction Environment. *J. Phys. Chem. C* **2013**, *117* (2), 783–790.

(43) Yu, J.; Qi, L.; Jaroniec, M. Hydrogen Production by Photocatalytic Water Splitting over Pt/TiO2 Nanosheets with Exposed (001) Facets. *J. Phys. Chem. C* **2010**, *114* (30), 13118–13125.

(44) Lingampalli, S. R.; Gautam, U. K.; Rao, C. N. R. Highly Efficient Photocatalytic Hydrogen Generation by Solution-Processed ZnO/Pt/CdS, ZnO/Pt/Cd 1− x Zn x S and ZnO/Pt/CdS 1− x Se x Hybrid Nanostructures. *Energy Environ. Sci.* **2013**, *6* (12), 3589–3594.

(45) Yan, H.; Yang, J.; Ma, G.; Wu, G.; Zong, X.; Lei, Z.; Shi, J.; Li, C. Visible-Light-Driven Hydrogen Production with Extremely High Quantum Efficiency on Pt–PdS/CdS Photocatalyst. *J. Catal.* **2009**, *266* (2), 165–168.

(46) Murdoch, M.; Waterhouse, G. I. N.; Nadeem, M. A.; Metson, J. B.; Keane, M. A.; Howe, R. F.; Llorca, J.; Idriss, H. The Effect of Gold Loading and Particle Size on Photocatalytic Hydrogen Production from Ethanol over Au/TiO 2 Nanoparticles. *Nat. Chem.* **2011**, *3* (6), 489.

(47) Sayed, F. N.; Jayakumar, O. D.; Sasikala, R.; Kadam, R. M.; Bharadwaj, S. R.; Kienle, L.; Schürmann, U.; Kaps, S.; Adelung, R.; Mittal, J. P. Photochemical Hydrogen Generation Using Nitrogen-Doped TiO2–Pd Nanoparticles: Facile Synthesis and Effect of Ti3+ Incorporation. *J. Phys. Chem. C* **2012**, *116* (23), 12462–12467.

(48) Onsuratoom, S.; Puangpetch, T.; Chavadej, S. Comparative Investigation of Hydrogen Production over Ag-, Ni-, and Cu-Loaded Mesoporous-Assembled TiO2-ZrO2 Mixed Oxide Nanocrystal Photocatalysts. *Chem. Eng. J.* **2011**, *173* (2), 667–675.

(49) Tsuji, I.; Kato, H.; Kudo, A. Visible-light-induced H2 Evolution from an Aqueous Solution Containing Sulfide and Sulfite over a ZnS–CuInS2–AgInS2 Solid-solution Photocatalyst. *Angew. Chemie Int. Ed.* **2005**, *44* (23), 3565–3568.

(50) Bi, S. -p.; Yang, X.; Zhang, F.; Wang, X.; Zou, G. Analytical Methodologies for Aluminium Speciation in Environmental and Biological Samples - a Review. *Fresenius. J. Anal. Chem.* **2002**, *370* (8), 984–996.

(51) Wang, H.; Chen, W.; Zhang, J.; Huang, C.; Mao, L. Nickel Nanoparticles Modified CdS–a Potential Photocatalyst for Hydrogen Production through Water Splitting under Visible Light Irradiation. *Int. J. Hydrogen Energy* **2015**, *40* (1), 340–345.

(52) Wang, W.; Liu, S.; Nie, L.; Cheng, B.; Yu, J. Enhanced Photocatalytic H 2-Production Activity of TiO 2 Using Ni (NO 3) 2 as an Additive. *Phys. Chem. Chem. Phys.* **2013**, *15* (29), 12033–12039.

(53) Yamada, Y.; Miyahigashi, T.; Kotani, H.; Ohkubo, K.; Fukuzumi, S. Photocatalytic Hydrogen Evolution with Ni Nanoparticles by Using 2-Phenyl-4-(1-Naphthyl) Quinolinium Ion as a Photocatalyst. *Energy Environ. Sci.* **2012**, *5* (3), 6111–6118.

(54) Cao, S.; Wang, C.-J.; Lv, X.-J.; Chen, Y.; Fu, W.-F. A Highly Efficient Photocatalytic H2 Evolution System Using Colloidal CdS Nanorods and Nickel Nanoparticles in Water under Visible Light Irradiation. *Appl. Catal. B Environ.* **2015**, *162*, 381–391.

(55) Tran, P. D.; Xi, L.; Batabyal, S. K.; Wong, L. H.; Barber, J.; Loo, J. S. C. Enhancing the Photocatalytic Efficiency of TiO 2 Nanopowders for H 2 Production by Using Non-Noble Transition Metal Co-Catalysts. *Phys. Chem. Chem. Phys.* **2012**, *14* (33), 11596–11599.

(56) Husin, H.; Su, W.-N.; Chen, H.-M.; Pan, C.-J.; Chang, S.-H.; Rick, J.; Chuang, W.-T.; Sheu, H.-S.; Hwang, B.-J. Photocatalytic Hydrogen Production on Nickel-Loaded La x Na 1− x TaO 3 Prepared by Hydrogen Peroxide-Water Based Process. *Green Chem.* **2011**, *13* (7), 1745–1754.

(57) Dinh, C.-T.; Pham, M.-H.; Kleitz, F.; Do, T.-O. Design of Water-Soluble CdS–Titanate–Nickel Nanocomposites for Photocatalytic Hydrogen Production under Sunlight. *J. Mater. Chem. A* **2013**, *1* (42), 13308–13313.

(58) Chen, X.; Chen, S.; Lin, C.; Jiang, Z.; Shangguan, W. Nickels/CdS Photocatalyst Prepared by Flowerlike Ni/Ni (OH) 2 Precursor for Efficiently Photocatalytic H2 Evolution. *Int. J. Hydrogen Energy* **2015**, *40* (2), 998–1004.

(59) Melián, E. P.; Suárez, M. N.; Jardiel, T.; Rodríguez, J. M. D.; Caballero, A. C.; Araña, J.; Calatayud, D. G.; Díaz, O. G. Influence of Nickel in the Hydrogen Production Activity of TiO2. *Appl. Catal. B Environ.* **2014**, *152*, 192–201.

(60) Chen, S.; Chen, X.; Jiang, Q.; Yuan, J.; Lin, C.; Shangguan, W. Promotion Effect of Nickel Loaded on CdS for Photocatalytic H2 Production in Lactic Acid Solution. *Appl. Surf. Sci.* **2014**, *316*, 590–594.

(61) Laursen, A. B.; Patraju, K. R.; Whitaker, M. J.; Retuerto, M.; Sarkar, T.; Yao, N.; Ramanujachary, K. V; Greenblatt, M.; Dismukes, G. C. Nanocrystalline Ni 5 P 4: A Hydrogen Evolution Electrocatalyst of Exceptional Efficiency in Both Alkaline and Acidic Media. *Energy Environ. Sci.* **2015**, *8* (3), 1027–1034.

(62) Han, J.-W.; Zheng, H.-F.; Cui, Y.; Sun, L.-D.; Ye, D.-Q.; Hu, Z.; Xu, J.-H.; Cai, Z.-M.; Huang, W.; Zhao, G.-P.; et al. Genome-Wide Association Study in a Chinese Han

Population Identifies Nine New Susceptibility Loci for Systemic Lupus Erythematosus. *Nat. Genet.* **2009**, *41*, 1234.

(63) Huang, Z.; Chen, Z.; Chen, Z.; Lv, C.; Meng, H.; Zhang, C. Ni12P5 Nanoparticles as an Efficient Catalyst for Hydrogen Generation via Electrolysis and Photoelectrolysis. *ACS Nano* **2014**, *8* (8), 8121–8129.

(64) Feng, L.; Vrubel, H.; Bensimon, M.; Hu, X. Easily-Prepared Dinickel Phosphide (Ni 2 P) Nanoparticles as an Efficient and Robust Electrocatalyst for Hydrogen Evolution. *Phys. Chem. Chem. Phys.* **2014**, *16* (13), 5917–5921.

(65) Tian, T.; Ai, L.; Jiang, J. Metal–Organic Framework-Derived Nickel Phosphides as Efficient Electrocatalysts toward Sustainable Hydrogen Generation from Water Splitting. *RSC Adv.* **2015**, *5* (14), 10290–10295.

(66) Burchardt, T.; Hansen, V.; Våland, T. Microstructure and Catalytic Activity towards the Hydrogen Evolution Reaction of Electrodeposited NiPx Alloys. *Electrochim. Acta* **2001**, *46* (18), 2761–2766.

(67) McKone, J. R.; Sadtler, B. F.; Werlang, C. A.; Lewis, N. S.; Gray, H. B. Ni–Mo Nanopowders for Efficient Electrochemical Hydrogen Evolution. *ACS Catal.* **2013**, *3* (2), 166–169.

(68) Gong, M.; Zhou, W.; Tsai, M.-C.; Zhou, J.; Guan, M.; Lin, M.-C.; Zhang, B.; Hu, Y.; Wang, D.-Y.; Yang, J. Nanoscale Nickel Oxide/Nickel Heterostructures for Active Hydrogen Evolution Electrocatalysis. *Nat. Commun.* **2014**, *5*, 4695.

(69) Morris, J. W. J. Chapter 4 : Defects in Crystals. *Mater. Sci. Eng. An Introd.* **2013**, 76–

107.

(70) Raghavan, V. Materials Science And Engineering: A First Course; PHI Learning, 2004.

(71) US DOE. Reaction of Aluminum with Water to Produce Hydrogen. *US DOE Rep.* **2008**, 1–26.

(72) Lindsay, S. Aluminum Chlorohydrate. *The Yale Review*. 1997, pp 87–87.

(73) Armstrong, C. R.; Casey, W. H.; Navrotsky, A. Energetics of Al13 Keggin Cluster Compounds. *Proc. Natl. Acad. Sci.* **2011**, *108* (36), 14775–14779.

(74) Lin, Y. F.; Lee, D. J. Electrospray Mass Spectrometry Studies of Purified Aluminum Tridecamer in 50:50 Water/Methanol Mixture. *J. Taiwan Inst. Chem. Eng.* **2011**, *42* (4), 604–607.

(75) Hoffman, D. C. Chemistry of the Heaviest Elements. *Radiochim. Acta* **1996**, *72* (1), 1–6.

(76) Wang, W.-Z.; Hsu, P. H. The Nature of Polynuclear Oh-Al Complexes in Laboratory-Hydrolyzed and Commercial Hydroxyaluminum Solutions. *Clays Clay Miner.* **1994**, *42* (3), 356–368.

(77) Bi, S.; Wang, C.; Cao, Q.; Zhang, C. Studies on the Mechanism of Hydrolysis and Polymerization of Aluminum Salts in Aqueous Solution: Correlations between the “Core-Links” Model and “Cage-like” Keggin-Al13 Model. *Coord. Chem. Rev.* **2004**, *248* (5), 441–455.

(78) Xu, Y.; Wang, D.; Liu, H.; Yiqiang, L.; Tang, H. Optimization of the Separation and Purification of Al13. *Colloids Surfaces A Physicochem. Eng. Asp.* **2003**, *231* (1), 1–9.

(79) Bottero, J. .; Axelos, M.; Tchoubar, D.; Cases, J. .; Fripiat, J. .; Fiessinger, F. Mechanism

of Formation of Aluminum Trihydroxide from Keggin Al13 Polymers. *J. Colloid Interface Sci.* **1987**, *117* (1), 47–57. (80) Phillips, B. L.; Vaughn, J. S.; Smart, S.; Pan, L. Characterization of Al30 in Commercial Poly-Aluminum Chlorohydrate by Solid-State 27Al NMR Spectroscopy. *J. Colloid Interface Sci.* **2016**, *476*, 230–239.

(81) Ouadah, N.; Moire, C.; Kuntz, J. F.; Brothier, F.; Cottet, H. Analysis and Characterization of Aluminum Chlorohydrate Oligocations by Capillary Electrophoresis. *J. Chromatogr. A* **2017**, *1492*, 144–150.

(82) Sarpola, A.; Hietapelto, V.; Jalonen, J.; Jokela, J.; Laitinen, R. S. Identification of the Hydrolysis Products of AlCl3·6H2O by Electrospray Ionization Mass Spectrometry. *J. Mass Spectrom.* **2004**, *39* (4), 423–430.

(83) Sarpola, A. T.; Hietapelto, V. K.; Jalonen, J. E.; Jokela, J.; Rämö, J. H. Comparison of Hydrolysis Products of AlCl3 ·6H2O in Different Concentrations by Electrospray Ionization Time of Flight Mass Spectrometer (ESI TOF MS). *Int. J. Environ. Anal. Chem.* **2006**, *86* (13), 1007–1018.

(84) Urabe, T.; Tanaka, M.; Kumakura, S.; Tsugoshi, T. Study on Chemical Speciation in Aluminum Chloride Solution by ESI-Q-MS. *J. Mass Spectrom.* **2007**, *42* (5), 591–597.

(85) Zhao, H.; Liu, H.; Qu, J. Effect of PH on the Aluminum Salts Hydrolysis during Coagulation Process: Formation and Decomposition of Polymeric Aluminum Species. *J. Colloid Interface Sci.* **2009**, *330* (1), 105–112.

(86) Urabe, T.; Tsugoshi, T.; Tanaka, M. Electrospray Ionization Mass Spectrometry Investigation of the Blocking Effect of Sulfate on the Formation of Aluminum Tridecamer. *J. Mol. Liq.* **2008**, *143* (1), 70–74.

(87) Sarpola, A. T.; Saukkoriipi, J. J.; Hietapelto, V. K.; Jalonen, J. E.; Jokela, J. T.; Joensuu, P. H.; Laasonen, K. E.; Rämö, J. H. Identification of Hydrolysis Products of AlCl3·6H2O in the Presence of Sulfate by Electrospray Ionization Time-of-Flight Mass Spectrometry and Computational Methods. *Phys. Chem. Chem. Phys.* **2007**, *9* (3), 377–388.

(88) Sarpola, A.; Hellman, H.; Hietapelto, V.; Jalonen, J.; Jokela, J.; Rämö, J.; Saukkoriipi, J. Hydrolysis Products of Water Treatment Chemical Aluminium Sulfate Octadecahydrate by Electrospray Ionization Mass Spectrometry. *Polyhedron* **2007**, *26* (12), 2851–2858.

(89) Urabe, T.; Tsugoshi, T.; Tanaka, M. Characterization of Aluminum Species with Nitrate, Perchlorate and Sulfate Ions in the Positive and Negative Ion Mode by Electrospray Ionization Mass Spectrometry. *J. Mass Spectrom.* **2009**, *44* (2), 193–202.

(90) Baron, D.; Hering, J. G. Analysis of Metal-EDTA Complexes by Electrospray Mass Spectrometry. *J. Environ. Qual.* **2010**, *27* (4), 844.

(91) Bertani, R.; Bombi, G. G.; Bortolini, O.; Conte, V.; Di Marco, V. B.; Tapparo, A. Complex Formation between Aluminium (III) and 2-hydroxy Nicotinic Acid: An Electrospray Mass Spectrometric Investigation. *Rapid Commun. mass Spectrom.* **1999**, *13* (18), 1878–1881.

(92) Di Marco, V. B.; Bombi, G. G.; Tubaro, M.; Traldi, P. Electrospray Ionization Mass Spectrometry in Studies of Aluminium(III)–Ligand Solution Equilibria. *Rapid Commun. Mass Spectrom.* **2003**, *17* (18), 2039–2046.

(93) Easterly, C. E.; Hercules, D. M.; Houalla, M. Electrospray-Ionization Time-of-Flight Mass Spectrometry: PH-Dependence of Phosphomolybdate Species. *Appl. Spectrosc.* **2001**, *55* (12), 1671–1675.

(94) Easterly, C. E.; Hercules, D. M.; Houalla, M. Electrospray-Ionization Time-of-Flight Mass Spectrometry: PH-Dependence of Phosphotungstate Species. *Appl. Spectrosc.* **2001**, *55* (12), 1665–1670.

Chapter 6

Solar Photothermochemical Alkane Reverse Combustion

We explored the synthesis of hydrocarbons from CO_2 and H_2O, in a one-step photothermocatalytic process in a flow photoreactor at a higher temperature (200 °C) and pressure (6.1 bar) using a TiO_2 based photocatalyst under UV irradiation. The initial results showed promising efficiencies of the photocatalytic system producing hydrocarbons including liquid alkanes, aromatics and oxygenates. This result was published in PNAS in 2016. While further exploring this system with 99% ^{13}C enriched CO_2, minimal incorporation of the ^{13}C found in the product whereas the published results included a 30% ^{13}C enriched CO_2 with comparable incorporation of ^{13}C in the product system. We assumed that the primary source of the carbon in the hydrocarbon products was the carbon impurities resided into the catalyst. Total carbon content analysis revealed that the total hydrocarbon products have a higher amount of carbon content than the catalyst itself. As the carbon content analysis and the isotopic labeling experiment were contradictory, we spent a great extent of resources and effort in this project to get a conclusive result, but unfortunately, all the data indicated a minimal amount of incorporation of carbon from CO_2 into the product. At this point, we retracted the paper from PNAS and terminated this project. We are archiving this paper here as it might provide helpful information for future studies on the photocatalytic conversion of CO_2 research.

Solar Photothermochemical Alkane Reverse Combustion.

Wilaiwan Chanmanee[1], Mohammad Fakrul Islam[1], Brian H. Dennis,[2]* Frederick M. MacDonnell[1]*

[1]Department of Chemistry and Biochemistry, [2]Department of Mechanical and Aerospace Engineering, University of Texas at Arlington, Arlington TX 76019

Reference: Chanmanee, W.; Islam, M. F.; Dennis, B. H.; MacDonnell, F. M. Solar Photothermochemical Alkane Reverse Combustion. *Proc. Natl. Acad. Sci. U. S. A.* **2016**, *113* (10), 2579–2584.

Abstract:

A one-step, photothermocatalytic process for the synthesis of hydrocarbons, including liquid alkanes, aromatics, and oxygenates, with carbon numbers (C_n) up to C_{13}, from CO_2 and water is demonstrated in a flow photoreactor operating at elevated temperatures (180-200°C) and pressures (1 - 6 bar) using a 5% cobalt on TiO_2 catalyst and under UV irradiation. A parametric study of temperature, pressure, and partial pressure ratio revealed that temperatures in excess of 160° C are needed to obtain the higher C_n products in quantity and that the product distribution shifts towards higher C_n products with increasing pressure. In the best run so far, over 22% by mass of the products were C_5+ hydrocarbons and some of these, i.e. octane, are drop-in replacements for existing liquid hydrocarbons fuels. Dioxygen was detected in yields ranging between 64 to 150 %. In principle, this tandem photochemical-thermochemical process, fitted with a photocatalyst better matched to the solar spectrum, could provide a cheap and direct method to produce liquid hydrocarbons from CO_2 and water via a solar process which utilizes concentrated sunlight for both photochemical excitation to generate high energy intermediates and heat to drive important thermochemical carbon-chain forming reactions.

Keywords: CO_2 reduction, solar fuel, photochemistry, Fischer-Tropsch

Oil is essential for sustaining the current global population and economy because it is the primary source of transportation fuels. Diesel, jet, and gasoline hydrocarbon fuels are unrivalled in terms of energy density and ease of use and storage, however, as fossil fuels their combustion leads to a significant anthropogenic contribution of CO_2 to the atmosphere, estimated at 40 billion metric tons of CO_2 in 2012 alone.[1,2] The eventual replacement of oil with fuels generated from sustainable and carbon-neutral sources is necessary if we are to avoid harmful climate change due to the build-up of greenhouse gases in the atmosphere.[3] Advances in solar-based technologies are the most promising,[4] however these technologies generally produce either electricity or hydrogen, neither of which is an ideal replacement for liquid hydrocarbons. The least disruptive technology would replace oil-derived hydrocarbons with liquid hydrocarbon fuels derived from CO_2, water, and a clean energy source, such as the sun, leading to a carbon-neutral fuel cycle.[5-7]

Currently, there are a number of promising strategies to harness solar energy to generate of high energy molecules (fuels) from water and/or carbon dioxide, including i. high-temperature thermochemical cycles,(8) ii. coupling photovoltaics to water electrolysis (PV-EC),[9, 10] iii. developing single or tandem photoelectrochemical cells (PEC)[11-13], or iv. direct photochemical methods (PC) using semiconductor materials, often modified by added co-catalysts or nanostructuring techniques.[12, 14, 15] Hydrogen, carbon monoxide, C_1 hydrocarbons, and syngas are the most commonly produced fuels and are derived from water or water and CO_2.[6, 16, 17] Hydrogen produced via the water splitting reaction (WSR, reaction 1) is arguably the easiest to produce and stores the most energy on a mass basis (kJ/kg), however it is not a particularly attractive replacement fuel for transportation, due to technological issues with low volume energy density, safe storage, and transportation.[18] Moreover, switching to a hydrogen-based

transportation fuel would also require a considerable investment in upgrading the existing automotive fleet and fuel distribution infrastructure.

One commonly proposed solution to this dilemma is to use the H_2 generated via the WSR, Rxn 1, in combination with CO_2 to synthesize liquid hydrocarbon fuels, using the reverse water-gas shift (RWGS), Rxn 2, and Fischer-Tropsch synthesis (FTS), Rxn 3, reactions.

$$H_2O \rightarrow H_2 + 1/2\ O_2 \qquad \Delta G^o = 237.3\ kJ/mol \qquad WSR\ (1)$$

$$CO_2 + H_2 \rightleftharpoons CO + H_2O \qquad \Delta G^o = 25.2\ kJ/mol \qquad RWGS\ (2)$$

$$(2n + 1)\ H_2 + n\ CO \rightarrow C_nH_{(2n+2)} + n\ H_2O \qquad \Delta G^o \sim -99n\ kJ/mol \qquad FT\ (3)$$

$$(n+1)\ H_2O + n\ CO_2 \rightarrow C_nH_{2n+2} + (3/2n+1/2)\ O_2 \qquad \Delta G^o \sim 665n\ kJ/mol \qquad ARC(4)$$

The combination of reactions 1-3 is the reverse of combustion and, as generally proposed, would be carried out as separate unit operations, each with its attendant efficiency losses and capital and operating costs.[19,20] We report here a photothermochemical process for driving the alkane reverse combustion (ARC) reaction (Rxn 4) to produce C_1 to C_{13} hydrocarbons in a single operation unit. If the process was driven by the sun to provide both photons and heat, a solar photothermochemical alkane reverse combustion (SPARC) process could be achieved in one-step. If the SPARC reaction can be optimized to predominantly produce liquid hydrocarbons and these products are derived from atmospheric CO_2, a sustainable and carbon-neutral liquid fuel cycle could be realized.

The direct production of C_1 hydrocarbons such as methane, methanol, formic acid, and CO from CO_2 and water in a photoelectrochemical reactor was realized as early as the mid 1970s when Halman[21] and then Inoue and coworkers[22] showed that irradiation of TiO_2 coated electrode

suspended in CO_2-saturated aqueous solutions yielded a number of C_1 products. Since this time, research has largely focussed on the exploration and development of new semiconductor photocatalysts,[23] modifications of the semiconductor catalyst in the form of added co-catalysts, e.g. Ni, Cu, Ag, and Pt, [23-25] new methods to nanostructure the catalyst,[26] and the coupling of molecular dyes and co-catalysts with the heterogeneous catalyst. [27,28] While these advances have led to improvements in catalytic efficiency and quantum yields, little progress has been realized in extending the selectivity of the reaction to favor the more desirable, higher carbon number liquid hydrocarbons.[29] While reports of trace amounts of products, such as ethane, ethanol, acetic acid, propanol, and butanol are not unknown,[30-34] they are the exception and frequently the underlying cause for their generation is unknown. Of these reports, the work of Varghese and coworkers stands out.[35,36] They reported that high temperature annealed TiO_2 nanotubes modified with Pt, Pd, or Cu, not only gave methane, but also traces of ethane, propane, butane, pentane, and hexane as well as olefins and branched paraffins, although the details regarding product quantification and characterization were omitted. While this work yielded the highest C_n products yet reported, the results contributed little towards a mechanistic understanding as to how to deliberately target these products.

Thus despite over 40 years of research on the photochemical CO_2 reduction with semiconductors, no clear method for directly producing C_5+ liquid hydrocarbon products exists. Herein, we demonstrate that operation of the photochemical ARC reaction at elevated temperatures in the presence of a hybrid FTS-like photocatalyst (cobalt on TiO_2 support) directly yields C_2+ hydrocarbons as the dominant products, including a significant portion of C_5+ liquid hydrocarbons.

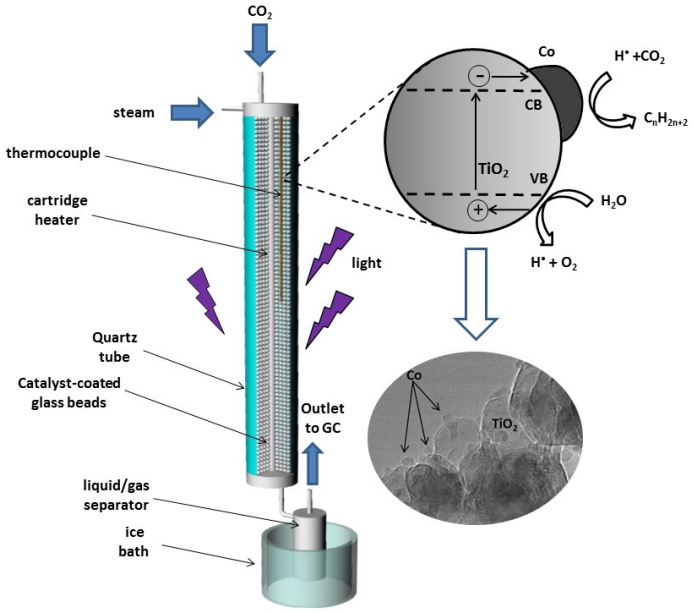

Figure 5-1. Schematic diagram of photothermal flow reactor with cartoon picture of a single Co/TiO_2 particle undergoing catalysis and TEM picture of cobalt on P25 TiO_2 catalyst.

The key insights being that: i. even though the FTS reaction is exothermic, a minimum temperature of ~ 180° C is required in order to obtain reasonable kinetics for the carbon-chain forming process[37,38] and ii. the majority of metals (i.e. Ni, Pd, Pt, Cu) used for CO_2 photocatalytic hydrogenation are poor FTS catalysts as they favor C_1 products.[39] Fe, Co, and Ru are commonly used as FTS catalysts because they exhibit high C_n selectivity,[39] but they have not been commonly explored in the context of CO_2 photoreduction/hydrogenation. By operating the SPARC reaction at elevated temperature and pressure over a hybrid FTS photocatalyst, the products of the photocatalytic reaction can be consumed in thermal reactions which favor higher C_n products.

In order to examine the SPARC reaction as a function of temperature and pressure, we constructed a fixed-bed, tubular flow reactor in which the catalyst bed could be both heated and irradiated, as shown schematically in Fig. 1. During the reaction, CO_2 and steam were flowed at 40 sccm over the 5 % cobalt on TiO_2 catalyst bed, which was heated via an internal electric heater and irradiated with four surrounding 250 W Hg lamps. The products were collected by passing the hot effluent gas through a condenser unit at 0 ^oC to capture condensable products, through a back pressure regulator to drop the pressure to 1.0 bar, and then though a sampling loop of an automated on-line gas chromatograph for real time gas analysis (full details in the SI).

As shown in Fig. 5-2, the condensable (liquid) productivity increases upon increasing the temperature from 110 to 200 °C (1 bar, P_{H2O}/P_{CO2} =1.2, UV irradiation) and the product distribution shifts to C_2 (CH_3CH_2OH and CH_3COOH) and C_3 (propanol) products. Temperatures higher than 200 °C were not explored due to reactor limitations. Below 150 °C, methanol is the exclusive condensable product whereas at 150 °C or above, C_2 and C_3 products become more prevalent and the methanol diminishes. Upon going from 180 to 200 °C, there was doubling of the mass productivity but a drop in propanol production and a large increase in acetic acid formation. Upon lowering the P_{H2O}/P_{CO2} to 0.6 (1 bar, 200 °C, UV irradiation) the amount of propanol increased 14 fold and pentanol ($C_5H_{12}O$) was also detected. The appearance of the heavier alcohols at or above 150 °C is consistent with a FTS-like mechanism becoming active as the thermal energy approaches

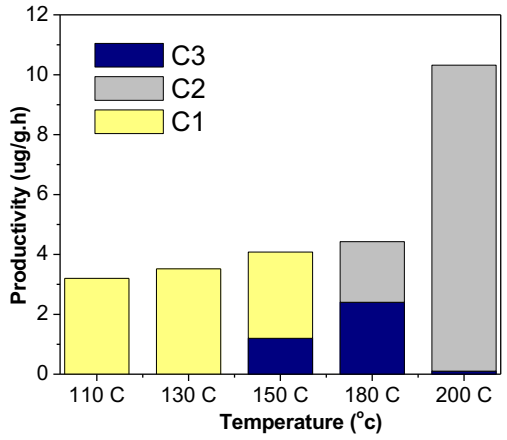

Figure 5-2. Mass productivity and C_n selectivity as a function of photothermal reactor temperature at 1 bar and P_{H2O}/P_{CO2} =1.2, and 40 sccm.

the activation energy needed for chain formation.[37,38,40] In a related study of the effect of temperature on the photochemical reduction of CO_2 to methane over TiO_2, Saladin and Alzneit showed that the rate of methane formation increases upon going from 20 to 200 °C, indicating the rate determining step is a thermal process.[41] Significantly, no higher C_n products were reported which we suspect is because they lacked a proper FTS co-catalyst, such as cobalt. In our current system, the kinetics of the carbon chain forming reactions seem to be rate determining at approximately 200 °C. Further experiments were run at 200 °C at three total pressures (1.0, 2.7, and 6.1 atm) and two partial pressure rations: P_{H2O}/P_{CO2} = 0.6 and 1.2. This data is collected in Table 1, which reports the mean productivity for each run, in units of mass productivity ($\mu g_{prod} \cdot g^{-1}_{cat} \cdot h^{-1}$) and molar productivity ($\mu mol_e \cdot g^{-1}_{cat} \cdot h^{-1}$, where μmol_e = μmol electrons stored in the product) of the catalyst in terms of product C_n. The products are divided into O_2, H_2, C_1, C_2-C_4 and C_5+, with certain higher C_n products explicitly listed. For data in which standard deviations are reported, the values are the mean of 3 independents runs, whereas those without

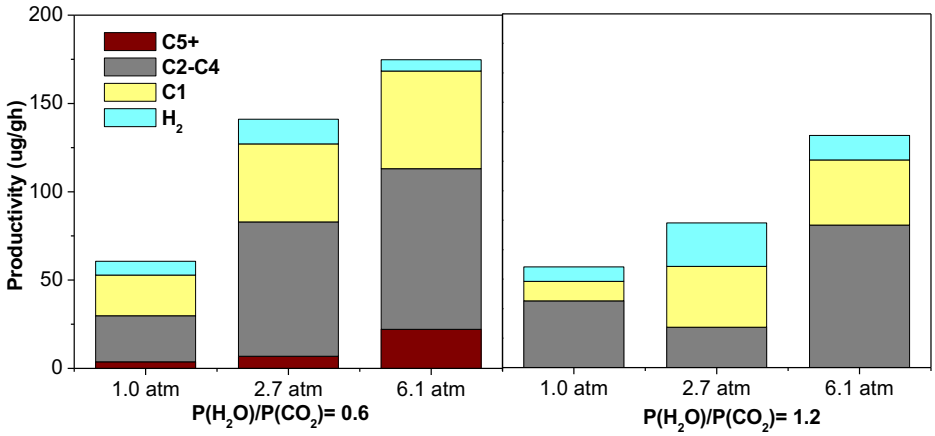

Figure 5-3. Mass productivity and selectivity of SPARC reaction at different pressure and partial pressure ratios at 200° C and 40 sccm.

are single run data. The full product distribution and productivity data is given in Tables S4 and S5 in the SI.

Figure 5-3 is a bar graph comparing the mass productivity and selectivity as a function of pressure and feedstock ratio. The most compelling data is the observation that the C_2+ hydrocarbons and oxygenates are not minor products but instead constitute 74% by mass of the products under one of the best set of conditions screened (6.1 bar, P_{H2O}/P_{CO2} = 0.6). Converted to a molar basis (moles of reducing electrons stored in products), this amounts to and 68% of all electrons stored in products in C_2+ hydrocarbons. Of this 22% by mass and 14% of the electrons are stored in liquid C_5+ products. The percentage of oxygenates in our product distribution (70 to 90%) is much higher than found in typical FTS chemistry which may be expected in a process that is considerably richer in oxygen overall and simply reflects some of the differences in SPARC vs FTS chemistry. It is not yet clear how or if the selectivity of the SPARC reaction can be tuned towards less oxygenated products. Nonetheless, most of these oxygenates are high molecular weight molecules with a greater fuel value on a mass basis than lighter alcohols or oxygenates. The H_2 and C_1 products account for 35% of product mass and 29 % of all electrons stored, but they are not the dominant products. In both feedstock ratios, we clearly observe an increase in overall productivity with increasing total pressure. However, only at the lower P_{H2O}/P_{CO2} of 0.6 do we observe any C_5+ selectivity and this increases with increasing pressure. Clearly, the feedstock ratio is an important parameter that merits further investigation and optimization. These data reveal that to a first approximation, the SPARC reaction responds to temperature and pressure in a manner similar to the FTS reaction and yields similar products. Because of this, we believe it is reasonable to assume some shared underlying chemical mechanisms. It is well-known that the FTS reaction responds to increases

in pressure with an increase in productivity (gram product per gram catalyst per hour) and a shift in product distribution (selectivity) towards heavier hydrocarbons,[40] and that the optimized industrial conditions are generally given around 20 atm with a 2:1 ratio of H_2 and CO for a cobalt-

based catalyst.[42,43] We assume that higher pressures will shift the selectivity in SPARC chemistry to favor higher C_n products, but our current reactor could not safely go beyond 6.1

Table 5-1. Products and mass and molar electron productivity as a function of pressure and partial pressure ratio at a constant temperature of 200 °C and flow rate of 40 sccm.

	Mass Productivity (P_m, μg/gh)						**Molar Productivity (P_{mol}, μmol_e/gh)**					
P_{H2O}/P_{CO2}	**0.6**			**1.2**			**0.6**			**1.2**		
Pressure	**1.0**	**2.7**	**6.1**	**1.0**	**2.7**	**6.1**	**1.0**	**2.7**	**6.1**	**1.0**	**2.7**	**6.1**
Compound	**P_m**	**P_m**	**P_m**	**P_m**	**P_m**	**P_m**	**P_{mol}**	**P_{mol}**	**P_{mol}**	**P_{mol}**	**P_{mol}**	**P_{mol}**
O_2	195±149	308±118	171±140	194	138	307	24±19	39±15	21±18	24	33	38
H_2	8±9	14±4	6±2	6	20	10	8±9	14±4	6±2	6	18	10
C_1	23±12	44±63	55±72	8	4	28	2±1	4±4	4±5	1	3	2
C_{2-4}	26±17	76±40	91±79	28	6	60	7±5	15±11	19±17	10	13	13
C_5+	4±5	7±11	22±13	0	0	0	1±2	4±5	5±8	0	1	0
Total (less O_2)	**61±5**	**141±27**	**175±39**	**43**	**30**	**98**	**18±3**	**36±3**	**35±6**	**17**	**35**	**26**
O_2 yield (%)							**136**	**108**	**62**	**140**	**94**	**150**
IPQY (%)							**0.02**	**0.05**	**0.04**	**0.02**	**0.04**	**0.03**
Select Prod												
$C_5H_{12}O$	3.7±5.2	1.6±1.9	1.7±2.1	0.0	0.0	0.0	1.3±1.8	0.8±0.7	0.6±0.7	0.0	0.0	0.0
C_7H_{12}	0	0.4±0.6	0.0	0.0	0.0	0.0	0.0	0.2±0.3	0.0	0.0	0.0	0.0
C_8H_{18}	0	0.4±0.6	0.0	0.0	0.0	0.0	0.0	0.2±0.3	0.0	0.0	0.0	0.0
$C_8H_{16}O_5$	0	0.0	2.2±3.8	0.0	0.0	0.0	0.0	0.0	0.4±0.8	0.0	0.0	0.0
C_9H_{12}	0	0.6±1.1	0.0	0.0	0.0	0.0	0.0	0.0	0.0	0.0	0.0	0.0
$C_{10}H_{20}O_2$	0	0.4±0.8	0.5±1.1	0.0	0.0	0.0	0.0	0.3±0.4	0.7±0.2	0.0	0.0	0.0
$C_{13}H_{12}$	0	0.9±1.5	0.0	0.0	0.0	0.0	0.0	0.5±0.7	0.0	0.0	0.0	0.0

bar. A new photoreactor capable of tolerating both higher temperatures and pressures is under construction and will allow us to test this.

Isotopic labelling experiments performed with $^{13}CO_2$ and D_2O feedstocks show incorporation of both labels into all of the reduced products (see SI). The O_2 yields, shown in Table 1, were calculated by dividing all the electrons released to form O_2 from H_2O by all the electrons stored in the identified products at the expected stoichiometry for the SPARC reaction and range from 64 to 150%. The agreement is acceptable considering the large standard deviations in these measurements, which reflect difficulties in obtaining good peak integration due to large adjacent CO_2 and N_2 peaks in the chromatogram (see Fig. S6).

As seen in Fig. 4, no O_2 and only trace hydrocarbons are detected before the catalyst bed is irradiated. Although difficult to see, there is a small amount of H_2, CH_4, and C_2H_6, produced during the dark period, constituting less than 10% of the CH_4 and C_2H_6 observed once the light is on. These basal products are attributed to thermal reactions of H_2O and CO_2 with the freshly prepared and highly reactive nanosized cobalt islands (catalyst preparation and characterization are given in the SI), some of which are unstable towards oxidation. When the catalyst is irradiated there is a substantial increase

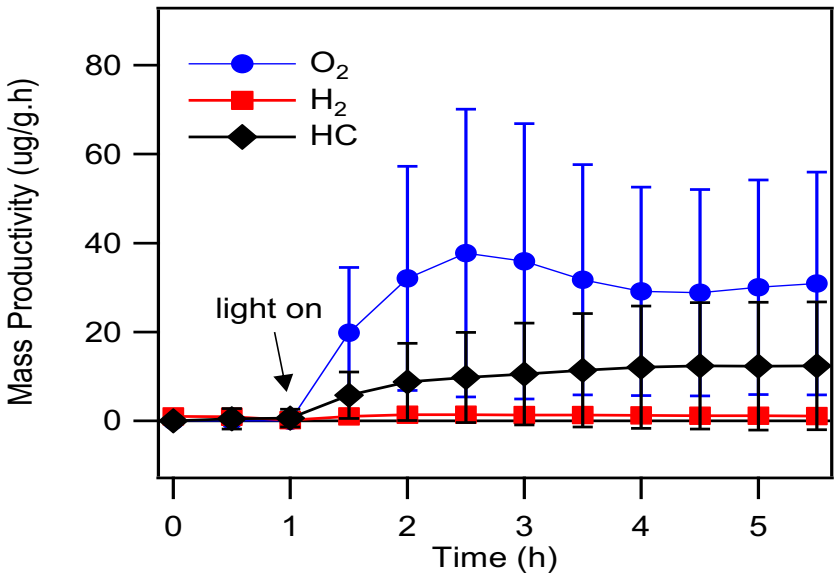

Figure 5-3. Productivity of O_2 (blue circles) H_2 (red squares) and hydrocarbons (HC) (black diamonds) as a function of time at 200 °C, 6.1 bar, P_{H2O}/P_{CO2} = 0.6 and 40 sccm.

in HC, H_2, and O_2 productivity consistent with a coupling of photochemical water oxidation with thermal CO_2 and proton reduction. Furthermore, the productivity is reasonably stable over the run period, however TEM analyses of the catalyst pre and post run reveal substantial agglomeration of the cobalt islands over this period (see SI Figure S2). The initial cobalt islands averaging 4.5 nm in diameter doubled in size over the 5 h run timeframe. It is well-established in FTS chemistry with cobalt-based catalysts that the catalyst undergoes considerable reorganization in the first 24 h of on stream use[44,45]and it is likely that a similar reorganization is occurring here. However, given the early stage of SPARC chemistry, there is not yet enough data to more adequately explain the catalyst behavior or its implications. It suffices to say that this phenomenon bears additional study.

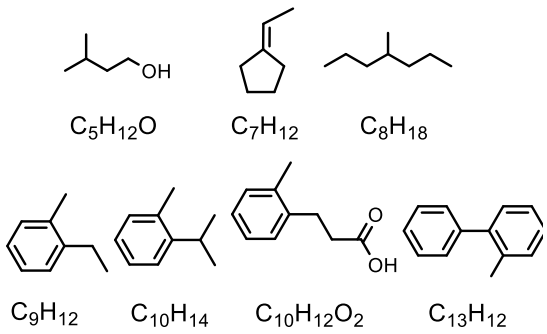

Figure 5-4. Structures of select C_5+ products as determined from NIST mass spectral database.

Table 1 also lists the productivity data for select C_5+ products, whose structures are shown in Fig. 5-4. The structures were determined by NIST database matching of the mass spectrum fragmentation patterns and were fit with confidence level greater than 99% for nearly all compounds. $C_5H_{12}O$ and C_8H_{18} are two saturated hydrocarbons typical of an FTS-like mechanism. The alkylbenzenes or oxygenates thereof suggest formation of surface acetylides/acetylenes, which can easily undergo cyclotrimerization to lead to the observed products.[46] This second C-C chain forming pathway is reasonable if we consider that the SPARC reaction conditions are considerably less hydrogen-rich relative to normal FTS, which rarely yields alkynes. While this unexpected mechanism seems to be

responsible for the aromatic C_6+ products, the presence of C_8H_{18} as well as C_7 and C_5 alkanes and olefins support a FTS process is occurring concurrently.

The highest mass productivity obtained 200 °C, 2.7 bar, P_{H2O}/P_{CO2} = 0.6, corresponded to 217 $\mu g \cdot g^{-1} \cdot h^{-1}$, not including O_2, or a molar electron productivity of 41 $\mu mol_e \cdot g^{-1} \cdot h^{-1}$. For comparisons, this latter value is ~20 μmol $H_{2(equiv)} g^{-1} \cdot h^{-1}$ and is within the typical range of 0.2 to 100 μmol product$\cdot g^{-1} \cdot h^{-1}$,[47, 48] reported for CO_2/H_2O semiconductor photocatalysis, although claims as high as 2000 μmol ethanol $g^{-1} \cdot h^{-1}$ exist.[49] When examined with respect to the incident photon flux ($\lambda \leq 400$ nm), an incident photon quantum yield (IPQY) of 0.02 to 0.05% is obtained on a per electron stored basis. These IPQYs are slightly higher if reported relative to the O_2 yield. Unfortunately, many studies of CO_2/H_2O semiconductor photocatalysis either do not report quantum yields or do not report them in a consistent manner. Where data exist, typical IPQY values are anywhere from 0.001% to 30%, although the higher values (> 1%) were only seen with non-oxide catalysts (i.e. ZnS, CdS, GaP).(24) We suggest that our modest IPQY is more a reflection of the early stage of this work rather than any practical limitation and note that a significant (2.5-fold) jump in IPQY was observed upon increasing the pressure from 1 bar to 2.7 bar, however, no further increase was seen at 6.1 atm.

As mentioned previously, the choice of a good metal for FTS catalyst is crucial and Fe, Co, and Ru are among the best known.[39] Here, we chose cobalt due to its known FTS performance and superior stability relative to iron,[42] and to demonstrate the SPARC reaction could be achieved without the requirement of rare or precious metal co-catalysts. In one of the few studies of the CO_2/H_2O semiconductor photocatalysis at temperatures in excess of 100° C, only C_1 products were found with copper and platinum zincates and titanate photocatalysts.[50] However, when Fe was used in the same systems ethanol in addition to the C_1 products was

observed,[51] suggesting the SPARC reaction was in operation. It is curious that even higher C_n products were not observed, but these photoreactions were conducted at temperatures in excess of 300° C which may well be too high for good operation. Oddly enough, cobalt-based catalysts yield primarily methane during the hydrogenation of CO_2.[52, 53] It was also shown that the increase water partial pressure stabilized the catalyst and it may be that the even higher P_{H2O} is influencing the SPARC product distribution here.

In general, elevated temperatures are avoided in photochemical reactions due to increased rates of charge recombination in the photocatalyst. For example, the photoluminescence (PL) intensity of TiO_2 drops by 50-60% upon raising the temperature from 20 to 200 °C.[54,55] At present, we observe an increase in productivity with temperature, showing a significant thermal component to the rate-determining kinetic step in this photothermochemical reaction. Nonetheless, the losses in charge carriers could be an important consideration upon development of an improved SPARC catalyst, where the thermal steps are no longer rate determining.

At present, this gas phase SPARC reaction is far from optimized and simply shows proof of principle. Higher productivities and better product distributions are likely to be realized as pressure, temperature, reactant ratio, space velocity, and catalyst are optimized. For example, the current photoreactor can only safely be operated at pressures less than 6.1 bar whereas higher pressures are likely to dramatically affect product selectivity and productivity. Similarly, BET surface area measurements reveal that the Nafion polymer, used to bind the catalyst powder to the glass beads, effectively covers up 50-60% of the catalyst surface area (see SI), revealing that we can likely do better using alternative methods to immobilize the catalyst. The current data also raise a number of important questions which must be addressed if this

technology is to be further developed. As both H_2 and CO are observed in the product stream, it is not clear if they are responsible for hydrocarbon formation via the FTS upon readsorption or if they represent a small fraction of surface escaped species. The most commonly involked mechanim for metal co-catalysts on photoactive TiO_2 is that the metal islands act as electron collectors upon which metal hydrides and CO_2 adsorption/reduction occurs while the holes migrate to the TiO_2 surface where they oxidize water. In a gas phase model, the protons must migrate over the surface of the TiO_2 to the cobalt islands, leading to questions as to the degree of surface hydration. It is notable that in the hydrogenation of CO or CO_2 on cobalt metal common surface same surface intermediates are invoked, even though the former gives hydrocarbon chains and the later gives methane.[52,53]

Although the current SPARC technology is currently impractical on a commercial scale, it does offer a conceptually new and commercially promising solar fuels technology that would be simple and inexpensive relative to most PV-EC and PEC systems. In a field operation, it is easy to imagine the use of parabolic mirrors to focus and concentrate sunlight onto a catalyst bed, providing both the photons required for photoexcitation and the thermal energy needed to run the reaction. Assuming such a system may require active cooling, the excess thermal energy could be used for product separations or other applications in which relatively low grade heat can be applied. In this respect, a SPARC process can realize greater efficiencies than process requiring ambient or near ambient temperatures in that the low energy photons are either used to help heat the SPARC reaction or are used to heat a working fluid to a more useful temperature (i.e. 200 °C). Concentrated sunlight minimizes photocatalyst costs and reactor volume, the former of which is often one of the more expensive components of any such technology. The direct production of the value-added hydrocarbons liquid fuel minimizes the number of unit

operations involved and the associated efficiency losses and capital expenses of each. Finally, the SPARC reaction, as realized here, is a true gas phase operation operating at conditions more typical of an industrial operation. The elevated temperature, pressure, and gas phase operation also open new possibilities about the types of semiconductors catalysts that are needed and may be used.

Supporting Information

Full experimental details for the reactor design and function, catalyst preparation and characterization, product identification, yield and distribution, and isotopic labelling are given in the supporting information (21 pages).

Acknowledgments

We thank Dr. Upendra Joshi helpful discussions and help with reviewing the manuscript. The National Science Foundation (CHE-1301332) and Robert A. Welch Foundation (Y-1301) are gratefully acknowledged for financial support.

References

1. Armaroli N & Balzani V (2010) Solar Fuels. *Energy for a Sustainable World*, (Wiley-VCH Verlag GmbH & Co. KGaA), pp 203-229.
2. Anonymous ed (2007) *Climate Change 2007 - The Physical Science Basis. Working Group I Contribution to the Fourth Assessment Report of the IPCC* (Cambridge University Press, Cambridge UK), p 1009.
3. Solomon S, Plattner G-K, Knutti R, & Friedlingstein P (2009) Irreversible climate change due to carbon dioxide emissions. *Proceedings of the National Academy of Sciences* 106(6):1704-1709.

4. Lewis NS & Nocera DG (2006) Powering the planet: Chemical challenges in solar energy utilization. *PNAS* 103:15729-15735.

5. Torella JP*, et al.* (2015) Efficient solar-to-fuels production from a hybrid microbial–water-splitting catalyst system. *Proceedings of the National Academy of Sciences* 112(8):2337-2342.

6. Song W*, et al.* (2011) Making solar fuels by artificial photosynthesis. *Pure Appl. Chem.* 83(4):749-768.

7. Liu C*, et al.* (2015) Nanowire–Bacteria Hybrids for Unassisted Solar Carbon Dioxide Fixation to Value-Added Chemicals. *Nano Letters* 15(5):3634-3639.

8. Steinfeld A (2005) Solar thermochemical production of hydrogen—a review. *Solar Energy* 78(5):603-615.

9. Cox CR, Lee JZ, Nocera DG, & Buonassisi T (2014) Ten-percent solar-to-fuel conversion with nonprecious materials. *Proceedings of the National Academy of Sciences* 111(39):14057-14061.

10. Barbir F (2005) PEM electrolysis for production of hydrogen from renewable energy sources. *Solar Energy* 78(5):661-669.

11. Kamat PV, Tvrdy K, Baker DR, & Radich JG (2010) Beyond Photovoltaics: Semiconductor Nanoarchitectures for Liquid-Junction Solar Cells. *Chemical Reviews* 110(11):6664-6688.

12. Kumar B*, et al.* (2012) Photochemical and Photoelectrochemical Reduction of CO2. *Annual Review of Physical Chemistry* 63(1):541-569.

13. Walter MG*, et al.* (2010) Solar water splitting cells. *Chemical reviews* 110(11):6446-6473.

14. Hisatomi T, Kubota J, & Domen K (2014) Recent advances in semiconductors for photocatalytic and photoelectrochemical water splitting. *Chemical Society Reviews* 43(22):7520-7535.

15. Gratzel M (2012) *Energy resources through photochemistry and catalysis* (Elsevier).

16. Alibabaei L*, et al.* (2013) Applications of metal oxide materials in dye sensitized photoelectrosynthesis cells for making solar fuels: let the molecules do the work. *Journal of Materials Chemistry A* 1(13):4133-4145.

17. Alibabaei L, Sherman BD, Norris MR, Brennaman MK, & Meyer TJ (2015) Visible photoelectrochemical water splitting into H2 and O2 in a dye-sensitized photoelectrosynthesis cell. *Proceedings of the National Academy of Sciences* 112(19):5899-5902.

18. Anonymous (2004) *The Hydrogen Economy: Opportunities, Costs, Barriers, and R&D Needs* (The National Academies Press, Washington, DC) p 256.

19. Centi G, Quadrelli EA, & Perathoner S (2013) Catalysis for CO2 conversion: a key technology for rapid introduction of renewable energy in the value chain of chemical industries. *Energy & Environmental Science* 6(6):1711-1731.

20. van der Giesen C, Kleijn R, & Kramer GJ (2014) Energy and climate impacts of producing synthetic hydrocarbon fuels from CO2. *Environmental science & technology* 48(12):7111-7121.

21. Halmann M (1978) Photoelectrochemical reduction of aqueous carbon dioxide on p-type GaP in liquid junction solar cells. *Nature* 275:115-116.

22. Inoue T, Fujishima A, Konishi S, & Honda K (1979) Photoelectrocatalytic Reduction of Carbon Dioxide in Aqueous Suspensions of Semiconductor Powders. *Nature* 277:637-638.

23. Chen X, Shen S, Guo L, & Mao SS (2010) Semiconductor-based photocatalytic hydrogen generation. *Chemical Reviews* 110(11):6503-6570.

24. Habisreutinger SN, Schmidt-Mende L, & Stolarczyk JK (2013) Photocatalytic reduction of CO2 on TiO2 and other semiconductors. *Angewandte Chemie International Edition* 52(29):7372-7408.

25. Hwang J-S, Chang J-S, Park S-E, Ikeue K, & Anpo M (2005) Photoreduction of carbondioxide on surface functionalized nanoporous catalysts. *Topics in catalysis* 35(3-4):311-319.

26. Kubacka A, Fernández-García M, & Colón G (2012) Advanced Nanoarchitectures for Solar Photocatalytic Applications. *Chemical Reviews* 112(3):1555-1614.

27. Ashford DL*, et al.* (2015) Molecular Chromophore–Catalyst Assemblies for Solar Fuel Applications. *Chemical Reviews*.

28. Song W*, et al.* (2013) Visualization of cation diffusion at the TiO2 interface in dye sensitized photoelectrosynthesis cells (DSPEC). *Energy & Environmental Science* 6(4):1240-1248.

29. Hoffmann MR, Moss JA, & Baum MM (2011) Artificial photosynthesis: semiconductor photocatalytic fixation of CO2 to afford higher organic compounds. *Dalton Transactions* 40(19):5151-5158.

30. Mizuno T, Adachi K, Ohta K, & Saji A (1996) Effect of CO2 pressure on photocatalytic reduction of CO2 using TiO2 in

aqueous solutions

J. Photochem Photobiol A 98:87-90.

31. Xia X-H*, et al.* (2007) Preparation of multi-walled carbon nanotube supported TiO2 and its photocatalytic activity in the reduction of CO2 with H2O. *Carbon* 45(4):717-721.
32. Subrahmanyam M, Kaneco S, & Alonso-Vante N (1999) A screening for the photo reduction of carbon dioxide supported on metal oxide catalysts for C1â€“C3 selectivity. *Applied Catalysis B: Environmental* 23(2â€“3):169-174.
33. Barton EE, Rampulla DM, & Bocarsly AB (2008) Selective Solar-Driven Reduction of CO2 to Methanol Using a Catalyzed p-GaP Based Photoelectrochemical Cell. *J. Am. Chem. Soc.* 130(20):6342-6344.
34. Cole EB*, et al.* (2010) Using a One-Electron Shuttle for the Multielectron Reduction of CO2 to Methanol: Kinetic, Mechanistic, and Structural Insights. *Journal of the American Chemical Society* 132(33):11539-11551.
35. Roy SC, Varghese OK, Paulose M, & Grimes CA (2010) Toward Solar Fuels: Photocatalytic Conversion of Carbon Dioxide to Hydrocarbons. *ACS Nano* 4(3):1259-1278.
36. Varghese OK, Paulose M, LaTempa TJ, & Grimes CA (2009) High Rate Solar Photocatalytic Conversion of Carbon Dioxide and Water vapor to Hydrocarbon Fuels. *NanoLett* 9(2):731-737.
37. Pendyala V, Shafer W, & Davis B (2013) Aqueous-Phase Fischer–Tropsch Synthesis: Effect of Reaction Temperature on Ruthenium Nanoparticle Catalyst and Comparison with Supported Ru and Co Catalysts. *Catalysis Letters* 143(9):895-901.

38. Zennaro R, Tagliabue M, & Bartholomew CH (2000) Kinetics of Fischer–Tropsch synthesis on titania-supported cobalt. *Catalysis Today* 58(4):309-319.

39. Vannice MA (1975) The catalytic synthesis of hydrocarbons from H2CO mixtures over the group VIII metals: I. The specific activities and product distributions of supported metals. *Journal of Catalysis* 37(3):449-461.

40. James OO, Chowdhury B, Mesubi MA, & Maity S (2012) Reflections on the chemistry of the Fischer-Tropsch synthesis. *RSC Advances* 2(19):7347-7366.

41. Saladin F & Alxneit I (1997) Temperature dependence of the photochemical reduction of CO2 in the presence of H2O at the solid gas interface of TiO2. *Chem. Comm.* 93(23):4159-4163.

42. Khodakov AY, Chu W, & Fongarland P (2007) Advances in the Development of Novel Cobalt Fischer−Tropsch Catalysts for Synthesis of Long-Chain Hydrocarbons and Clean Fuels. *Chemical Reviews* 107(5):1692-1744.

43. Visconti CG & Mascellaro M (2013) Calculating the product yields and the vapor–liquid equilibrium in the low-temperature Fischer–Tropsch synthesis. *Catalysis Today* 214:61-73.

44. Karaca H*, et al.* (2010) In situ XRD investigation of the evolution of alumina-supported cobalt catalysts under realistic conditions of Fischer-Tropsch synthesis. *Chemical Communications* 46(5):788-790.

45. Khodakov AY (2009) Fischer-Tropsch synthesis: Relations between structure of cobalt catalysts and their catalytic performance. *Catalysis Today* 144(3–4):251-257.

46. Vollhardt KPC (1984) Cobalt-Mediated [2+ 2+ 2]-Cycloadditions: A Maturing Synthetic Strategy [New Synthetic Methods (43)]. *Angewandte Chemie International Edition in English* 23(8):539-556.

47. Izumi Y (2013) Recent advances in the photocatalytic conversion of carbon dioxide to fuels with water and/or hydrogen using solar energy and beyond. *Coordination Chemistry Reviews* 257(1):171-186.

48. Mao J, Li K, & Peng T (2013) Recent advances in the photocatalytic CO 2 reduction over semiconductors. *Catalysis Science & Technology* 3(10):2481-2498.

49. Liu Y*, et al.* (2009) Selective ethanol formation from photocatalytic reduction of carbon dioxide in water with BiVO 4 photocatalyst. *Catalysis Communications* 11(3):210-213.

50. Guan G, Kida T, Harada T, Isayama M, & Yoshida A (2003) Photoreduction of carbon dioxide with water over K 2 Ti 6 O 13 photocatalyst combined with Cu/ZnO catalyst under concentrated sunlight. *Applied Catalysis A: General* 249(1):11-18.

51. Guan G, Kida T, & Yoshida A (2003) Reduction of carbon dioxide with water under concentrated sunlight using photocatalyst combined with Fe-based catalyst. *Applied Catalysis B: Environmental* 41(4):387-396.

52. Visconti CG*, et al.* (2009) Fischer–Tropsch synthesis on a Co/Al 2 O 3 catalyst with CO2 containing syngas. *Applied Catalysis A: General* 355(1):61-68.

53. Zhang Y, Jacobs G, Sparks DE, Dry ME, & Davis BH (2002) CO and CO 2 hydrogenation study on supported cobalt Fischer–Tropsch synthesis catalysts. *Catalysis today* 71(3):411-418.

54. Forss L & Schubnell M (1993) Temperature dependence of the Luminescence of TiO2 Powder. *Appl. Phys. B.* 56:363-366.

55. Schubnell M, Kamber I, & Beaud P (1997) Photochemistry at high temperatures - potential of ZnO as a high temperature photocatalyst. *Appl. Phys. A.* 64:109-113.

56. Cho-Ching L, Chung-Hsuang H, Chung-Shin Y & Jen-Fong W (2007) Photoreduction of carbon dioxide with H2 and H2O over TiO2 and ZrO2 in a circulated photocatalytic reator. Solar Energy Materials &Solar Cells 91 : 1765-1774.

57. Kenneth A. M & Robert B. M (2004) State of Understanding of Nafion. *Chem. Rev*. 104:4535−4585

58. Cullity B.D. & Stock S.R., *Elements of X-Ray Diffraction*, 3rd Ed., Prentice-Hall Inc., 2001, p 167-171, ISBN 0-201-61091-4.

59. Gribb, A. A.; Banfield, J. F(1997) Particle size effects on transformation kinetics and phase stability in nanocrystalline TiO2. *Am. Mineral*. 82, 717.

60. Lowell S, Shields JE, Thomas, MA & Thommes M.(2004) Characterization of Porous Solids and Powders: Surface Area, Pore Size and Density . Volume 16 of the series *Particle Technology Series* p 58-81

61. Narendra Pai K. R., Anjusree G. S., Deepak T. G., Subash D., Shantikumar V. Nair & Sreekumaran Nair A.(2014) High surface area TiO2 nanoparticles by a freezedrying approach for dye-sensitized solar cells. *RSC Adv.* 4, 36821–36827

Supporting Information

Solar Photothermochemical Alkane Reverse Combustion

Wilaiwan Chanmanee[1], Mohammad Fakrul Islam[1], Brian H. Dennis,[2]* Frederick M. MacDonnell[1]*

[1]Department of Chemistry and Biochemistry, [2]Department of Mechanical and Aerospace Engineering, University of Texas at Arlington, Arlington TX 76019

I. Catalysts preparation

1. ***Preparation of 5% Co/TiO_2 photocatalyst.*** The 5% by mass metallic cobalt on TiO_2 catalyst was prepared by wet impregnation of 5g Degussa P-25 TiO_2 with 1.25 g $Co(NO_3)_2$ (Alfa Asear) in 3 mL DI water. After completing the impregnation, the resultant Co/TiO_2 catalyst was dried overnight at room temperature and then calcined at 250 °C for 180 min. The dried powder was finely ground and immobilized on the glass beads as described in the next section.

2. ***The immobilized Co/TiO_2 catalyst*** The unreduced catalyst powder was supported in the flow reactor by coating it on Pyrex glass pellets (diameter of 2 mm) (Sigma Aldrich) following the procedure below. The glass pellets were etched in 5 M NaOH solution for 24 h at 70 °C to increase surface roughness. [S1] After extensive rinsing with DI water, the glass pellets were soaked in aqueous suspension of 3 g unreduced Co/TiO_2 powder dispersed in 3.0 mL of DI water with the aid of an ultrasonic bath. Subsequently, 3.0 mL of a Nafion polymer solution (5% Nafion D521 in water/1-propanol Alfa Aesar) was slowly added and the solution stirred for 10 min during which time the majority of the powder adhered to the pellets. The suspension was decanted off and the pellets washed with DI water which was removed by decanting. Finally, the pellets were placed in an oven at 100 °C under N_2 atmosphere and dried for 4 h. No 1-propanol was detected by GC after the baking and loading the pellets into the flow reactor. The catalyst was then reduced in situ by flowing H_2 gas over the fixed-bed photocatalyst reactor at 350 °C for 12 h.

3. **Catalyst Characterization**

XRD (X-ray powder diffraction)

The crystal phase of Co on TiO_2 catalyst was analyzed by XRD and recorded on a Bruker D8 diffractometer using Cu Kα radiation with a step size of 0.01° in the range of 15–85°. The step time was 1 second, which was long enough to obtain a good signal-to-noise ratio in the mean reflections of the two studied TiO_2 crystalline phases, (101) anatase (2θ ~ 25.237) and (110) rutile (2θ ~ 27.365). The average particle size was estimated by applying the Scherrer's formation[S2] on the anatase (101) (the highest intensity peak) as show in Equation 1

$$L = \frac{K\lambda}{\beta \cos\theta} \qquad (1)$$

Where L is the crystallite size, K a constant (usually 0.89), λ the wavelength of the X-ray radiation (0.15418 nm of Cu Kα), β is the line width at the half-maximum height and θ is the corresponding diffraction angle in degrees. The weight fraction of each TiO_2 phase in catalyst were calculated from XRD spectra by the following equation 2[S3]

$$W_R = \frac{A_R}{0.884A_A + A_R} \qquad (2)$$

Where A_A represents the integrated intensity of the anatase (101) peak and A_R the integrated intensity of the rutile (110) peak. The particle size and mass fractions are given in Table S1 and the XRD spectra shown in Figure S1.

As seen in both Table S1 and Fig. S1, anatase was the predominant structure in the cobalt-TiO_2 before and after the runs (a typical run was 5-8 h). When comparing the diffractograms of the synthesized catalysts that were modified with cobalt, it was observed that the catalyst samples show no changes in crystallinity, direction of crystals, or changes of phase. However, no peaks corresponding to Co, CoO, or Co_3O_4 were observed in the XRD due the low cobalt loading and high cobalt dispersion.

Table S1. Weight fraction of phase and crystal size of catalysts

Sample	Weight fraction of phase (%)		Crystal size (nm)
	Anatase	Rutile	
Pre run TiO_2-Co (reduced)	83	17	40
Post run 1.0 bar	81	19	39
Post run 2.7 bar	84	18	38
Post run 6.1 bar	81	19	41

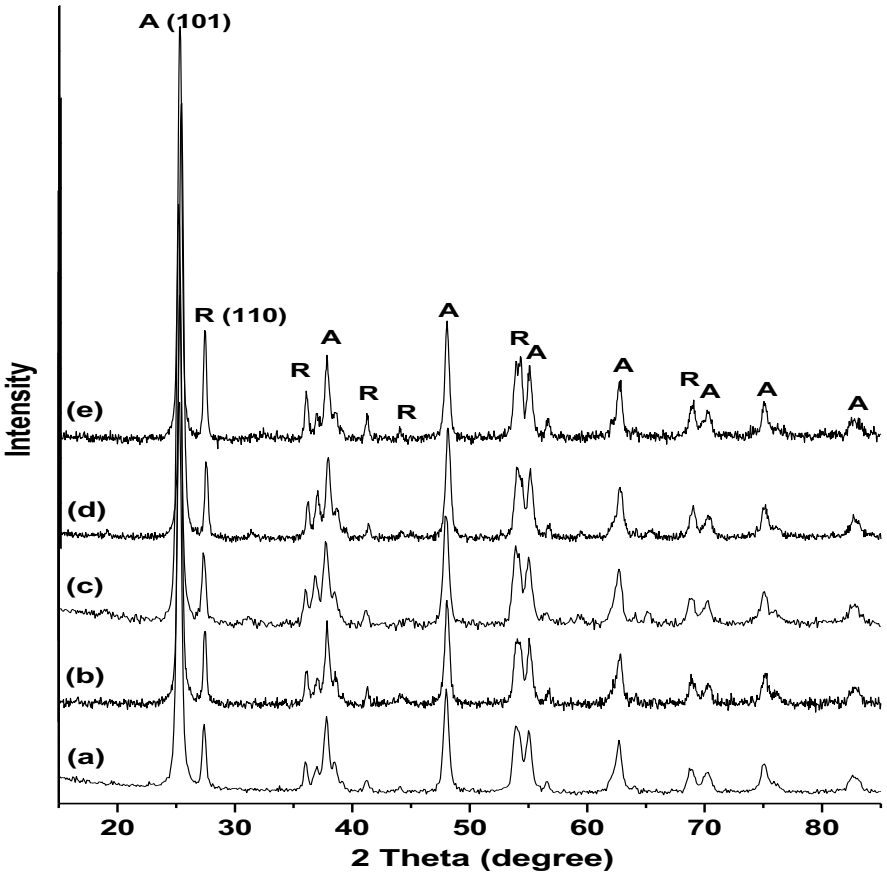

Figure S1. XRD analyses of (a) TiO_2 Degussa P25 powder (b) pre-run reduced Co/TiO_2 catalyst, post run after UV irradiation, 200 °C, P_{H2O}/P_{CO2} 0.6, flow rate 40 sccm at a total pressure of (c) 1.0 bar, (d) 2.7 bar, (e) 6.1 bar. (A) = anatase, (R) = Rutile

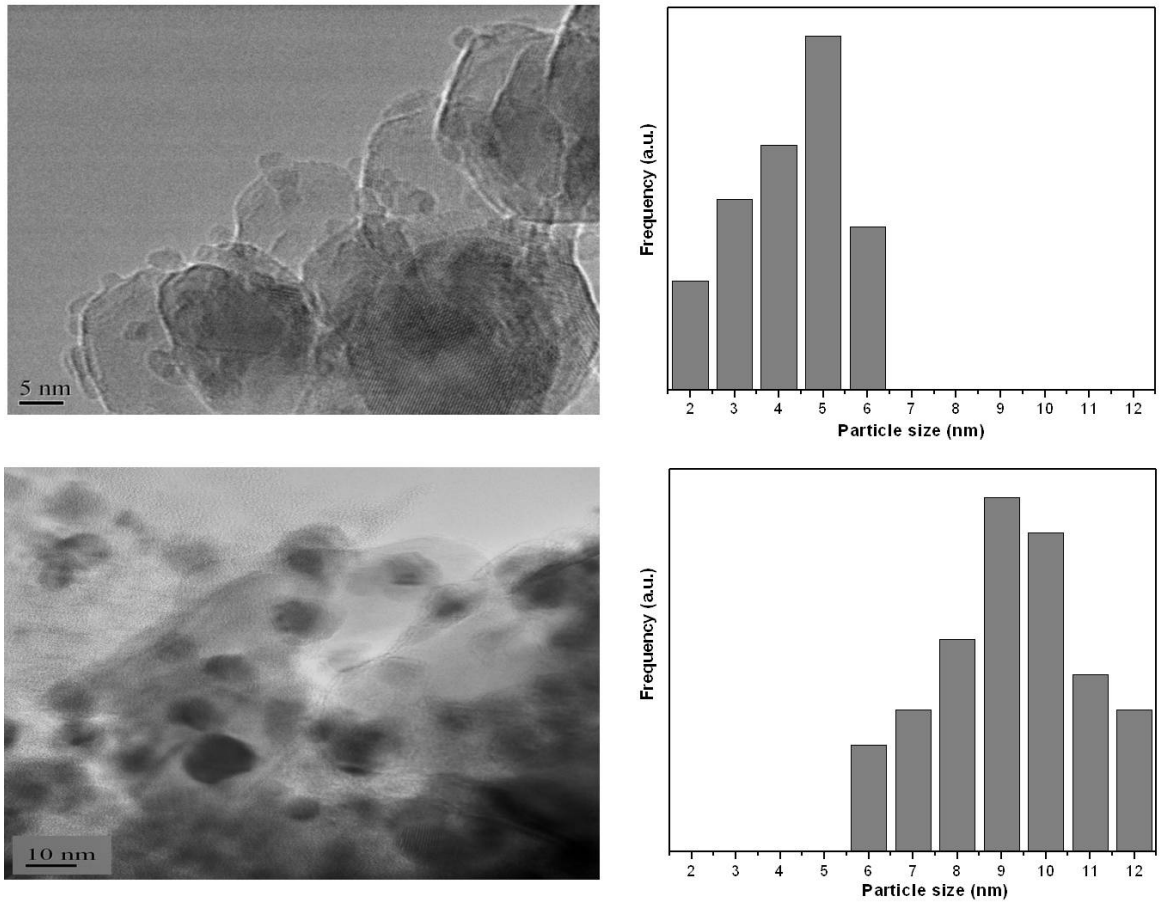

Figure S2. TEM images for (top left) the reduced, pre-run Co/TiO_2 catalyst and (top right) histogram of cobalt-island size, (bottom left) post 5 h run (6.1 bar, 200 °C, $P_{H2O/CO2}$ 0.6, flow rate 40 sccm) Nafion coated, and (bottom right) histogram of cobalt-island size.

The morphology of the Co/TiO_2 catalyst was observed using transmission electron microscopy (TEM, Hitachi H-9500) as shown in Figure S2. Figure S2 (a) shows the TEM image of the 5 wt.% Co/TiO_2 catalyst after reduction, but before the run. The images show TiO_2 (Degussa P25) crystallites on the order of 20.2 ±4 nm with small sports which are Co-metal particles which are highly dispersed on the TiO_2 support. The cobalt cluster sizes are seen to be in the range 4.5 ± 2.0 nm. The TEM images of same catalyst after 5 h reaction at 6.1 bar, 200 °C are shown in Fig S2 (b-d). Some small cobalt metal clusters are still observed however there appears to be considerable aggregation of most of the cobalt particles are now 9.7 ± 2.5 nm in diameter, as seen by the larger dark spots. The post-run sample gave poorer quality images which we presume is due to interference from the Nafion binder, which is not completely removed via washing.

XPS (X-ray photoelectron spectroscopy)

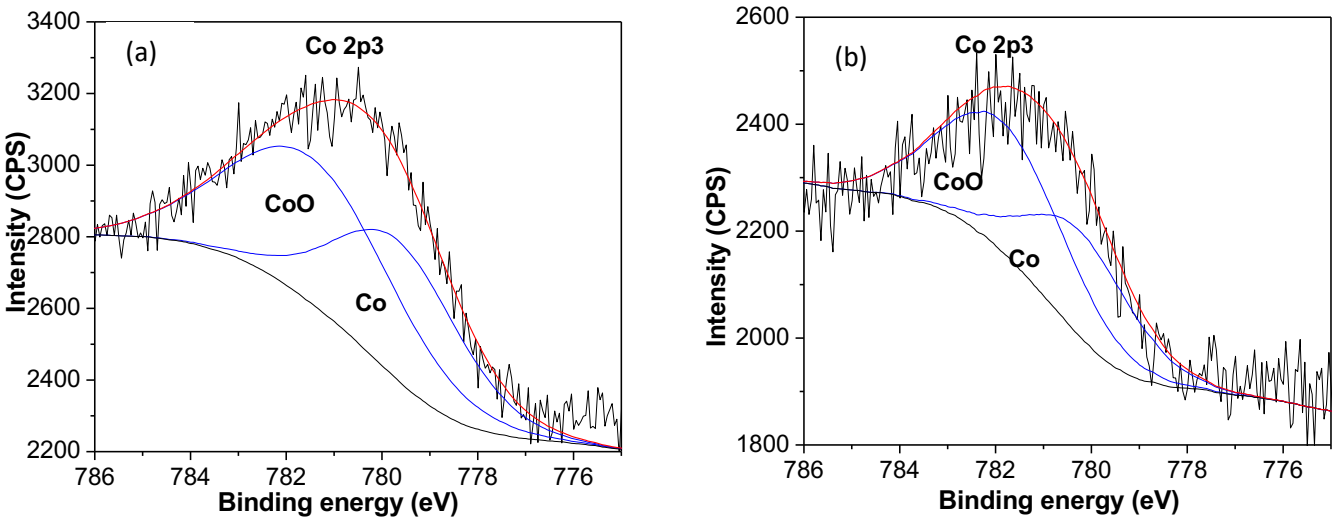

Figure S3. High-resolution XPS analyses of (a) pre-run, reduced Co/TiO_2 catalyst and (b) post-run cobalt/TiO_2 catalyst after being subjected to SPARC reaction at 2.7 bar, 200 °C for 8 h.

X-ray photoelectron spectroscopy (XPS) was performed on a Perkin Elmer/Physical Electronic Model 5000C instrument. Post run samples required washing otherwise all surface catalyst peaks were obscured by the Nafion coating. Washing consisted of extensive rinsing with 95% ethanol and then DI water, after which reasonably good spectra could be obtained. XPS data for the pre-run, reduced cobalt/TiO_2 catalyst is shown in Fig. S3a with the energies associated with the binding energies for Co(II) (778 eV) and Co(0) (780 eV) fit to two peaks to reproduce the observed spectra. Because these two peaks are so close together, the fitting is approximate and gave a 60:40 ratio of Co(II) to Co(0) representing a real loading of ~2.1% Co metal, at the beginning of the run. It is not known if the CoO present has any role in the observed chemistry. Post run XPS analysis of washed catalyst is shown in Fig. S3b with the only difference being a slight decrease in the percentage of Co(0)

present, with a ~65:35 Co(II)/Co(0) ratio, leading to a final metallic cobalt loading of 1.8%. This small amount of cobalt oxidation could account for up to one-third of the product in the best run data however it seems unlikely that cobalt oxidation is a major contributor to the reduced products given the following considerations. The observation of an excess or near stoichiometric amount of O_2 with the reduced products upon irradiation supports a photochemical reaction. In addition, the majority of cobalt oxidation likely occurred during the reactor warm up, a period in which only CO_2 gas was introduced and during the initial dark period, when steam was introduced. During these dark phases, the most reactive and unstable cobalt islands are likely oxidized, and this correlates well with the observation of an initial H_2 spike when the reaction is first monitored. This is seen in a blow-up of the dark phase data for Figure 5-3 in the manuscript, shown in Fig S4. Finally, it is not known how the post-run washing affected the Co^{2+}/Co^0 ratio, but it is likely to contribute a little towards some of the observed oxidation.

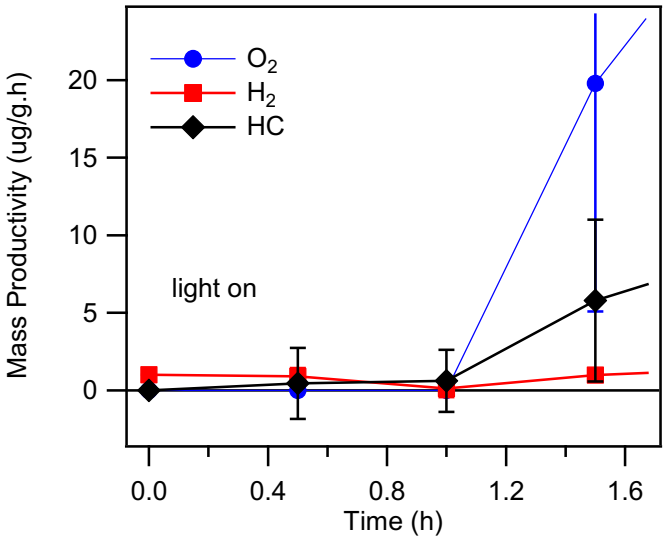

Figure S4. H_2 and HC evolution during the warm-up and dark period before catalyst irradiation.

Surface area (BET)

Brunauer-Emmett-Teller (BET) surface area and BJH average adsorption- desorption pore diameter and pore volume measurement were conducted using a Micromeritics Tri-Star system. [S4,S5] A precisely weighed 0.3 g of reduced catalyst sample was taken and slowly heated to 250 °C for 24 h under N_2. The sample was then transferred to the adsorption unit, and the N_2 adsorption was measured at the boiling temperature of nitrogen.

Table S2. BET surface area of Co/TiO_2 catalyst with or without Nafion.

Catalyst	Surface area (m^2g^{-1})	Pore size (nm)	Pore volume (cm^3g^{-1})
TiO_2	51.5	9.7	0.07
5 wt.% Co/TiO_2 (reduced powder)	44.5	15.3	0.18
5 wt.% Co/TiO_2 (reduced powder coated on glass pellets with Nafion after drying (100 °C for 4 h))	0.27	14.1	0.001
5 wt.% Co/TiO_2 (reduced powder coated on glass pellets with water after drying (100 °C for 4 h))	0.67	16.2	0.004

As seen from the data in Table S2, the surface area of the catalyst drops considerably but as expected when coated onto glass pellets. However, this dispersion was necessary to allow for good gas flow in the packed reactor. Initial attempts to coat the pellets using no binder resulted in a mechanically unstable film which would fall off during a reaction run. The use of the perfluorinated, sulfonated Nafion polymer added

mechanical strength to the films but as seen in the surface area measurements, it also had the effect of reducing the available catalyst surface area by ~ 60% and the accessible pore volume by 75%. We are in the process of designing and fabricating a second generation photoreactor in which thin film deposition will be far more straightforward and the mechanical strength of the film less demanding, thus allowing us to avoid the Nafion binder completely. However, for this proof of concept study, the Nafion was necessary.

II. Continuous Flow Fixed-bed photo-thermal reactor

The reactor was composed of a single quartz tube and two aluminum caps on each end. The quartz tube had the length of 2.54 cm, outside diameter of 3.65 cm and a wall thickness of 0.32 cm. Two Viton®Fluoroelastomer O-rings were placed on each cap to prevent leaks. A metal clamp was used to axially secure the caps when the reactor was pressurized.

Internal heating was used to control the reaction temperature. A stainless-steel tube with the diameter of 0.635 cm and length of 2.54 cm was place along the center of the reactor to hold a 750W cylindrical cartridge heater in place. The heater was powered by a variac transformer and was connected to a Proportional Integral Derivative (PID) controller. Feedback for the PID controller was provide by a K-type thermocouple placed halfway between the between the cartridge heater and the reactor wall. The PID controller was programmed to hold the desired reaction temperature as a function of time.

The top cap contained three fittings, one to hold the thermocouple, another for the stainless-steel tube holding the heater, and one for gas and water vapor input. The bottom cap contained a single fitting for the flow outlet.

Experiment Setup The schematic for the setup is shown in Figure S5. CO_2 was fed through an O_2 scrubber (Restek Cat no# 20601) to remove trace O_2 from the CO_2 source. No O_2 was detected by GC (described below) in the feed gas after this scrubber had been added. The reactor pressure was set by adjusting the delivery pressure on the CO_2 tank regulator. A back-pressure regulator valve was used to control the flow rate of CO_2 into the reactor. A mass flow meter was used to monitor the flow rate. Degassed water which prepared by slowly bubbling with N_2 through the liquid to remove oxygen from water was pumped (HPLC pump, Shimadzu LC 20ADXR) continuously into a fitting wrapped with a cord heater that was connected to a Variac transformer. A thermocouple in the fitting was used to monitor the temperature. The Variac was adjusted to give a temperature larger than 100 ^oC. The resulting steam was directed into the reactor where it mixed with the CO_2 stream. The reactant mixture then passed over the catalyst-coated glass bead bed, which was irradiated by four UV lamps (PHILIPS 250W Mercury Vapor Light Bulb) located outside of the reactor. The hot vapor stream passed out of the reactor and into a pressurized liquid-gas separator vessel that was surrounded by an ice bath. Liquids were collected in a glass vial contained in the separator and gases were directed through an adjustable outlet valve. The gases were then directed to an online gas chromatograph to be identified and quantified.

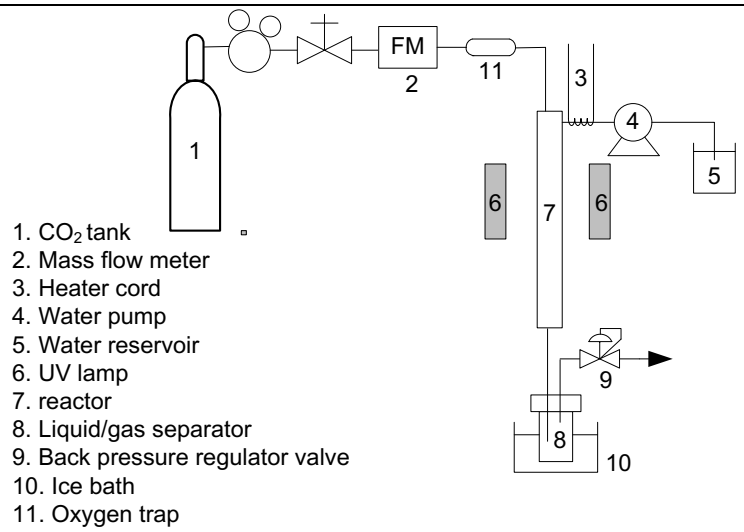

Figure S5: Schematic for the experimental setup

Experimental Method The catalysis-coated glass beads were packed fully inside the quartz tube before each experiment. The CO_2 flow rate was kept at 40 sccm for all runs. The water to CO_2 partial pressure ratio was controlled between 0.6 and 1.2 by adjusting the water flow rate of pump. The temperature for the experiments was set to range from 110 to 220 ºC. All four Hg lamps were used at their maximum intensity (1000W total) for all experiments. The power density was measured in mW/cm^2 every 10 nm and measured between 200 nm and 400 nm and the resulting data converted into a total photon flux over that range. The experiments were run under different pressures from 1.0-6.1 bar for 5-8 hours. The outlet valve was adjusted to maintain the desired 40 sccm CO_2 flow rate for each pressure.

III. Product detection using GC- MS and on-line GC

Gas Chromatography with mass spectra detection The condensable liquid products consisted of a single phase with noticeable changes in the meniscus behavior. The

total solution was placed in a 10.00 mL volumetric flask and made up to 10.00 mL with DI water. This 10.00 mL solution was extracted with 1.00 mL dichloromethane (DCM) and the aqueous phase decanted off. The DCM solution was used as is for analysis by GC-MS. Calibration curves for common analytes such as methanol, ethanol, acetic acid, etc. were prepared by taking 10.00 mL of a known concentration if aqueous solution and subjecting them to the same extraction procedure. A 1 µL aliquot of the DCM solution was injected into the GC-MS instrument, which was a Shimadzu GC-MS-2010SE chromatograph with a MS QP2010 detector and an AOC-4 20S autosampler. The chromatographic column was Shimadzu SHRX105MS (30-m length and 0.25-mm inner diameter, part # 220-94764-02), and helium was used as the carrier gas. The initial oven temperature was 40 °C held for 5 min, followed by ramp to 150 °C at 10°C/min. The injection port and detector temperatures were both 200 °C. The temperature of the ion source (electron ionization mode, 70eV) was 250 °C. The MS detector was set at 250 °C. Samples were run in the SIM and SCAN mode over a mass-to-charge (m/z) ratio range of 20-250. The heavier GC-MS products were characterized by analysis of their mass spectrum with a NIST library were using the Shimadzu GCMS solution v4.11 software package.

Online Gas Chromatography The gas products were analyzed during the synthesis reaction process, a reactor was connected to Shimadzu 2014 Online-Reactor Gas Analyzer which has been customized for the analysis of light gases and refinery-type gases by Custom Solutions Group of Katy, TX. This package includes a comprehensive list of common refinery gases, complete with retention-time, detector response, and calibration curves. O_2, H_2 and CO were also checked against three standard gas mixes obtained from Mattheson to assure a good calibration. The custom GC featured a 250 μL sample loop with an automatic valve for sample injection and samples were analyzed every 30 min. The hydrocarbon gases such as methane, ethane and propane were analyzed using an Agilent Al_2O_3/Na_2SO_4 (50-m length and 0.53-mm inner diameter) capillary column. The column was set to 70 °C hold for 3 min and ramp 15 °C /min until 200 °C and hold for 10 min with FID detector at 250 °C. For the H_2, O_2 and CO were analyzed using *Molecular sieves 5A* 80/100 and *HayeSep Q*, 80/100 mesh

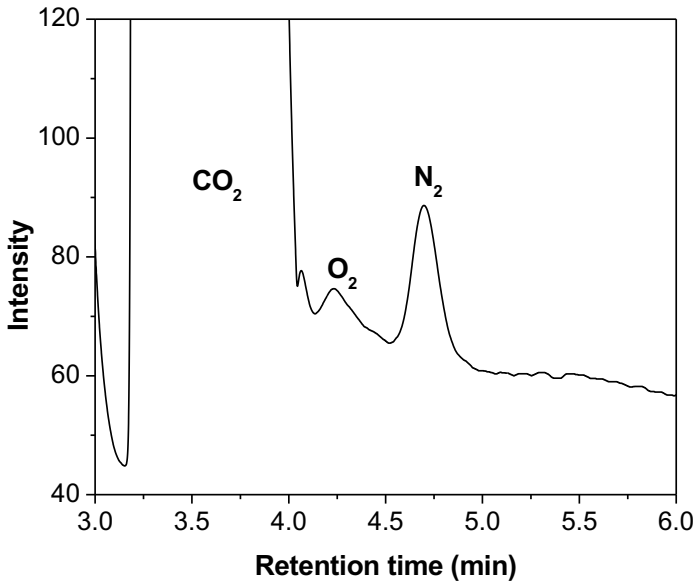

Figure S6. GC chromatogram of the O_2 peak, showing the difficulty in obtaining high precision data due to it positioning near the large CO2 peak and the N_2 peak. The N_2 is a contaminant from the CO_2 tank.

pack column with TCD detector at 200 °C. The injection port temperature was 225 °C. The column was hold at 90 °C for 25 min.

Table S3. Parametric study of SPARC reaction as a function of temperature, catalyst, pressure and ratio.

Run	Catalyst	T (°C)	P (bar)	P_{H2O}/P_{CO2}	Irrad	Products	
						gas	condensable
1	Co/TiO_2	110	1.0	1.2	+	n/a	CH_3OH
2	Co/TiO_2	130	1.0	1.2	+	n/a	CH_3OH
3	Co/TiO_2	150	1.0	1.2	+	n/a	CH_3OH
4	Co/TiO_2	180	1.0	1.2	+	n/a	CH_3OH, C_3H_7OH
5	Co/TiO_2	200	1.0	1.2	+	CH_4,C_2H_4,C_2H_6,C_3H_6, C_3H_8, C_4H_8, CO, H_2, O_2	CH_3OH, C_2H_5OH CH_3COOH,C_3H_7OH, C_3H_7OH, $C_5H_{11}OH$,
6	Co/TiO_2	220	1.0	1.2	+	n/a	CH_3OH
7	Co/TiO_2	200	1.0	1.2	-	n/a	none
8	Co/TiO_2	200	1.0	1.2 (N_2)	+	n/a	none
9	TiO_2	200	1.0	1.2	+	n/a	none
10	Co/TiO_2	200	1.0	0.6	+	CH_4,C_2H_4,C_2H_6,C_3H_6, C_3H_8, C_4H_{10}, CO, H_2, O_2	C_2H_5OH, C_3H_6O, CH_3COOH
11	Co/TiO_2	200	1.0	0.6	-	n/a	none
12	Co/TiO_2	200	2.7	0.6	+	CH_4 ,C_2H_6,C_3H_8, C_4H_{10}, CO, H_2, O_2	HCOOH,CH_3OH, C_2H_5OH, C_3H_7OH, CH_3COOH, C_3H_6O, $C_3H_6O_2$, C_3H_8O C_4H_9OH, C_5H_8O, $C_5H_{12}O$, C_6H_8O, C_7H_{12}, C_7H_8O, C_8H_{10}, C_8H_{18}, C_9H_{12}, $C_{10}H_{14}$, $C_{10}H_{12}O_2$, $C_{13}H_{10}$, $C_{13}H_{12}$
13	Co/TiO_2	200	2.7	0.6	-	n/a	none
14	Co/TiO_2	200	2.7	0.6 (D_2O)	+	n/a	deuterium incorporated into CH_3OH, C_2H_5OH, C_3H_7OH, CH_3COOH, C_3H_6O, C_4H_9OH, $C_6H_{12}O$, C_8H_{10}, C_9H_{12}, $C_{10}H_{14}$
15	Co/TiO_2	200	2.7	1.2 ($^{13}CO_2$)	+	n/a	13-carbon incorporated into CH_3OH, C_2H_5OH, C_3H_7OH, $C_8H_{18}O$,
16	Co/TiO_2	200	2.7	1.2	+	CH_4,C_2H_4,C_2H_6,C_3H_6, C_4H_8, C_4H_{10}, C_5H_{12},CO, H_2, O_2	C_3H_7OH, $C_3H_4O_2$
17	Co/TiO_2	200	6.1	0.6	+	CH_4,C_2H_6,C_3H_6,C_3H_8, C_4H_8, C_4H_{10}, C_5H_{12},CO, H_2, O_2	CH_3OH, HCOOH, C_2H_5OH, $C_2H_2O_3$,CH_3COOH, $C_2H_2O_4$,C_3H_7OH, $C_3H_6O_2$, $C_3H_4O_3$, C_4H_9OH, C_3H_7COOH, $C_4H_{10}O_2$, $C_5H_{12}O$, $C_5H_{12}O_2$, $C_6H_{10}O_4$, C_6H_5COOH $C_8H_{16}O_5$, $C_{10}H_{20}O_2$, $C_{10}H_{12}O_2$
18	Co/TiO_2	200	6.1	1.2	+	CH_4,C_2H_4,C_2H_6,C_3H_6, C_3H_8,C_4H_8,C_5H_{12},CO,H_2, O_2	HCOOH, CH_3OH, CH_3COOH, C_3H_7OH, $C_4H_{10}O$, $C_4H_{10}O_2$

Table S4. Full product list and mass productivity as a function of pressure and partial pressure ratio at 200 °C

				Productivity (μg/gh)																			
Pressure (bar)				1.0 bar						2.7 bar										6.1 bar					
$P_{H2O/CO2}$				0.6					1.2	0.6					1.2					0.6					1.2
Products				Run1	Run2	Run3	**Avg**	std	Run 1	Run 1	Run 2	Run 3	**AVG**	Std	Run1	Run 2	**AVG**	Std	Run 1	Run 2	Run 3	**AVG**	STD	Run 1
Cn	Formula	MW	# e																				
	O2	32.0	4.0	334.2	38.0	212.0	**194.7**	148.9	194.3	188.7	425.1	310.6	**308.1**	118.3	359.2	14.9	**187.1**	243.4	213.9	14.1	285.1	**171.0**	140.5	307.3
	H2	2.0	2.0	4.2	1.6	17.5	**7.8**	8.5	6.1	9.4	16.3	16.1	**13.9**	4.0	4.4	41.2	**22.8**	26.0	6.9	3.9	8.5	**6.4**	2.3	10.4
C1	CO	28.0	2.0	29.8	9.1	26.6	**21.8**	11.2	7.5	5.7	44.4	8.3	**19.5**	21.6	20.5	25.0	**22.7**	3.2	90.8	19.5	5.6	**38.6**	45.7	15.3
	CH4	16.0	8.0	0.7	0.8	1.0	**0.8**	0.1	0.8	1.2	0.9	1.3	**1.1**	0.2	2.3	4.6	**3.4**	1.6	2.2	1.0	1.1	**1.4**	0.7	0.4
	CH2O2	46.0	2.0							0.0	0.0	69.9	**23.3**	40.4					42.8	0.0	0.0	**14.3**	24.7	7.3
	CH3OH	32.0	6.0	0.6	0.2		**0.4**	0.3		0.2	0.7	0.0	**0.3**	0.4					1.4	1.3	0.1	**0.9**	0.7	4.6
C2	C2H4	28.0	12.0	0.5	0.7	0.4	**0.5**	0.1	0.1							3.0								0.5
	C2H6	30.0	14.0	12.4	3.4	2.2	**6.0**	5.6	17.6	3.4	1.7	1.5	**2.2**	1.1	12.7	25.6	**19.1**	9.1	23.5	2.4	2.1	**9.3**	12.3	2.8
	C2H6O	46.0	12.0	0.7	1.6		**1.2**	0.6	0.1	0.1	0.0	0.0	**0.0**	0.0					0.7	2.2	0.0	**1.0**	1.1	
	C2H2O3	74.0	4.0																0.0	0.0	13.7	**4.6**	7.9	
	C2H2O4	90.0	2.0																0.0	0.0	7.0	**2.3**	4.0	
	C2H4O2	60.0	8.0	20.2	8.6		**14.4**	8.2	9.1	44.4	50.0	60.0	**51.5**	7.9					13.8	74.4	62.4	**50.2**	32.1	36.6
C3	C3H6	42.0	18.0	0.3	0.5	0.4	**0.4**	0.1	0.3										2.4	0.8	0.6	**1.3**	1.0	0.1
	C3H8	44.0	20.0	1.2	1.3	0.8	**1.1**	0.2	0.9	1.0	1.5	1.5	**1.3**	0.3		3.0			1.6	1.2	1.2	**1.3**	0.3	0.8
	C3H6O	58.0	16.0							0.2	0.0	0.0	**0.1**	0.1										
	C3H6O2	74.0	14.0								14.7	0.3	**7.5**	10.2					0.0	0.7	4.1	**1.6**	2.2	
	C3H8O	60.0	18.0	2.7	0.2		**1.5**	1.8	0.1	0.7	1.3	0.6	**0.9**	0.4	1.9				0.5	1.2	0.0	**0.6**	0.6	15.8
	C3H4O2	72.0	4.0													7.2								
	C3H4O3	88.0	12.0																0.2	0.0	0.0	**0.1**	0.1	
C4	C4H8	56.0	24.0	1.2	1.1	0.9	**1.1**	0.2								0.2								0.3
	C4H10	58.0	26.0						0.1	6.9	1.1	1.2	**3.1**	3.3		2.8			8.1	2.1	4.1	**4.8**	3.1	
	C4H10O	74.0	24.0							28.5	0.0	0.0	**9.5**	16.5					1.7	0.0	0.0	**0.6**	1.0	2.1
	C4H8O2	88.0	20.0																14.0	0.0	22.2	**12.1**	11.2	
	C4H10O2	90.0	22.0																3.8	0.0	0.0	**1.3**	2.2	1.4
C5	C5H12	72.0	32.0													1.5			0.8	0.4	0.6	**0.6**	0.2	0.0
	C5H8O	84.0	26.0							0.0	0.0	1.9	**0.6**	1.1										
	C5H12O	88.0	30.0	7.4			**3.7**	5.2		0.0	3.7	1.0	**1.6**	1.9					0.0	0.9	4.1	**1.7**		
	C5H12O2	104.0	26.0																7.4	0.0	0.0	**2.5**		
C6	C6H8O	90.0	30.0							0.0	0.0	3.0	**1.0**	1.7										
	C6H10O4	146.0	26.0																0.0	2.3	26.9	**9.7**		
C7	C7H12	96.0	40.0							0.0	0.0	1.0	**0.3**	0.6										
	C7H8O	108.0	34.0							0.0	0.0	1.1	**0.4**	0.6										
	C7H6O2	122.0	30.0																4.3	0.0	0.0	**1.4**		
C8	C8H10	106.0	42.0							0.2	0.0	0.0	**0.1**	0.1										
	C8H18	114.0	50.0							0.0	1.1	0.0	**0.4**	0.6										
	C8H16O5	192.0	38.0																6.7	0.0	0.0	**2.2**		
C9	C9H12	120.0	46.0							1.9	0.0	0.0	**0.6**	1.1										
C10	C10H14	134.0	54.0							0.1	0.0	0.0	**0.0**	0.0										
	C10H20O2	140.0	60.0							0.0	1.3	0.0	**0.4**	0.8					0.0	0.0	1.6	**0.5**		
	C10H12O2	164.0	48.0																10.5	0.0	0.0	**3.5**		
C13	C13H10	166.0	62.0							0.0	1.8	0.0	**0.6**	1.0										
	C13H12	168.0	64.0							0.0	2.6	0.0	**0.9**	1.5										
	H2			**4.2**	**1.6**	**17.5**	**7.8**	**8.5**	**6.1**	**9.4**	**16.3**	**16.1**	**13.9**	**4.0**	**4.4**	**41.2**	**22.8**	**26.0**	**6.9**	**3.9**	**8.5**	**6.4**	**2.3**	**10.4**
	C1			**31.2**	**10.0**	**27.6**	**23.0**	**11.6**	**8.3**	**7.1**	**46.0**	**79.5**	**44.2**	**62.5**	**22.8**	**29.5**	**26.1**	**4.8**	**137.2**	**21.8**	**6.9**	**55.3**	**71.8**	**27.6**
	C2-4			**39.2**	**17.4**	**4.7**	**26.1**	**16.8**	**28.3**	**85.2**	**70.2**	**65.1**	**76.0**	**39.7**	**14.6**	**41.9**	**19.1**	**9.1**	**70.4**	**85.1**	**117.4**	**91.0**	**79.0**	**60.4**
	C5+			**7.4**	**0.0**	**0.0**	**0.0**	**0.0**	**0.0**	**2.2**	**10.5**	**8.0**	**6.9**	**11.1**	**0.0**	**1.5**	**0.0**	**0.0**	**29.7**	**3.6**	**33.2**	**22.1**	**0.2**	**0.0**
	Gas prod			**384.6**	**56.5**	**261.8**	**234.3**	**174.9**	**227.7**	**216.3**	**491.0**	**340.5**	**349.3**	**148.7**	**399.0**	**121.8**	**255.1**	**283.4**	**350.2**	**45.5**	**308.9**	**234.9**	**205.9**	**338.0**
	Conden. prod			**31.6**	**10.5**	**0.0**	**21.1**	**16.2**	**9.3**	**76.3**	**77.2**	**138.8**	**99.9**	**86.9**	**1.9**	**7.2**	**0.0**	**0.0**	**107.8**	**83.0**	**142.1**	**111.0**	**87.9**	**67.8**

Table S5. Full product list and molar (electrons stored) productivity as a function of pressure and partial pressure ratio at 200 C

				Productivity (μmol electrons/gh)																			
Pressure (bar)				1.0 bar						2.7 bar									6.1 bar					
$P_{H2O/CO2}$				0.6					1.2	0.6					1.2				0.6					1.2
Products				Run1	Run2	Run3	**Avg**	std	Run 1	Run1	Run 2	Run 3	**AVG**	Std	Run1	Run 2	**AVG**	Std	Run 1	Run 2	Run 3	**AVG**	STD	Run 1
Cn	Formula	MW	# e																				
	O2	32.0	4.0	41.8	4.8	26.5	**24.3**	18.6	24.3	23.6	53.1	38.8	**38.5**	14.8	44.9	1.9	**23.4**	30.4	26.7	1.8	35.6	**21.4**	17.6	38.4
	H2	2.0	2.0	4.2	1.6	17.5	**7.8**	8.5	6.1	9.4	16.3	16.1	**13.9**	4.0	4.4	41.2	**22.8**	26.0	6.9	3.9	8.5	**6.4**	2.3	10.4
C1	CO	28.0	2.0	2.1	0.6	1.9	**1.6**	0.8	0.5	0.4	3.2	0.6	**1.4**	1.5	1.5	1.8	**1.6**	0.2	6.5	1.4	0.4	**2.8**	3.3	1.1
	CH4	16.0	8.0	0.4	0.4	0.5	**0.4**	0.1	0.4	0.6	0.5	0.6	**0.6**	0.1	1.2	2.3	**1.7**	0.8	1.1	0.5	0.6	**0.7**	0.3	0.2
	CH2O2	46.0	2.0								0.0	3.0	**1.5**	2.1					1.9	0.0	0.0	**0.6**	1.1	0.3
	CH3OH	32.0	6.0	0.1	0.0		**0.1**	0.1		0.0	0.1	0.0	**0.1**	0.1					0.3	0.2	0.0	**0.2**	0.1	0.9
C2	C2H4	28.0	12.0	0.2	0.3	0.2	**0.2**	0.1	0.0							1.3	**1.3**							0.2
	C2H6	30.0	14.0	5.8	1.6	1.0	**2.8**	2.6	8.2	1.6	0.8	0.7	**1.0**	0.5	5.9	11.9	**8.9**	4.3	11.0	1.1	1.0	**4.4**	5.7	1.3
	C2H6O	46.0	12.0	0.2	0.4		**0.3**	0.2	0.0	0.0	0.0	0.0	**0.0**	0.0					0.2	0.6	0.0	**0.3**	0.3	
	C2H2O3	74.0	4.0																0.0	0.0	0.7	**0.2**	0.4	
	C2H2O4	90.0	2.0																0.0	0.0	0.2	**0.1**	0.1	
	C2H4O2	60.0	8.0	2.7	1.1		**1.9**	1.1	1.2	5.9	6.7	8.0	**6.9**	1.1					1.8	9.9	8.3	**6.7**	4.3	4.9
C3	C3H6	42.0	18.0	0.1	0.2	0.2	**0.2**	0.0	0.1										1.0	0.4	0.3	**0.6**	0.4	0.1
	C3H8	44.0	20.0	0.5	0.6	0.4	**0.5**	0.1	0.4	0.4	0.7	0.7	**0.6**	0.1		1.4	**1.4**		0.7	0.5	0.6	**0.6**	0.1	0.4
	C3H6O	58.0	16.0							0.1	0.0	0.0	**0.0**	0.0										
	C3H6O2	74.0	14.0								2.8	0.1	**1.4**	1.9					0.0	0.1	0.8	**0.3**	0.4	
	C3H8O	60.0	18.0	0.8	0.1		**0.4**	0.5	0.0	0.2	0.4	0.2	**0.3**	0.1	0.6		**0.6**		0.2	0.4	0.0	**0.2**	0.2	4.7
	C3H4O2	72.0	4.0													0.4	**0.4**							
	C3H4O3	88.0	12.0																0.0	0.0	0.0	**0.0**	0.0	
C4	C4H8	56.0	24.0	0.5	0.5	0.4	**0.5**	0.1								0.1	**0.1**							0.1
	C4H10	58.0	26.0						0.0	3.1	0.5	0.5	**1.4**	1.5		1.3	**1.3**		3.6	0.9	1.8	**2.1**	1.4	
	C4H10O	74.0	24.0							9.2	0.0	0.0	**3.1**	5.3					0.6	0.0	0.0	**0.2**	0.3	0.7
	C4H8O2	88.0	20.0																3.2	0.0	5.0	**2.7**	2.6	
	C4H10O2	90.0	22.0																0.9	0.0	0.0	**0.3**	0.5	0.3
C5	C5H12	72.0	32.0													0.6	**0.6**		0.3	0.2	0.3	**0.3**	0.1	0.0
	C5H8O	84.0	26.0								0.0	0.6	**0.3**	0.4										
	C5H12O	88.0	30.0	2.5			**1.3**	1.8			1.3	0.3	**0.8**	0.7					0.0	0.3	1.4	**0.6**	0.7	
	C5H12O2	104.0	26.0																1.9	0.0	0.0	**0.6**	1.1	
C6	C6H8O	90.0	30.0								0.0	1.0	**0.5**	0.7										
	C6H10O4	146.0	26.0																0.0	0.4	4.8	**1.7**	2.7	
C7	C7H12	96.0	40.0								0.0	0.4	**0.2**	0.3										
	C7H8O	108.0	34.0																					
	C7H6O2	122.0	30.0																1.1	0.0	0.0	**0.4**	0.6	
C8	C8H10	106.0	42.0							0.1	0.0		**0.0**	0.1										
	C8H18	114.0	50.0							0.0	0.5		**0.2**	0.3										
	C8H16O5	192.0	38.0																1.3	0.0	0.0	**0.4**	0.8	
C9	C9H12	120.0	46.0							0.7	0.0		**0.4**	0.5										
C10	C10H14	134.0	54.0							0.0	0.0		**0.0**	0.0										
	C10H20O2	140.0	60.0							0.0	0.6		**0.3**	0.4					0.0	0.0	0.7	**0.2**	0.4	
	C10H12O2	164.0	48.0																3.1	0.0	0.0	**1.0**	1.8	
C13	C13H10	166.0	62.0							0.0	0.7		**0.3**	0.5										
	C13H12	168.0	64.0							0.0	1.0		**0.5**	0.7										
	H2			**4.2**	**1.6**	**17.5**	**7.8**	**8.5**	**6.1**	**9.4**	**16.3**	**16.1**	**13.9**	**4.0**	**4.4**	**41.2**	**22.8**	**26.0**	**6.9**	**3.9**	**8.5**	**6.4**	**2.3**	**10.4**
	C1			**2.6**	**1.1**	**2.4**	**2.0**	**0.9**	**0.9**	**1.0**	**3.8**	**4.3**	**3.5**	**3.9**	**2.6**	**4.1**	**3.3**	**1.0**	**9.7**	**2.1**	**1.0**	**4.3**	**4.8**	**2.5**
	C2-4			**10.9**	**4.8**	**2.1**	**6.8**	**4.7**	**10.1**	**20.6**	**11.8**	**10.2**	**14.7**	**10.6**	**6.5**	**16.4**	**13.9**	**4.3**	**23.2**	**14.0**	**18.7**	**18.6**	**16.7**	**12.7**
	C5+			**0.0**	**0.0**	**0.0**	**0.0**	**0.0**	**0.0**	**0.8**	**4.0**	**2.3**	**3.6**	**4.6**	**0.0**	**0.6**	**0.6**	**0.0**	**7.6**	**0.9**	**7.1**	**5.2**	**8.1**	**0.0**
	Gas prod			**55.7**	**10.6**	**48.5**	**38.3**	**30.9**	**40.2**	**39.1**	**75.0**	**58.1**	**57.4**	**22.5**	**57.8**	**63.8**	**63.1**	**61.7**	**57.9**	**10.7**	**49.0**	**39.2**	**31.2**	**52.2**
	Conden. prod			**6.3**	**1.7**	**0.0**	**2.7**	**1.8**	**1.3**	**16.3**	**13.9**	**13.6**	**16.8**	**15.3**	**0.6**	**0.4**	**1.0**	**0.0**	**16.3**	**11.9**	**21.9**	**16.7**	**18.3**	**11.8**

IV. Isotopic labeling experiments using $^{13}CO_2$ and D_2O

In order to confirm the products are derived from CO_2 and H_2O, isotopically enriched $^{13}CO_2$ (30% $^{13}CO_2$ purchased from Aldrich) or D_2O (99% D_2O from Aldrich) were used as a feedstock. Products were analyzed using a Shimadzu GC-MS-2010SE chromatograph with a MS QP2010 detector and an AOC-4 20S auto sampler. The mass spectrometer was operated in electroionization mode (EI) at 250 °C with the filament operating at 70 eV in SCAN and SIM mode. After identification of the unlabeled sample by analysis of the entire MS spectrometric pattern, the MS of a representative fragment was scanned in detail to obtain a good signal to noise for the labeled and unlabeled product and the spectrometric patterns compared.

Supplementary figures 7-8 show the results for the $^{13}CO_2$ labeling experiment conducted at 200 °C, 2.7 bar, P_{H2O}/P_{CO2} = 1.2 for isopropanol and 2-ethyl-hexanol, respectively. The ^{13}C appeared in the mass spectroscopy as well as the compared isotopic ratios values for the ^{13}C incorporation into the product, given the original 30% isotopic labeling. The deuterium labeling experiment was conducted with 99% D_2O (Supplementary figures 9-13) at 200 °C, 2.7 bar, P_{H2O}/P_{CO2} = 0.6. The mass spectroscopies of the unlabeled and labeled products are shown below for methanol, ethanol, propanol and a C_9 and C_{10} product. In this case, the labeling was a little less than expected from the 99% D_2O which we attribute to adventitious unlabeled water being in the reactor.

a

Event	Time (min)	Event time(s)	Acq. mode	m/z		
				Start	End	Ch1
1	1 to 3	0.2	SCAN	25	150	
2	1 to 3	0.1	SIM			45
3	1 to 3	0.1	SCAN	45.5	48.5	

b

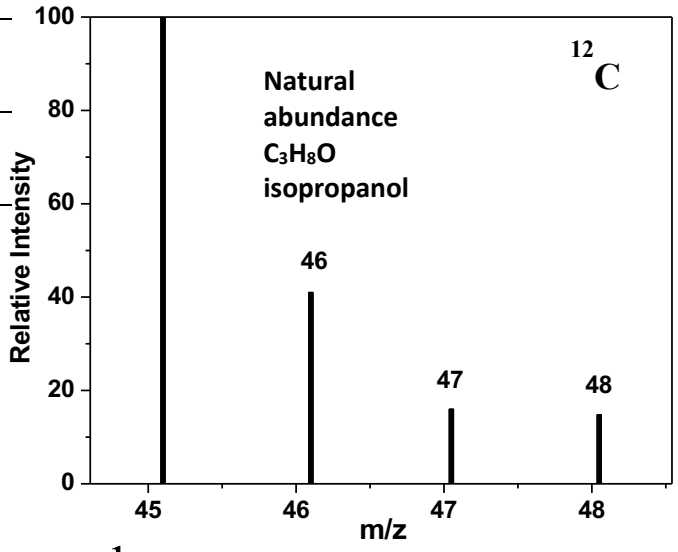

c

m/z	^{12}C	^{13}C
46.1	2.05%	2.90%
47.1	19.02%	10.73%
48.1	10.25%	35.49%
49.1	3.25%	36.36%

d

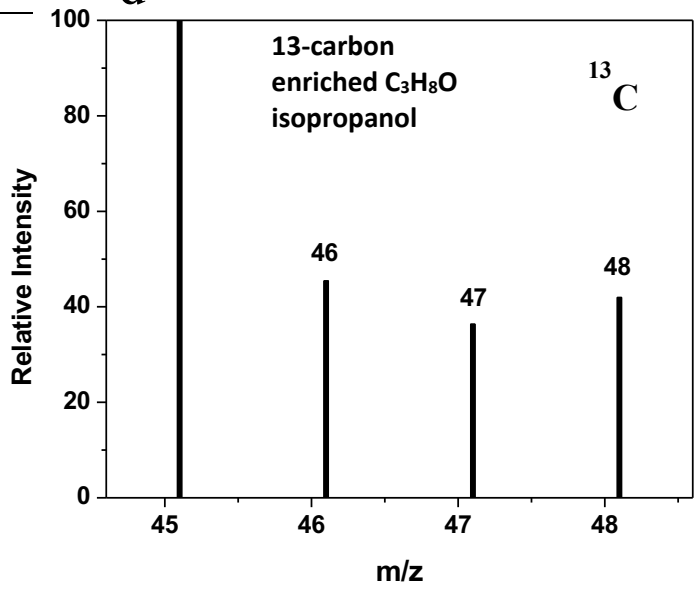

Figure S7. Gas Chromatography/Mass spectroscopy of isopropanol product from experiment was conducted with ^{13}C labeling and H_2O at 200 °C, 2.7 bar, P_{H2O}/P_{CO2} = 1.2. (a) The mass spectrometer operating set up, (b) $^{12}CO_2$ sample, (d) $^{13}CO_2$ sample and (c) compared isotopic ratios.

a

Event	Time (min)	Event time(s)	Acq. mode	^{12}C m/z		
				Start	End	Ch1
1	10 to13	0.2	SCAN	25	150	
2	10 to13	0.1	SIM			112
3	10to 13	0.1	SCAN	110.5	125.5	

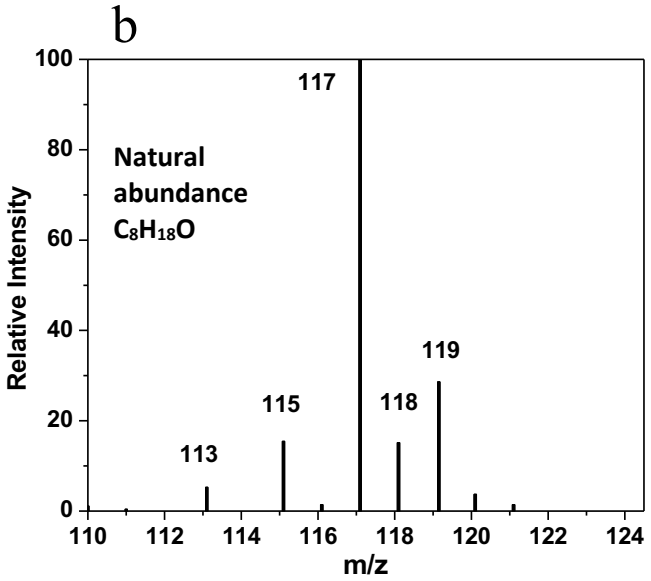

c

m/z	^{12}C	^{13}C
111.1	37.72 %	58.41 %
116.1	9.26 %	15.61 %
118.1	15.16 %	55.20 %
120.1	13.00 %	18.31 %
121.1	38.44 %	27.66 %
123.1	0 %	50.00 %

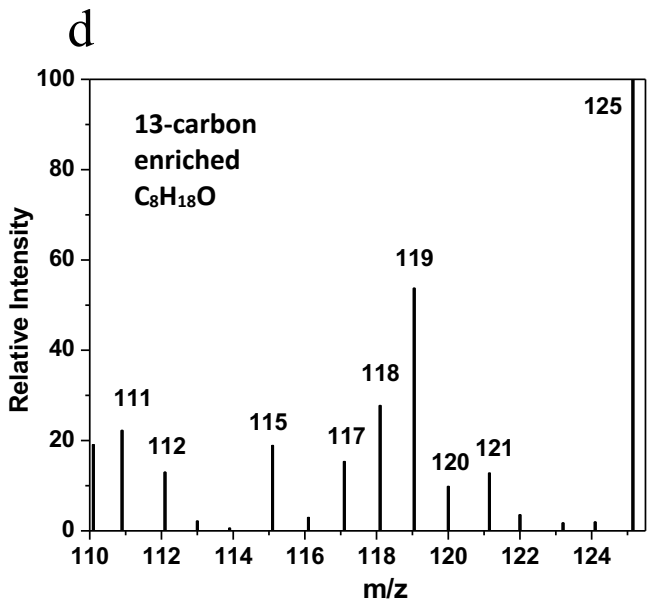

Figure S8. Gas Chromatography/Mass spectroscopy of 2-ethyl-1-hexanol ($C_8H_{18}O$) product from experiment was conducted with ^{13}C labeling and H_2O at 200 °C, 2.7 bar, P_{H2O}/P_{CO2} = 1.2. (a) The mass spectrometer operating set up, (b) $^{12}CO_2$ sample, (d) $^{13}CO_2$ sample and (c) compared isotopic ratios.

a

Event	Time (min)	Event time(s)	Acq. mode	m/z			
				Start	End	Ch1	Ch2
1	1 to 3	0.2	SCAN	25	150		
2	1 to 3	0.1	SIM			31	32
3	1 to 3	0.1	SCAN	27	38		

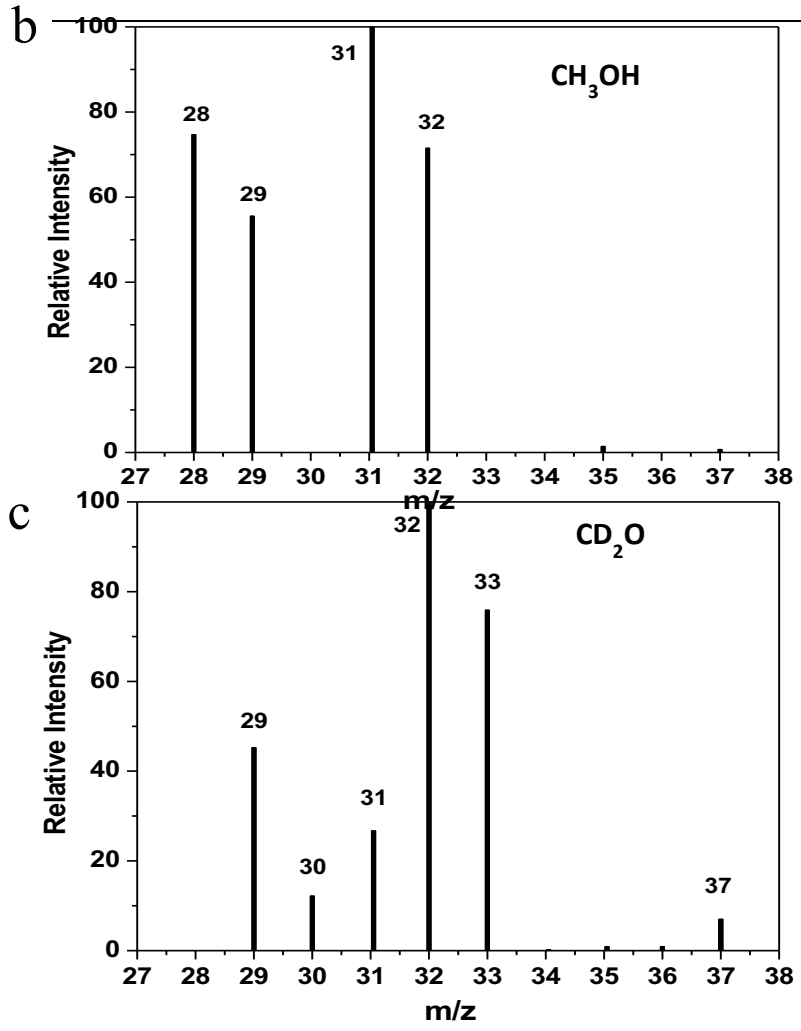

Figure S9. Gas Chromatography/Mass spectroscopy of methanol product from experiment was conducted with D_2O and $^{12}CO_2$ at 200 °C, 2.7 bar, P_{D2O}/P_{CO2} = 0.6. (a) The mass spectrometer operating set up, (b) H_2O sample, (c) D_2O sample.

a

Event	Time (min)	Event time(s)	Acq. mode	m/z			
				Start	End	Ch1	Ch2
1	1 to 3	0.2	SCAN	25	150		
2	1 to 3	0.1	SIM			31	45
3	1 to 3	0.1	SCAN	25	70		

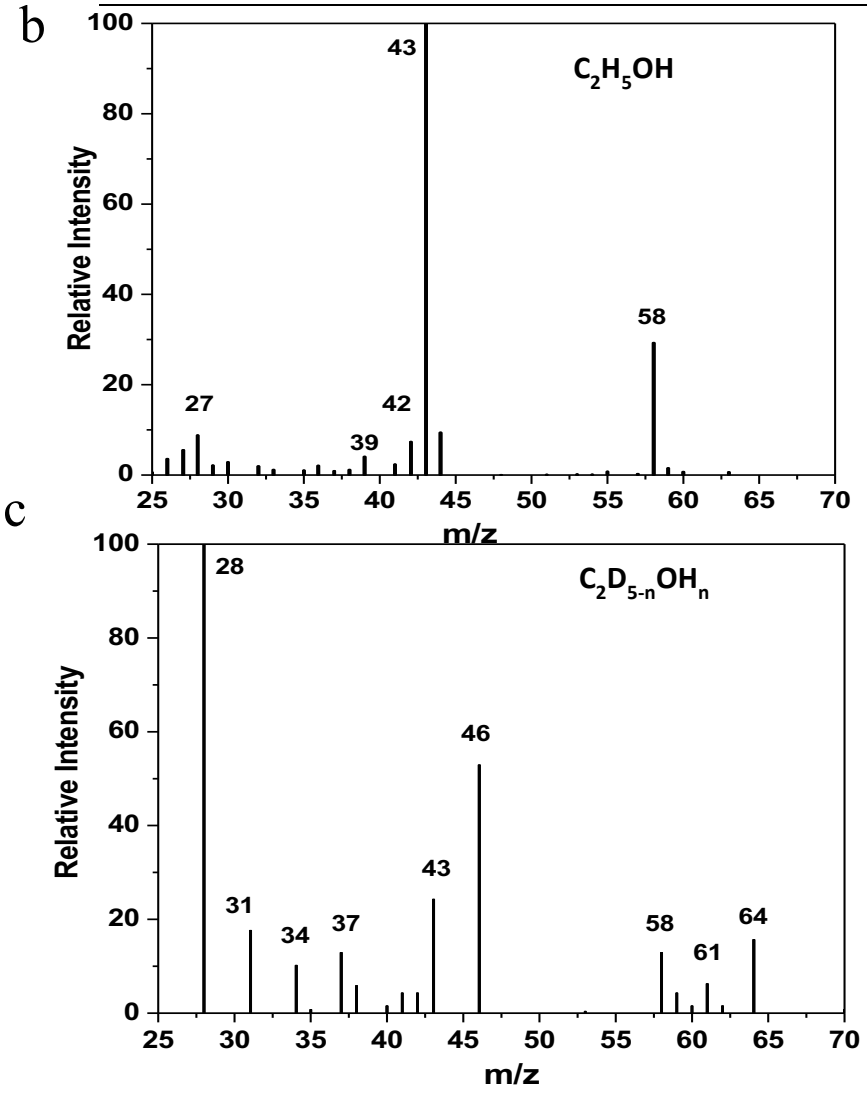

Figure S10. Gas Chromatography/Mass spectroscopy of ethanol (C_2H_5OH) product from experiment was conducted with D_2O and $^{12}CO_2$ at 200 °C, 2.7 bar, P_{D2O}/P_{CO2} = 0.6. (a) The mass spectrometer operating set up, (b) H_2O sample, (c) D_2O sample.

a

Event	Time (min)	Event time(s)	Acq. mode	m/z			
				Start	End	Ch1	Ch2
1	1 to 3	0.2	SCAN	25	150		
2	1 to 3	0.1	SIM			45	59
3	1 to 3	0.1	SCAN	25	65		

b

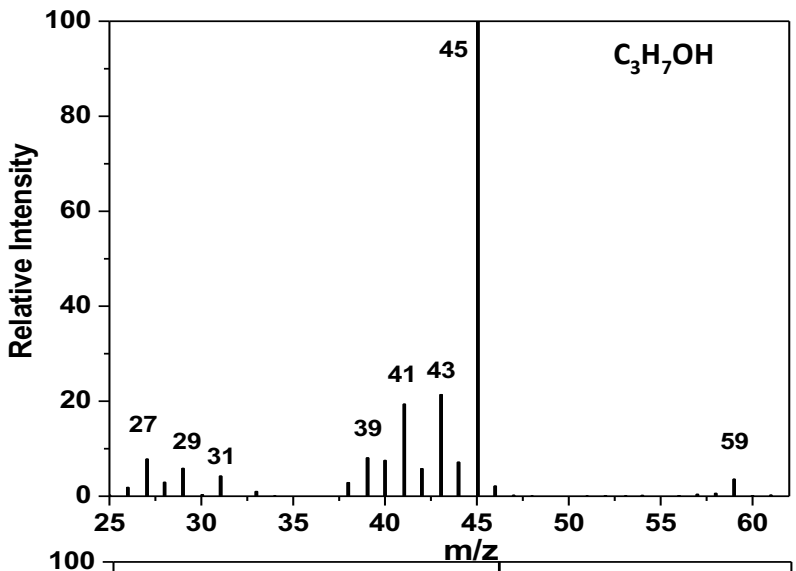

c

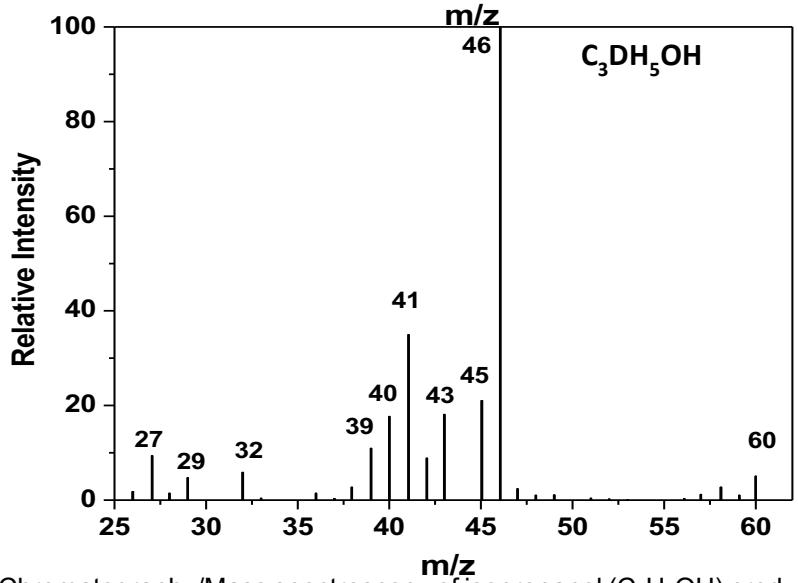

Figure S11. Gas Chromatography/Mass spectroscopy of isopropanol (C_3H_7OH) product from experiment was conducted with D_2O and $^{12}CO_2$ at 200 °C, 2.7 bar, P_{D2O}/P_{CO2} = 0.6. (a) The mass spectrometer operating set up, (b) H_2O sample, (c) D_2O sample.

a

Event	Time (min)	Event time(s)	Acq. mode	m/z			
				Start	End	Ch1	Ch2
1	110 to 13	0.2	SCAN	25	150		
2	110 to 13	0.1	SIM			105	120
3	110 to 13	0.1	SCAN	25	135		

b

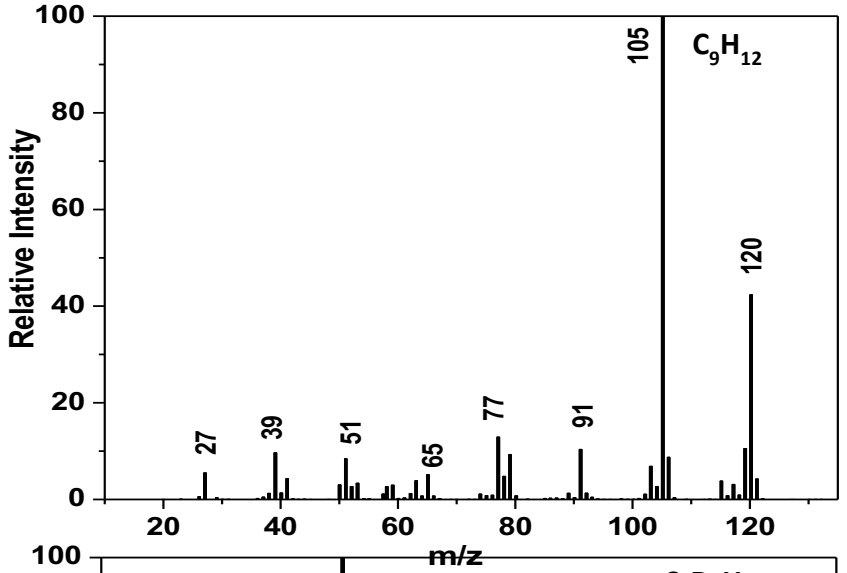

c

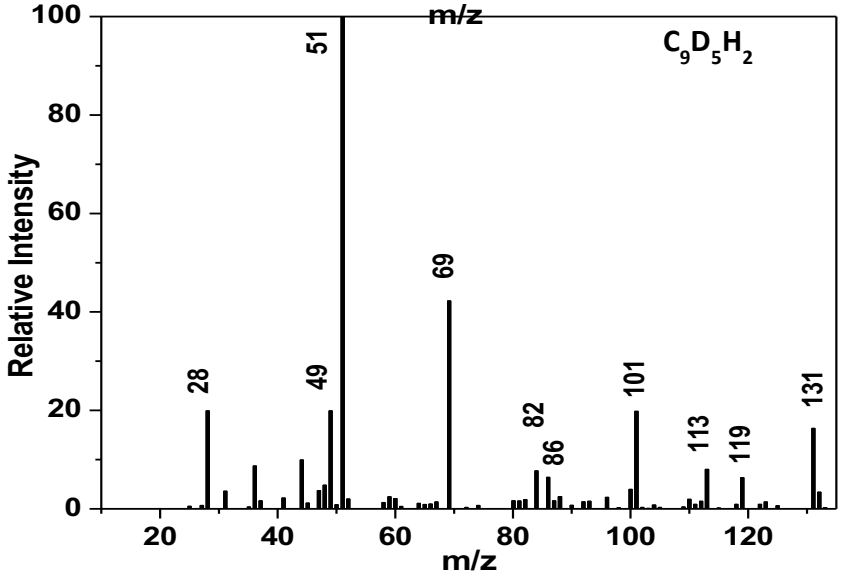

Figure S12. Gas Chromatography/Mass spectroscopy of a derivative of benzene (C_9H_{12}) product from experiment was conducted with D_2O and $^{12}CO_2$ at 200 °C, 2.7 bar, P_{D2O}/P_{CO2} = 0.6. (a) The mass spectrometer operating set up, (b) H_2O sample, (c) D_2O sample.

a

Event	Time (min)	Event time(s)	Acq. mode	m/z			
				Start	End	Ch1	Ch2
1	10 to 13	0.2	SCAN	25	150		
2	10 to 13	0.1	SIM			105	134
3	10 to 13	0.1	SCAN	25	150		

b

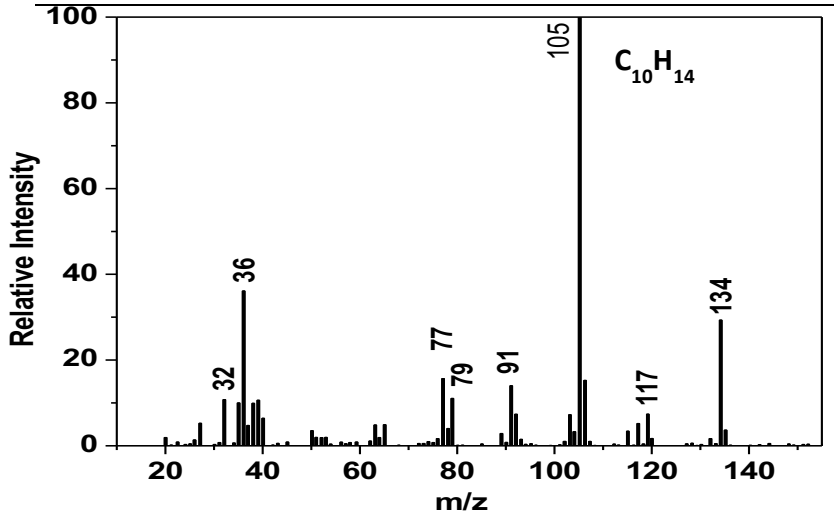

c

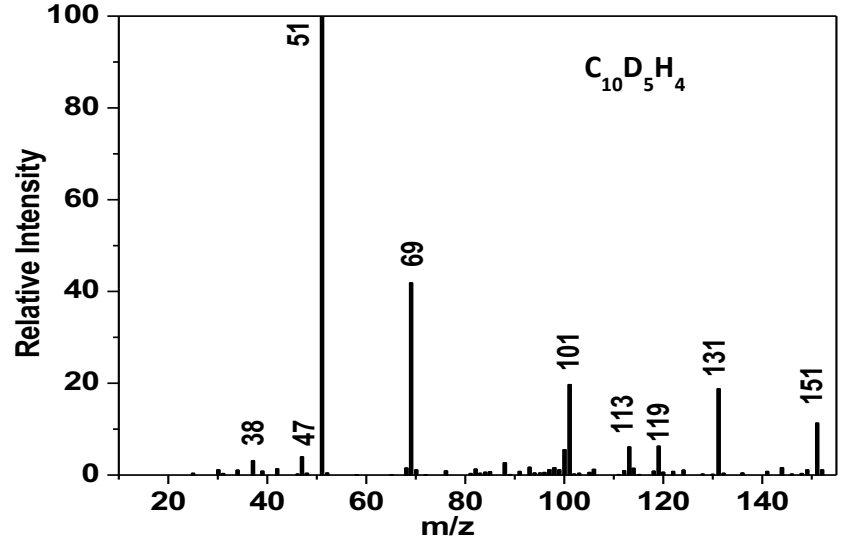

Figure S13. Gas Chromatography/Mass spectroscopy of a derivative of benzene ($C_{10}H_{14}$) product from experiment was conducted with D_2O and $^{12}CO_2$ at 200 °C, 2.7 bar, P_{D2O}/P_{CO2} = 0.6. (a) The mass spectrometer operating set up, (b) H_2O sample, (c) D_2O sample.

References:

S1. Cho-Ching L, Chung-Hsuang H, Chung-Shin Y & Jen-Fong W (2007) Photoreduction of carbon dioxide with H2 and H_2O over TiO_2 and ZrO_2 in a circulated photocatalytic reator. Solar Energy Materials &Solar Cells 91 : 1765-1774.

S2. Cullity B.D. & Stock S.R., *Elements of X-Ray Diffraction*, 3rd Ed., Prentice-Hall Inc., 2001, p 167-171, ISBN 0-201-61091-4.

S3. Gribb, A. A.; Banfield, J. F(1997) Particle size effects on transformation kinetics and phase stability in nanocrystalline TiO_2. *Am. Mineral*. 82, 717.

S4. Lowell S, Shields JE, Thomas, MA & Thommes M.(2004) Characterization of porous solids and powders : surface area, pore size and Density. Volume 16 of the series *Particle Technology Series* p 58-81

S5. Narendra Pai K. R., Anjusree G. S., Deepak T. G., Subash D., Shantikumar V. Nair & Sreekumaran Nair A.(2014) High surface area TiO_2 nanoparticles by a freezedrying approach for dye-sensitized solar cells. *RSC Adv.* 4, 36821–36827

Retraction for Chanmanee et Al., Solar Photothermochemical Alkane Reverse Combustion. *Proc. Natl. Acad. Sci.* **2018**, *115* (3), E557–E557.

Retraction Letter

We wish to retract this article as it is now apparent that our results are largely due to artifacts and that the underlying thesis of this work has not been demonstrated. In this paper, we reported that CO_2 and steam, passed over a cobalt on P25 TiO_2 catalyst at 200 C and 1-6 atm total pressure, was forming higher carbon number hydrocarbons (up to C_{13}), when irradiated with UV light. We postulated that CO_2 was reduced to CO and water oxidized to give H_2 or cobalt surface-bound hydrides via TiO_2 mediated photochemical reactions and then these intermediates were consumed in thermally-driven Fischer Tropsch-like processes to yield higher carbon number hydrocarbons.

It is now apparent that the majority of the carbon in the products is from carbon impurities, presumably graphite, present in the TiO_2. In order to verify that the CO_2 was the carbon source, we conducted a labelling experiment using 30% isotopically enriched $^{13}CO_2$ and saw a shift in that parent ion peak distribution shift to higher m/z (see Figures S7 and S8), however following publication, Professor Geoffrey Ozin of the University of Toronto, communicated to us the need to verify such results using 100% isotopically enriched $^{13}CO_2$. While initially skeptical, when we performed an experiment (200 °C, 2.1 atm, 99% enriched $^{13}CO_2$) the GC-MS data of the liquid products showed very little incorporation of the label (less than 5%) into the products. Subsequent runs in which the CO_2 feedstock was replaced with helium gas (200 °C, 2.1 atm, water present) also

showed the presence of similar amounts of higher hydrocarbon products in the liquid phase, although the product distribution and isomers were different.

Our work in the paper was done using Degussa (Frankfurt, Germany) P25 titanium dioxide (Control number 2047) which is now manufactured and marketed by Evonik Industries (Parsippany, NJ). Having run out of the Degussa P25 before discovering our error, all our subsequent data has been obtained on the Evonik Aeroxide^{R} TiO_2 P25. Carbon elemental analysis reveals 0.012% carbon (Galbraith Labs, Knoxville, TN) while calcination in air at 400 °C for 6 h does nothing to improve this as the carbon content in this sample was 0.015% (small increase due to lost moisture/adsorbates) and we start to see conversion of the anatase phase into rutile, so further heating was not done. As our productivities were in the 61 to 175 μg product per g TiO_2 per hour, mass balance is possible due to adventitious carbon (however our Degussa P25 must have had a greater carbon content that our Evonik P25).

We were aware of previous reports that TiO_2 having trace absorbed acetic acid impurities or graphitic carbon impurities (especially for homemade TiO_2 prepared via sol-gel methods).[REF] UV irradiation in the presence of moisture could mobilize these materials to form hydrocarbons such as methane, methanol, and acetic acid, however no reports of higher hydrocarbons being formed/released were known to us. Clearly, the addition of heat to the irradiated TiO_2 mobilizes bigger fragments of the carbon and is responsible for our observations of higher hydrocarbons. For the record, we considered that the carbon impurities may be in the form of carbonates, and investigated the reaction (200 °C, 2.1 atm, CO_2 and H_2O) in which the TiO_2 was impregnated with sodium carbonate (1

mass% of the cobalt-TiO_2 catalyst) but the results were no different than that without the added carbonate.

Biographical Information

Mohammad Fakrul Islam obtained his Bachelor of Science degree in chemistry from the University of Dhaka, Bangladesh in 2010 and Master of Science from Analytical and Inorganic Chemistry from the same institute in 2012. He started his doctoral studies under the supervision of Dr. Frederick MacDonnell at the university of Texas at Arlington in August 2013. His research focused on the synthesis and analysis of aluminum chlorohydrate using Liquid Chromatography-Mass Spectrometry.